12-15-2014

Influence of Defects in Epitaxial Graphene Towards Material Growth and Device Performances

Shamaita Shithi Shetu
University of South Carolina - Columbia

INFLUENCE OF DEFECTS IN EPITAXIAL GRAPHENE TOWARDS MATERIAL GROWTH AND DEVICE PERFORMANCES

by

Shamaita Shithi Shetu

Bachelor of Science
Bangladesh University of Engg & Technology, 2008

Master of Engineering
University of South Carolina, 2012

Submitted in Partial Fulfillment of the Requirements

for the Degree of Doctor of Philosophy in

Electrical Engineering

College of Engineering and Computing

University of South Carolina

2014

Accepted by:

MVS Chandrashekhar, Major Professor

Tangali S. Sudarshan, Committee Member

Goutam Koley, Committee Member

John W. Weidner, Committee Member

Lacy Ford, Vice Provost and Dean of Graduate Studies

DEDICATION

To my parents Md. Shahid Ullah Bhuiyan and Nurjahan Begum, my husband B M Farid Rahman, my son Shadhin Rahman and my beloved motherland The People's Republic of Bangladesh.

ACKNOWLEDGEMENTS

I'd like to express my deep appreciation to many people without whom I couldn't reach to this point of my life. First of all, I'd like to thank my advisor, Dr. MVS Chandrashekhar for believing in me for the experimental works related with furnace and guiding me throughout my PhD years. He is very knowledgeable and insightful, and has pointed me to the right direction many times; he has also been very supportive of my research and encouraged me even when I feel frustrated though the course of my graduate study ; in addition to guiding me through my projects, he also coached me on paper writing and presentations skills, which could be as important as doing good research; last but not least, he cared about my personal well-being as well as that of my family's, which is a noble quality and it helped me not only to be perform well in research but also being a better human being.

I would also like to thank Professor Tangali S Sudarshan, for his valuable advice and encouragement throughout my work as well as guiding me though my writing and presentation skills. His open-ended policy to exploit the lab equipment enhanced my hands on experience which helped me to land on a well-deserved job. I am also very thankful to Dr Goutam Koley, his enthusiasm for research and ideas to implement experiments was invaluable through the projects we work together. I would also like to thank Dr. John W. Weidner for being a part of my committee, to provide valuable feedback throughout my study and ensuring the quality of this work. I also thank Dr.

Chris Williams for the use of his Raman system which is an important part of my work. I also gratefully acknowledge my lab mates in Clean Energy Lab ,SiC Lab and NESL, throughout the last five years for their enormous support and discussions which made my graduate life more rewarding. As I walk through my memory lane, they will always be one of the most memorable ones for not only being a part of my graduate study but also for being there for me in my pregnancy period and the times of hardship while taking care of a baby as a graduate student.

Lastly, I would like to thank my family for their endless emotional and spiritual support. My father (Md Shadhid Ullah Bhuiyan) and mother (Nurjahan begum) for their constant support and the sacrifices they have made throughout my life to give me this opportunity; My sister (Paromita Shithi Nitu) and brother (Ahmed Sumit Noor) for their silly talks to deal with the stress; My mother-in-law (Shamsunnahar) and father in-law (Md. Atiar Rahman) for their encouragement to achieve this goal. Most importantly, I deeply appreciate my wonderful husband B M Farid Rahman to be there for me and supporting me throughout my studies. He had been my inspiration, my guide, my mentor and I really thank almighty to be blessed as his wife. His continuous encouragement and sacrifices during my pregnancy and motherhood landed me to the fulfillment of the biggest achievement of my life, my PhD degree. Finally, I want to share all my achievements with my son Shadhin Rahman for his enormous sacrifices and hardships in infancy and toddler years to keep me stay focused on my research and fulfill my dream of being a doctorate.

Shamaita S Shetu

August 2014, Columbia, SC USA

ABSTRACT

Since its invention in 2004, Graphene, a two dimensional array of SP^2 bonded carbon atoms has received significant interest by the scientific community due to its unique electrical, optical and mechanical properties. A promising route to the synthesis of large-area graphene, is epitaxial graphene formed by sublimation of silicon atoms from Silicon carbide at elevated temperatures (>1200^{o}C). Although the electronic and mechanical properties of graphene with perfect atomic lattice are outstanding, the structural defects, which may appear during graphene growth, can influence the growth mechanism and material properties. However, deviations from perfection, i.e. introducing dopants in semiconductors often considered as engineered defects, can be very useful in some applications, as they make it possible to achieve new functionalities.

In this thesis, a quantitative study is presented to investigate the role of structural defects on the growth of multilayer epitaxial graphene on polar(c plane Si and C face) and non-polar (a and m plane) 6H-SiC faces, with distinctly different defect profile and provide an insight for optimizing the EG growth. For Si-face with point defects, multilayer EG growth is influenced by diffusion of Si atoms to these defects as well as desorption through these defects. However, the growth on C-face and non-polar (a and m plane) faces, the growth is limited by the lateral diffusion of the Si atoms to the line defects/grain boundaries.

Graphene is the ideal active material for gas detection owing to its physically stable surface, practically achievable thin form, and potentially fast response time. The structural defects inherent in EG grown on C-face allows diffusion and adsorption of gas molecules extending the remarkable surface sensitivity of EG to bulk multilayer films. The carrier transport phenomenon for three different gases (N_2, NH_3 and NO_2) in EG on C-face is investigated by Fourier Transform Infrared (FTIR) reflection spectroscopy and the 3 gases were clearly distinguished, enabling a new paradigm for multi-modal gas sensing using optical interrogation of EG surfaces towards EG electronic or optical noses.

Lastly, a novel technique is established to grow defect engineered thick multilayer (> 200 MLs) graphene on Si face 4H SiC substrates (0, 4 and 8 deg off cuts) than possible with solid-state decomposition at atmospheric pressure in Argon alone (~2ML). This method exploits the thermodynamic advantages of SiF_4 to increase the Si-removal from the SiC surface, thereby increasing the graphene growth rate. The defect density for these EG layers varies from ~1 at 1400°C to <0.2 at 1600°C, enabling temperature controlled engineering of the defect profile of the material. A novel approach is also presented to estimate large number of graphene layers based on Raman and Infrared spectroscopy. This is critical for enabling defect-controlled applications in electrochemistry such as batteries and biosensors that require thick layers of activated graphitic carbon.

TABLE OF CONTENTS

LIST OF TABLES

LIST OF FIGURES

LIST OF SYMBOLS

e	Electron charge (1.6×10^{-19} C)
v_F	Fermi velocity
λ	Wave-length
c	velocity of light (3×10^8 m/s)
τ	scattering time
ħ	Normalized Planck's constant (1.054×10^{-34} Js)
n	Refractive index
ML	Monolayers
E_F	Fermi energy
μ	Mobility (cm^2/Vs)
f	Frequency
t	Time
k	Wave vector
K	Boltzmann Constant
L_G	Crystal Coherence Length/ grain Size
n_D	Defect density
n_i	Impurity concentration
R	Reflection
σ_{inter}	Interband conductivity
σ_{intra}	Intraband conductivity

LIST OF ABBREVIATIONS

AFM..... .... Atomic Force Microscopy

BCF .....Burton, Canberra and Frank

CMP..... Chemical Mechanical Polish

CVD..... Chemical Vapor Deposition

DI..... De-ionized

E-beam ..... Electron Beam

E-k.....Energy-momentum

EG..... Epitaxial Graphene

FTIR.....Fourier Transform Infrared Spectroscopy

FWHM ..... Full Width Half Maximum

HF ..... Hydrofluoric Acid

IR ..... Infrared

ML .....Monolayer

RF .....Radio Frequency

SiC ..... Silicon Carbide

TE ..... Transverse Electric

TM .....Transverse Magnetic

TCE ..... Trichloroethylene

UHV..... Ultra High Vacuum

XPS ..... X-ray Photoelectron Spectroscopy

CHAPTER 1

INTRODUCTION

In this chapter, the motivations, background and objectives of this research, titled, "***Influence of Defects in Epitaxial Graphene towards Material Growth and Device Performances***" are presented. In general, defects are considered as imperfections in materials that could significantly degrade their quality and performance. However, on some occasions, defects could be extremely useful as they could be exploited to generate novel, innovative and useful materials and functional devices. Graphene, a 2D material with honeycomb lattice structure has attracted huge interest among researchers, due to its distinctive mechanical, thermal, and electrical properties. This thesis focuses on the role of defects present in epitaxial graphene layers towards material growth and also the influence of the defects in case of epitaxial graphene based devices. Presented in this chapter are major contributions of this work, the organization of this thesis and presentations and publications by the author.

1.1.BACKGROUND

Graphene, whose discovery won the 2010 Nobel Prize in physics, has captured immense scientific and technological interest in recent years [c1:1–6]. Owing to its unique physicochemical properties: high surface area (theoretically 2630 m^2/g for single-layer graphene) [c1:1,5], excellent thermal conductivity [c1:7], electric

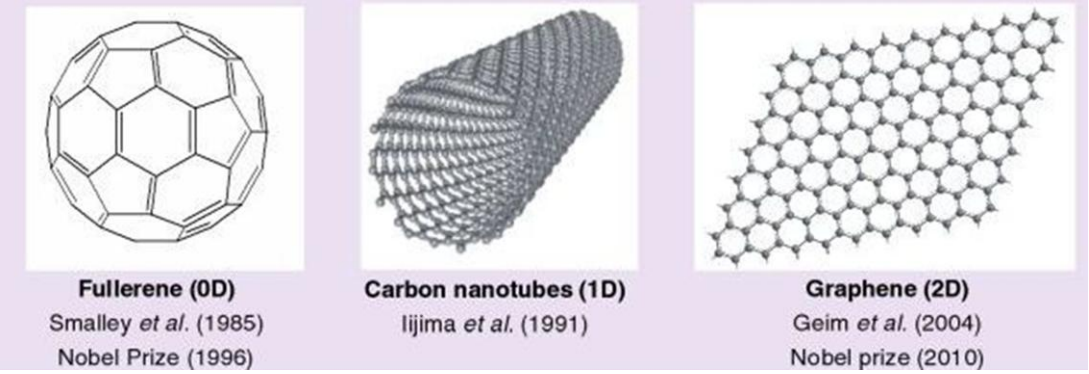

Figure 1.1: The sp^2 bonded nanomaterial -zero-dimensional (0D) fullerene and 1D carbon nanotubes and 2D Graphene.

conductivity [c1: 1, 8], and strong mechanical strength [c1: 9], graphene has found potential applications in a wide range of areas, such as electronics [c1: 10], plasmonics [c1: 11], gas filters/sensors [c1: 12,13], energy storage and applications (supercapacitors [c1: 14], batteries [c1: 15,16], fuel-cells [c1: 17-21] ,solar cells [c1: 22,23]) , biosensing applications [c1: 24-29] etc. It is a two-dimensional (2D) form of carbon atoms arranged in a honeycomb crystal structure; each carbon atom is connected to three other carbon atoms via covalent bonds with lengths of 1.42 Å and with 120◦ angles between each bonded pairs [c1: 30]; serves as the basic building block of other sp^2 carbon nanomaterial such as zero-dimensional (0D) fullerene and 1D carbon nanotubes (Figure 1.1).

Among many of the unique properties of graphene, the most unusual is that the quasiparticles (electrons and holes) in this material obey a linear dispersion relation. A linear dispersion relation was first realized by P. R. Wallace [c1: 31] which implies that the E-k relation is linear for low energies near the six corners of the two-dimensional hexagonal Brillouin zone, shown in figure 1.2, leading to zero effective mass for electrons and holes [c1: 32] and thus electrons and holes near these six points, two of

which are in equivalent, behave like relativistic particles described by the Dirac equation for spin 1/2 particles [c1: 33,34].The equation describing the linear E-k relation is $E = \hbar v_F k$ where $k = \sqrt{k_x^2 + k_y^2}$ is called the wave vector and the Fermi velocity $v_F \sim 10^6$ m/s. Hence, the electrons and holes are called Dirac fermions, and the six corners of the Brillouin zone are called the Dirac points (shown in figure 1.2). Thus, intrinsic graphene is a semi-metal or zero-gap semiconductor.

Therefore, pure and structurally perfect graphene has shown outstanding electronic phenomena such as ballistic electron propagation with extremely high carrier mobility (~10^4 cm^2 V^{-1} s^{-1} at room temperature). However, the absence of a band gap in perfect graphene does not allow switching of graphene-based transistors with a high on-off ratio. Hence, graphene has to be modified either native or physically introduced defects [c1: 35] even when making basic devices and, even more, for manufacturing sophisticated circuits.

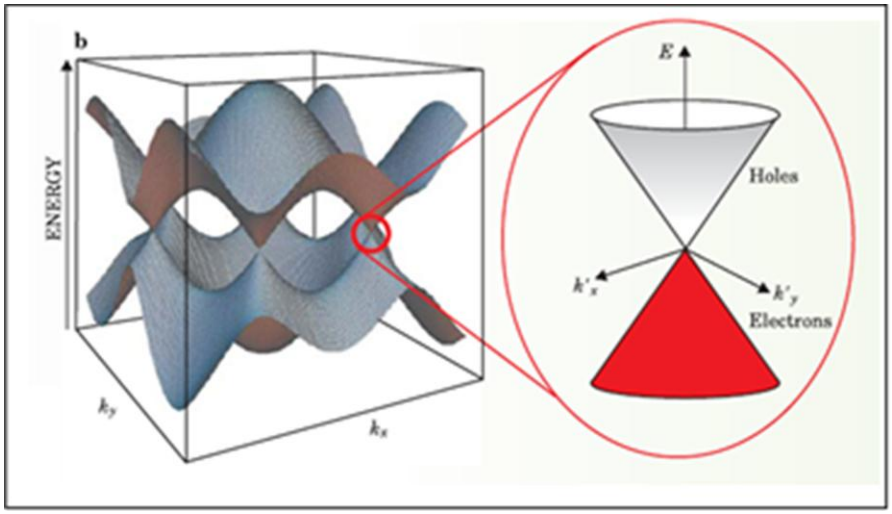

Figure 1.2: Graphene six Dirac points (left), Linear E-K diagram (right).

Graphene also exhibit remarkable sensitivity to detect individual dopants. Being a two-dimensional material its whole volume exposed to surface adsorbents, which maximizes their effect. Due to graphene's metallic conductivity a few extra electrons can cause notable relative changes in carrier concentration, n makes it an ideal candidate for sensing purposes.

1.2. MOTIVATION:

Since first reported in 2004 the synthesis of graphene by mechanical exfoliation technique, many methods have been developed to produce graphene [c1: 1]. Though this method, which is called scotch-tape method [c1: 1], is widely used in many laboratories to obtain pristine perfect structured graphene layer(s) for basic scientific research and for making proof-of-concept devices, it is not a suitable process to obtain large- scale graphene production for producing commercial graphene devices. A potential mass-production method to synthesis is graphene prepared by thermal decomposition of SiC wafer under ultrahigh vacuum (UHV), which is the focus on this thesis (Figure 1.3). In this process, Si atoms sublime off from the SiC substrate during annealing, leaving the C atom behind, this rearranges them to form graphene [c1: 36]. The epitaxial graphene growth on polar Si-face SiC is slow, leading to self-limiting 1-4 monolayer (ML) Bernal stacked films, while growth on the polar C-face is much faster, giving films >30ML thick, with mixed stacking. Growth on the non-polar faces of SiC also produces films >30ML thick [c1: 37]. Once a perfect single crystal of graphene is nucleated on SiC substrate, no further growth is possible, as the graphene lattice is so tightly packed that no subsequent Si can diffuse through the grown graphene layer to

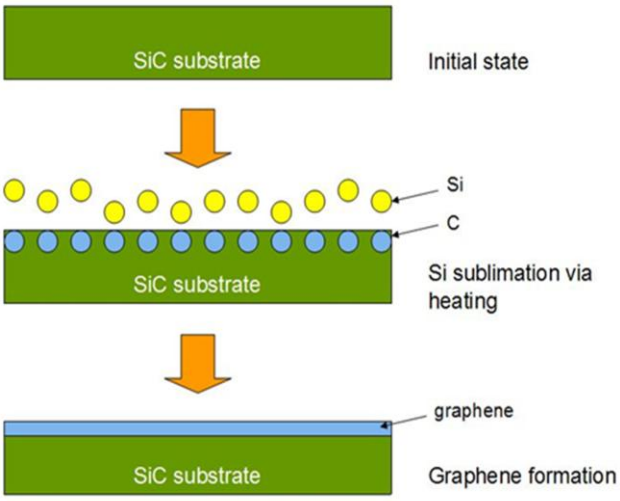

Figure 1.3: Epitaxial growth of graphene.

enable subsequent multilayer EG growth [c1: 37]. Thus, the growth of multilayer EG films must be mediated by Si-diffusion through defects and grain boundaries of the already grown EG layers.

These may be 1-dimensional point defects, as on the Si-face [c1: 38] and 2-dimensional defects such as stacking boundaries [c1: 37, 38], and/or cracks [c1: 39], as on the C-face, or grain boundaries, as on the non-polar faces [c1: 37] (Figure 1.4). Furthermore, these defects also provide high surface area and pathways for molecular adsorption,

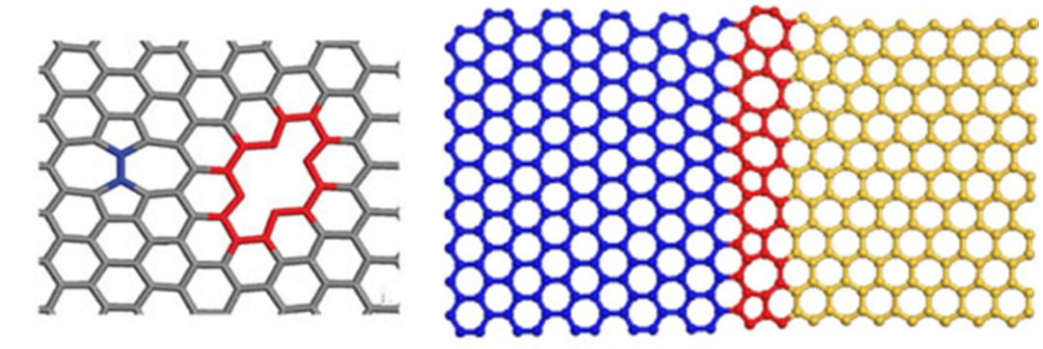

Figure 1.4: Point defects (left) and grain boundary/line defects (right) in graphene.

allowing graphene's application in sensing and energy storage/conversion. Hence, like in any other real material, structural defects that exist in graphene can dramatically alter its properties and influence the material quality. Defects can also be deliberately engineered into the graphene layers, to enable novel applications, which is a mainstay of the semiconductor industry.

1.3 MAJOR CONTRIBUTION OF THIS THESIS

The major contribution of this thesis is summarized as follows:

I)This work demonstrates the first numerical/analytical description of the Si-adatom kinetics and subsequent growth of multilayer epitaxial graphene on SiC substrates by thermal desorption of Si, a key technology in the commercialization/scaling of graphene. We show that Si adatom kinetics, as well as the defects present in the grown graphene layer, clearly influence the quality of subsequently grown graphene. This information may enable crystal growers to further refine the growth of epitaxial graphene on SiC.

II)A quantitative analysis on multilayer epitaxial graphene growth after the formation of first layer was performed based on a Deal-Grove like growth model, which assumes vertical diffusion of Si through these defects as the limiting factor for EG growth, is unsuitable for describing multilayer growth.

III)To quantify the experimental results, a modified BCF (Burton, Cabrera and Frank) model is introduced .In this model, defects in epitaxial graphene serve as sinks for Si desorption loss, taking the place of reactive sites such as step edges for nucleation and growth of crystals produced with external precursors. This analysis shows that the surface diffusion of Si atoms to the grain boundaries of EG limits the growth on c-plane

C-face and non-polar faces, rather than the purely vertical diffusion of Si through the grain boundaries described in the Deal-Grove model.

IV) The role of defects on the substrate on the epitaxial graphene growth on non-polar (a and m plane SiC substrates) was demonstrated for the first time. Hydrogen etching was performed prior to EG growth, a well-known method to reduce surface scratches and thereby improve the surface morphology on the nucleation surface of EG growth on these faces. This led to EG growth with better quality and higher mobility is also observed as compared to EG on un-etched substrates. The increase in mobility is justified by an increase in phonon lifetime contributing towards the minimization of scattering.

V) The sensing behavior of epitaxial graphene with more defects (C-face) was observed under the exposure of three (NH_3, NO_2 and N_2) distinguishable gases. By comparing the change in Ef under gas adsorption with the adsorbed impurity concentration as a function of EG thickness, the 3 gases were clearly distinguished, enabling a new paradigm for multi-modal gas sensing using optical interrogation of EG surfaces towards EG electronic or optical noses.

VI) A novel technique is introduced and established to grow multilayer thick (> 200 MLs) graphene on Si face SiC substrates, exploiting the Si-adatom removal from SiC surface using SiF_4 and subsequent Si out diffusion through defects present in grown graphene layers. A novel approach is also presented to estimate large number of graphene layers based on Raman and Infrared spectroscopy. This information may enable crystal growers to achieve thick graphene layers on Si face SiC substrates and characterize that for energy storage applications.

1.4. ORGANIZATION OF THESIS

The role of defects present in epitaxial graphene will be discussed over the next six chapters, towards material growth and also in device performances. Chapter 2 presents a brief overview of three major graphene synthesis techniques. The process of epitaxial graphene growth and characterization of the material at Clean Energy lab at University of South Carolina is also presented. A novel method to quantitatively analyze multilayer epitaxial graphene growth after the formation of first layer incorporating the influence of defects present in the first EG layer is presented in Chapter 3. Chapter 4 demonstrates the role of substrate defects towards epitaxial graphene growth on non-polar SiC substrates for the first time introducing hydrogen etching prior to growth. The growth model developed in chapter 3 was utilized to analyze the growth kinetics; the role of defect minimization on the electronic properties of the EG layers are also discussed. The sensing behavior of EG on C face(attributed to higher defect density as compared to EG on Si face)is demonstrated experimentally and theoretically in chapter 5.Finally, chapter 6 demonstrates a technique to achieve temperature controlled defect engineering in epitaxial graphene layers by introducing SiF_4 gas. Chapter 7 presents a summary of the research and accomplishments throughout the thesis.

1.5 PUBLICATIONS AND PRESENTATIONS

The publications and presentations by the author are listed in this section throughout the graduate study and research years at the University of South Carolina.

Publications (6 Journal [3 First Author], 8 conference presentations [5 First Author])

1. **Shamaita S Shetu**, S. Omar, K. Daniels, B. Daas, J Andrewes , S. Ma, T. S. Sudarshan, MVS Chandrashekhar, "Si-adatom kinetics in defect mediated growth of multilayer epitaxial graphene films on 6H-SiC" , *(Journal of Applied Physics,2013,Vol.114,Issue 16).*

2. **Shamaita S Shetu**, Tangali S Sudarshan, Tawhid A Rana, Kevin M Daniels, Haizheng Song, MVS Chandrashekhar, "Thick Defect-Engineered Multilayer Graphene on SiC using SiF_4" (*Manuscript submitted to Journal of crystal growth and design).*

3. **Shamaita S Shetu,**Tawhid A rana, Gomez hani, T. S. Sudarshan, MVS Chandrashekhar. "Influence of interfacial surface preparation by hydrogen etching on the growth kinetics of epitaxial grapheme on non-polar faces", (*Manuscript to be submitted to Applied Physics Letters).*

4. K. M. Daniels, **S. Shetu**, J. Staser, J. W. Weidner, C. Williams, T. Sudarshan, MVS Chandrashekhar,"Electrochemical Hydrogenation of Dimensional Carbon", *(GaN and SiC Power Technologies issue 3, Volume 58 ,ECS Transactions 2013).*

5. B. Daas, O. Sabih, **S. Shetu**, K. Daniels, S. Ma, T. Sudarshan, MVS Chandrashekhar , "Comparison of epitaxial graphene growth on polar and non-polar

6H-SiC faces: On the growth of multilayer films", (*Journal of Crystal Growth and Design*,20 12, Vol. 7, 3379-3387).

6. B. Daas, K. Daniels, **S. Shetu**, T.S. Sudarshan, M.V.S. Chandrashekhar, "Epitaxial Graphene Growth on non-polar SiC faces" , (*Material Science Forum ,2012*, Vol. 717-720 633-636).

Conference papers:

1. **Shamaita S Shetu**,Tawhid A rana, Gomez hani, T. S. Sudarshan, MVS Chandrashekhar. "Influence of Hydrogen Etching on Growth Kinetics of Multilayer Epitaxial Graphene on Non-Polar SiC Substrates " *Electronic Material Conference* ,Santabarbara, CA(2014)

2. **Shamaita S Shetu**, B. Daas, T.S. Sudarshan and MVS Chandrashekhar "Surface plasmon group velocity of c/60 using Graphene/SiC Ribbon Gratings: Shrinking optical components to electronic dimensions", *Electronic Material Conference* ,South Bend, IN(2013)

3. **Shamaita S Shetu**, B. Daas, K. M. Daniels, T.S. Sudarshan, GoutamKoley and MVS Chandrashekhar, "Selective Multimodal Gas Sensing in Epitaxial Graphene by Fourier Transform Infrared Spectroscopy", proceedings of *IEEE Sensors Conference* ,Baltimore ,MD (2013)

4. **Shamaita S. Shetu**, B. K. Daas, K. Daniels, T. S. Sudarshan, MVS Chandrashekhar "A Study on the growth mechanism of epitaxial graphene on polar and non-polar 6H-SiC faces" Electronic Material Conference (2012)

5. **Shamaita S Shetu,**M W K Nomani, Goutam Koley, MVS Chandrashekhar "Surface Adsorption and Charge Transport in Epitaxial Graphene on 6H-SiC" Electronic Material Conference (2011)

6. Kevin M. Daniels, **Shamaita S. Shetu**, J. Staser, J. W. Weidner, C. Williams, T. S. Sudarshan, MVS Chandrashekhar, "Electrochemical Hydrogenation of Dimensional Carbon", 244th ECS Meeting, San Francisco , CA (2013)

7. Kevin M. Daniels, **Shamaita S. Shetu**, J. Staser, J. W. Weidner, C. Williams, T. S. Sudarshan, MVS Chandrashekhar, "History Dependence of Reversible Electrochemical Hydrogenation of Epitaxial Graphene/SiC", 244th ECS Meeting, San Francisco , CA (2013).

CHAPTER 2

GRAPHENE GROWTH & CHARACTERIZATION

Graphene is a two dimensional crystal of carbon atoms arranged in a honeycomb lattice structure that may well serve as the building block for future carbon-based Nano-electronics. It has very fascinating physical properties such as tunable band gap, high crystalline quality, quantum electronic transport, extremely high mobility, high elasticity and electromechanical modulation [c2:1-6].

One of the biggest challenges in developing graphene based devices is how to synthesize it. There are many different techniques to grow graphene and all techniques differ in terms of their cost structure, volume production capability and ultimately, potential target markets. A recent report shows the comparative position of these techniques based on quality, cost

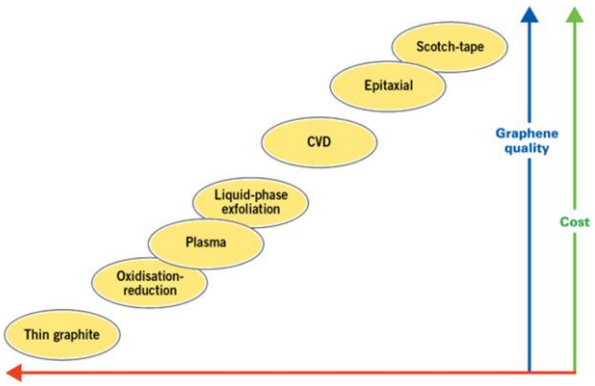

Figure 2.1: Graphene synthesis techniques based on quality, cost and scalability.

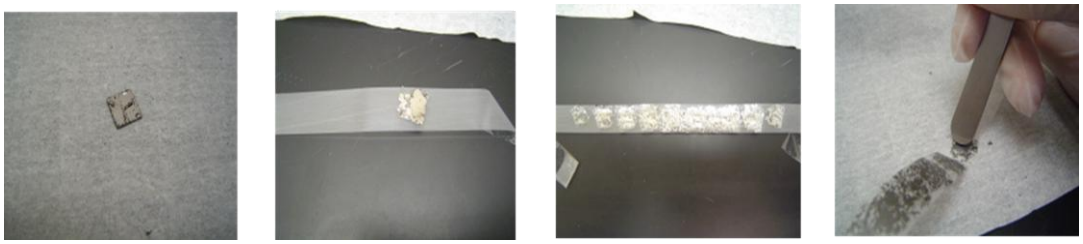

Figure 2.2: Step by Step peeling to get exfoliated graphene using scotch-tape.

and scalability[c2: 7] .In this chapter, we will discuss the top three graphene synthesis techniques which involve Scotch-tape or mechanical exfoliation technique, chemical vapor deposition (CVD) and epitaxial growth of graphene.

2.1: SCOTCH-TAPE/MECHANICAL EXFOLIATION TECHNIQUE:

Since discovery, graphene is limited to small sizes due to its production mostly by exfoliating graphite, a technique first demonstrated by a University of Manchester group in 2004. In this process, they repeatedly peeled off graphite crystals into increasingly thinner pieces using scotch tape (figure 2.2) [c2:8]. Then the tape with attached optically transparent graphene flakes was dissolved in acetone, and, after a few further steps, the flakes including graphene monolayers were deposited on a silicon wafer. This process enables to synthesize single layer graphene.

2.2: CHEMICAL VAPOR DEPOSITION (CVD) GROWTH OF GRAPHENE:

Recently, chemical vapor deposition (CVD) of graphene and few-layer graphene using hydrocarbons on metal substrates such as Ni and Cu has shown to be a promising technique .The growth is based upon cracking of gases at elevated temperature on the top of a metal catalyst. C atoms are dissolved in the catalyst and subsequently segregate out during cooling, yielding mono to few-layer graphene.

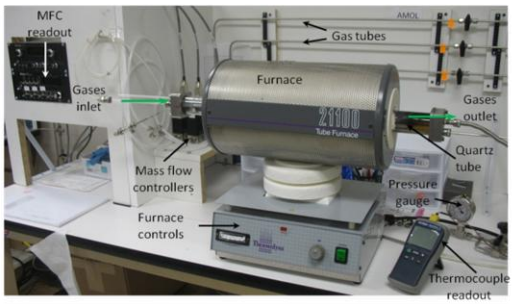

Figure 2.3: CVD Chamber for graphene.

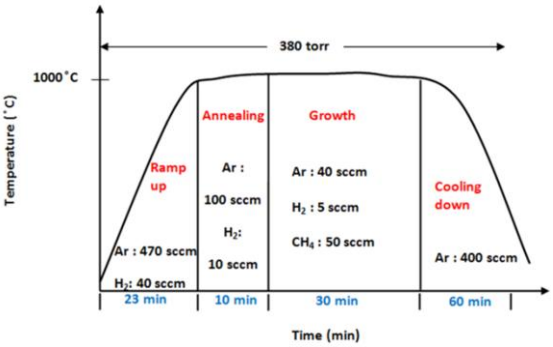

Figure 2.4: CVD growth temperature and pressure profile.

Graphene growth on nickel (Ni) is achieved by annealing at 800^0C with CH_4 environment in Chemical vapor deposition (CVD) [c2:9]. On the other hand, graphene growth on single crystal Cu (111) has been achieved by thermal decomposition of ethylene in an ultrahigh vacuum chamber.

It has been proposed that CVD growth of graphene on Ni/Cu is due to a C segregation [c2:10] or precipitation [c2:11] process and a fast cooling rate is suggested as critical for suppressing formation of multiple layers and thus obtaining graphene .Thus, the graphene films grown on Ni/Cu foil/film so far however are still not uniformly monolayer, i.e., they have a wide variation in thickness over the film area [c2:12]. Again since the metal substrate is conducting, electronic device applications require additional processes to remove the substrate [c2:13, 14]. The grown graphene can be transferred onto another insulating substrate by etching the metal substrate in an acid solution, but the transferred film usually contains defects such as breaks and wrinkles. However, we do not discuss details on the growth of CVD graphene since it is beyond the scope of this thesis. Here we show the growth stage and process parameters for the CVD graphene growth in NESL lab at USC.

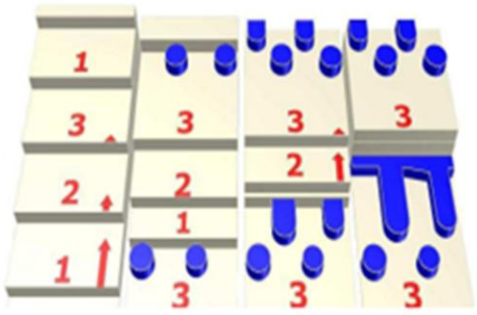

Figure 2.5: A growth model showing the process involved for the epitaxial growth of graphene.

2.3: EPITAXIAL GROWTH OF GRAPHENE:

A promising large area technique for graphene synthesis is epitaxial growth of graphene where a 4H or 6H-SiC substrate is annealed in high vacuum to produce epitaxial carbon layers. In this method, Si-C bond breaks and Si sublimes off from the SiC substrate since the sublimation rate of silicon is higher than that of carbon atoms .The carbon atoms left behind on the surface and then rearranges to form graphene layer [c2:15]. The growth process involves three basic steps such as (1)silicon desorption, (2)carbon diffusion and (3)island nucleation associated with high temperature [c2:16,17]. The growth sequence is shown [c2:16] schematically in the above figure. Three adjacent steps evaporate Si and release carbon as they are retracting. The retracting speed of step 1 is larger than the retracting speed of 2, which in turn is larger than the retracting speed of step 3. The initial islands begin to nucleate in the area exposed during the retraction of the first half of the terrace associated with the fast moving step 1. Because step 1 retracts faster it merges with step 2 to form a double SiC bilayer step. Before merging, the increased carbon released from the second half of the terrace associated with step 1 and the carbon released from step 2 combine

to form fingers. Eventually the last slow bilayer step 3 catches up to the retracting double step to merge into a triple bilayer step. However on the C face, EG growth is defect mediated, as defects are higher energies than the surface for Si to sublimes off leaving behind C atom to rearrange in honeycomb structure, graphene [c2:18].

2.4. EPITAXIAL GRAPHENE GROWTH AT CLEAN ENERGY LAB (CEL)

A schematic of the RF reactor furnace used to grow epitaxial graphene in Clean Energy Lab at USC is shown in figure 2.6.The reactor furnace is designed to achieve high quality epitaxial graphene growth at high vacuum. In general, epitaxial graphene (EG) growth by thermal decomposition of SiC at high temperature can be achieved in two different ways i) Growth at high pressure [c2:19-22] and ii) Growth at high vacuum (low pressure) [c2:23-25]. At high pressure (usually Ar environment), Si sublimation slows down from the SiC substrate allowing carbon atoms sufficient time to rearrange

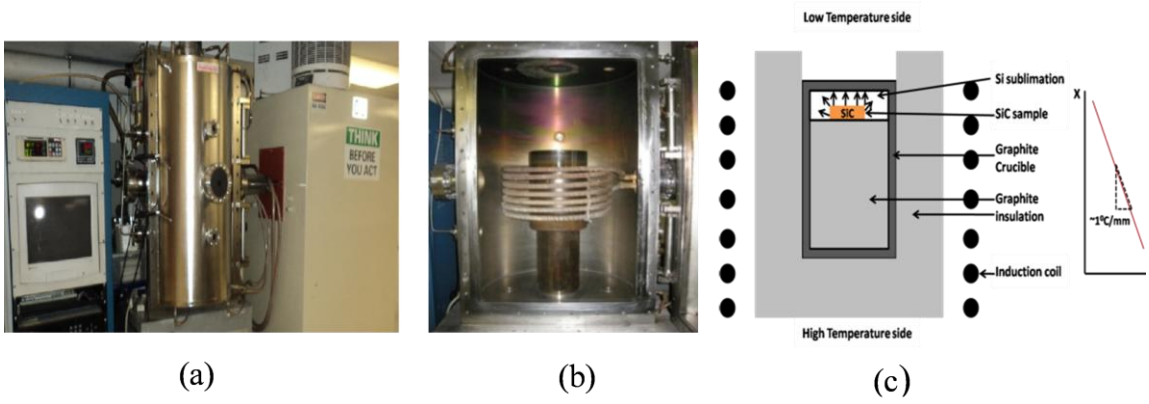

Figure 2.6: The RF induction furnace to grow epitaxial graphene on 6H-SiC (a) The outer view of the system. (b)An inner view of the furnace architecture. (c) Schematic illustration of the furnace. The large amount of graphite foam surrounding the graphite crucible, as well as the large thermal mass of the graphite crucible minimizes the thermal gradients (~1^0C/mm) and thermal transients in the system.

themselves to form a good quality crystal [c2: 20-22]. However, the slower Si-out diffusion rate necessitates higher growth temperatures (by ~300-400K) than with vacuum, which leads to significant step bunching in the underlying SiC substrate, leading to surface steps >10nm in some cases [c2: 21,26] on the Si-face. On the other hand, epitaxial graphene growth at high vacuum requires lower temperatures; which prevents step-bunching, leading to smoother surfaces, a potential advantage of vacuum growth over high pressure growth. Furthermore, the slow Si sublimation is accomplished through SiC substrate confinement in a small region, where the silicon vapor fills up the container/susceptor, preventing further loss of silicon [c2:24]. This method of controlling the silicon/carbon environment over SiC is called the "sublimation sandwich" technique [c2:27]. At the same time, small thermal gradients are maintained so that $SiC(s) \rightarrow Si(g)+C(s)$ equilibrium is achieved with minimal Si loss from the substrate to form good quality EG layers. Thus, in Clean Energy Lab (CEL), all EG growth are achieved by using a small, inductively heated hot-wall container for EG growth (Figure 2.6). The gradients are minimized by heating the entire enclosing container, which is then placed in a large thermal reservoir of insulating graphite foam, typical for a SiC bulk growth reactor [c2:28]. Our growth conditions were optimized for Si-face growth to produce uniform EG bilayers of quality as good as or better than those grown using Ar-mediated growth at high pressure [c2:25]. However, the growth on the C-face is of poorer quality than with Ar-growth, as the Si-loss rate is much higher in vacuum, due to defects in the EG, as we will show in the next chapter.

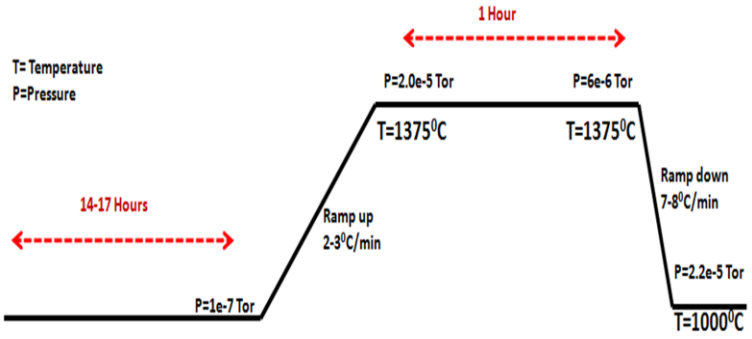

Figure 2.7: The process parameters for optimized growth condition

In our experiments, EG was grown on commercial CMP polished 4H/6H SiC substrates, nitrogen doped or semi insulating substrate. Samples were degreased using trichloroethylene (TCE), acetone and methanol. They were then rinsed in DI water for three minutes. The samples were finally dipped in HF for two minutes to remove native oxide and rinsed with DI water before being blown dry. They were then set in the crucible in an inductively heated furnace in both face up and face down orientation where high vacuum was maintained ($<10^{-6}$ Torr) and baked out at 1000^0C for 13 to 15 hours. The temperature was slowly raised to the growth temperature (1250-1400°C). All growths were performed for different time duration depending on the requirement and cooling to 1000^0C at a ramp rate of $7\sim8^0$C/min, eventually to room temperature. Slow temperature ramps were utilized to minimize thermal stress on the samples.

In this way we can produce good quality uniform epitaxial graphene on SiC. Then we confirm the quality of graphene through several characterization techniques.

2.5: GRAPHENE CHARACTERIZATION TECHNIQUES:

There are several characterization techniques used to confirm graphene such as Raman characterization, Atomic force Microscopy (AFM), X-ray photoelectron

spectroscopy (XPS), Infra-Red (IR) spectrometer, ARPES (angled resolved photo electron spectroscopy), LEEM (low energy electron microscopy) etc.

At USC we mainly use the following characterization techniques to confirm graphene.

1. X-ray photo electron spectroscopy(XPS)
2. Atomic force microscopy(AFM)
3. Raman Spectroscopy.
4. Fourier Transform Infrared (FTIR) spectroscopy.

2.5.1. X-RAY PHOTOELECTRON SPECTROSCOPY (XPS):

After each growth EG film thickness was extracted from the X-ray photoelectron spectroscopy (XPS) spectrum. The measurements were conducted using a Kratos AXIS Ultra DLD XPS system equipped with a monochromatic Al Kα source. The energy scale of the system was calibrated using a Au foil with Au4f scanned for the Al radiation and a Cu foil with Cu2p scanned for Mg radiation resulting in a difference of 1081.70 ± 0.025eV between these two peaks. The binding energy is calibrated using a Ag foil with $Ag3d_{5/2}$ set at 368.21 ± 0.025eV for the monochromatic Al X-ray source. The monochromatic Al Kα source was operated at 15 keV and 150 W. The pass energy was fixed at 40 eV for the detailed scans. A charge neutralizer (CN) was used to compensate for the surface charge.

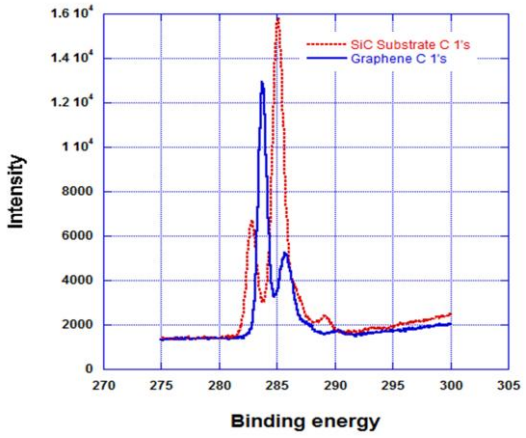

Figure 2.8: XPS Characterization of EG.

As shown in the figure above, we measured the C1s and Si2p peaks both on the EG samples and the substrate to extract the film thickness. To overcome any instrumental error both normal and 70^{o} beam incidence angles were considered while taking the XPS spectra. For EG on Si face the C 1s XPS spectra consists of three components, one SiC bulk component located at 283.7± .08eV, one is from the graphene overlayer at ~284.4eV while the other is broad and weak at ~285.5eV arising from C-C bonding in a $6\sqrt{3}X6\sqrt{3}$ interfacial buffer layer [c2:29]. Thus to estimate the EG thickness after the interfacial buffer layer for EG on Si face graphene overlayer peak intensity was normalized to the peak intensity arising from SiC bulk component as described earlier[c2:30].

For EG on C-face and non-polar faces , no interface related component is evident as opposed to Si face . For thinner layers <10ML, the C 1s spectra are dominated by two components, one of which is attributed to the SiC bulk and another is due to graphene overlayers and the thickness is estimated as a similar manner for EG on Si face. For thicker layers, the peak due to SiC bulk component disappears from the EG C 1s spectra while the Si2p peak is still significant. Therefore, the C1s peak was normalized

to the Si2p peak, from which the thickness was determined as described elsewhere [c2:31, 32] by the following equation.

$$ln \frac{I_G/S_G}{I_S/S_S} = e^{-\frac{d}{\lambda Cos\phi}} \qquad (2.1)$$

Where,

I_G= Peak area intensity of the graphene overlayer component from C 1s spectra for the EG samples.

I_S= Peak area intensity of SiC bulk component from C 1s spectra/Si 2p spectra for the EG samples/SiC Substrate.

λ= inelastic mean free path at that kinetic energy when intensity is in peak (here kinetic energy is 1202ev. Corresponding to this λ=2.1nm)

Φ=the emission angle(measured with respect to surface normal)

d=thickness of the Graphene layer

S_G and S_S are the relative sensitivity factors corresponding to graphene samples and substrate. To obtain the relative sensitivity factor for the Si2p peak, the thickness values using only the C1s peak intensities (C1s(graphene overlayer component)/C1s(SiC bulk component)), were correlated with the thickness for the same layers determined by comparing the C1s and Si2p peaks i.e. (C1s(graphene overlayer component)/Si2p).

2.5.2. ATOMIC FORCE MOCROSCOPY (AFM):

The surface morphology of EG films were characterized by Atomic force microscopy (AFM) modeled as Nano Scope SPM Dimention-3100. Tapping mode was used to scan 2.5umX2.5um window size on several positions on a sample. Different growth orientation exhibits different surface morphology originates from the growth

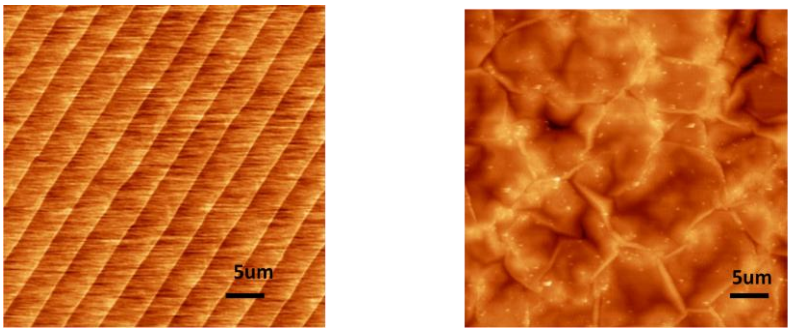

Figure 2.9: AFM image of EG on SiC substrates (left) Si-face,(right)C-face.

mechanism. Such as for EG on SiC, Si-face shows step features arising from the step flow mechanism[c2:33] whereas C face shows different surface morphology compared to Si face, arises from defect mediated growth mechanism. Both Si and C face growth also depends on face up or face down orientation, the way it was placed in the RF reactor [c2:34].The figure below describes the surface morphology for EG grown on Si face and C face respectively.

The crystal Coherence length (L_g) or grain size for the EG layers can also be determined by taking a statistical measurement of 10 individual grains of each sample from the phase image of the tapping mode AFM image as described in the literature [c2:35].In this method, 10 grains were chosen randomly from approximate area coverage of 70% from a representative AFM image size to adequately sample the surface.

2.5.3. RAMAN CHARACTERIZATION:

A micro-Raman setup with laser excitation wavelength at 632nm and a spot size of ~2µm was used to obtain the Raman spectroscopy of the epitaxial graphene. The Raman system was calibrated using the known Si peak at 520.7cm^{-1}. Reference blank

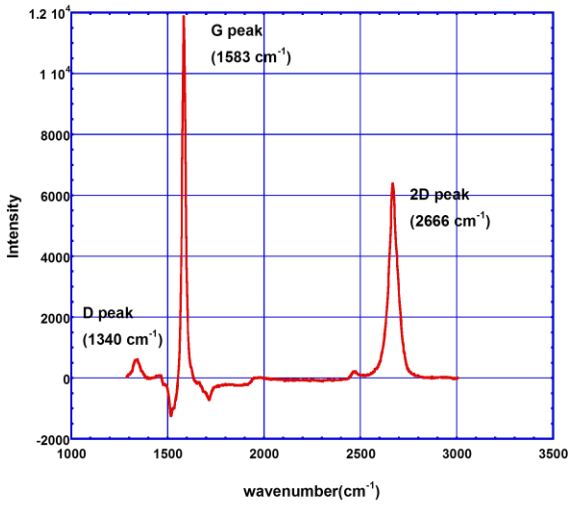

Figure 2.10: Raman Characterization of EG.

substrate spectra were scaled appropriately and subtracted from the EG spectra to show only the graphene peaks [c2:36].Raman was used as an indication of G (1585cm^{-1}), D(1345cm^{-1}) and 2D(2650cm^{-1}) peak which are due to in plane vibration, disorder and double resonant respectively [c2:37].The ratio of the integrated peak intensities of the D-peak to the G-peak (I_D/I_G) gives an indication of disorder/defects present in EG layers. The disorder ratio is inversely proportional to the cluster diameter or in plane coherence length, L_g (nm) [c2:38].

$$L_g = (2.4\times10^{-10})\lambda_l^4\left(\frac{I_D}{I_G}\right)^{-1} \qquad (2.2)$$

Where λ_l is the Raman incident laser wavelength (632.817nm) and I_D and I_G are the integral area of the Raman peak. From these measurements, the EG defect density can be directly estimated by [c2:39]

$$n_D(cm^{-2}) = 10^{14}/(\pi L_g)^2 \qquad (2.3)$$

The 2D-peak in graphene is an indication of the stacking of the material. Ideal Bernal stacked graphite has a split asymmetric 2D-peak, each sub-peak corresponding to the AB stacking that broadens graphene's linear electron dispersion. Turbostratic graphite i.e. graphite that is well-oriented, but rotationally disordered, gives a symmetric peak, due to a breaking of the A-B stacking that causes a split-peak [c2:40].In addition, the ratio of 2D/G peak intensities provides an indication of the thickness of EG [c2:41].

2.5.4. FOURIER TRANSFORM INFRARED (FTIR) SPECTROSCOPY:

In general, the EG thickness is estimated from the XPS spectra as discussed earlier. However, for films >~35ML thick, the thickness of graphene layers is ~12nm which is much greater than the inelastic mean free path for C1s and Si2p X-ray photoelectrons ~10nm, it is not possible to extract the thickness by XPS.

Therefore, we adopt another approach to extract the thickness of the EG layers by Fourier Transform Infrared Spectroscopy (FTIR) [c2:42]. This relies on the fact that more conductive graphene layers are more reflective in the infrared[c2:43]. Thus, from a reflectance spectrum, the conductivity can be determined[c2:43]. For thick films, which are electrically neutral (far from the substrate>>1ML screening length in graphene [c2:44]), the carrier concentration, n, is known. Thus, if the carrier mobility, μ, can be estimated using Raman [c2:45], the total thickness in ML, N, can be estimated from the relationship:

$$\sigma\ (FTIR) = Nnq\mu \qquad (2.4)$$

At room temperature, n=2x8x$10^{10}$$cm^{-2}$/ML, assuming a neutral layer, where the factor of 2 comes from equal concentration of electrons and holes. The carrier mobility can be

estimated from the phenomenological μ-2D Raman width correlation established by Robinson et. al. [c2:45]. Therefore, the lone fitting parameter is N, enabling reasonable confidence in the measurements.

FTIR reflectivity measurements are performed using a Galaxy Series FTIR-5000 spectrometer in an incidence angle of 40^{o} over the wavelength 2.5μm to 25μm using a blank SiC substrate as the reference. We considered the reflectance at a low value of $500cm^{-1}$ to minimize apparent decrease in reflectance for non-specular reflections, damping from carrier scattering, and increase in conductivity from interband transitions at higher frequencies [c2:43] .Thus, we estimated the differential reflectance of graphene as we vary the no of layers with this approach as shown in Figure 2.11 for a $\mu=500cm^{2}/Vs$.

The MATLAB code for the thickness estimation as attached in Appendix-1.Thus by matching the differential reflectance obtained from FTIR experimental data EG thickness for thicker layers can be estimated.

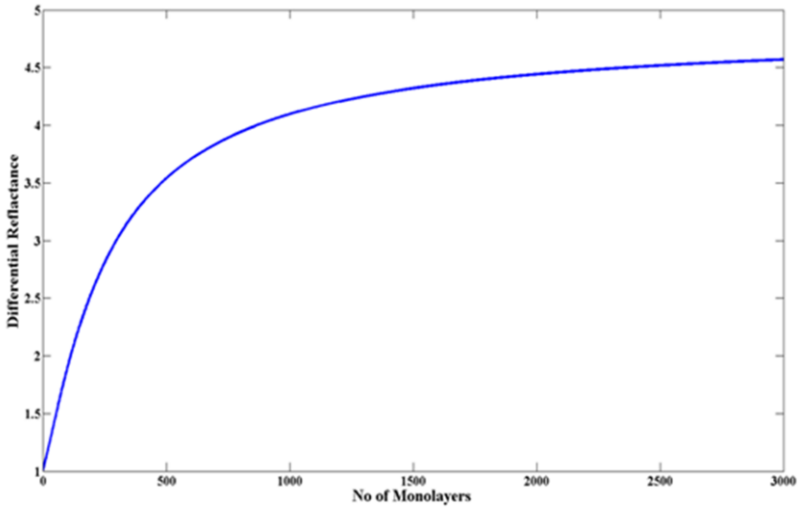

Figure 2.11: Variation of total differential infrared reflectance spectra with graphene thickness (i.e. no of graphene monolayers).

CHAPTER 3

DEFECT MEDIATED MULTILAYER EPITAXIAL GRAPHENE GROWTH

In this chapter, a quantitative study is presented on the growth of multilayer epitaxial graphene (MEG) by solid-state decomposition of SiC on polar (c-plane Si and C-face) and non-polar (a and m plane) 6H-SiC faces, with distinctly different defect profiles. It is very important to have a clear understanding about the growth mechanism of EG on SiC as there may be several factors that may limit the quality of graphene layers that form on SiC. A fairly detailed discussion about nucleation of carbon atoms in single layer epitaxial graphene on polar Si-face and C-face has been studied [c3:1-3].A comparative study on the growth of multilayer epitaxial graphene on polar and non-polar faces based on crystallographic structure is also reported [c3:4].Thus to realize the insight of multilayer EG growth a quantitative analysis has been done on multilayer epitaxial graphene growth on polar (c plane Si and C face) and non-polar (a and m plane), after the nucleation of the first layer. The MEG growth rates are slower than expected from a mechanism that involves Si loss from an open and free surface, and much faster than expected for the nucleation of a defect-free EG layer, implying that defects in the EG play a critical role in determining the growth kinetics. We show that a Deal-Grove growth model, which assumes vertical diffusion of Si through these defects as the limiting factor for EG growth, is unsuitable for describing multilayer growth. Instead, we introduce a lateral ‘adatom’ diffusion mechanism for Si out-diffusion, based on a modified BCF (Burton, Cabrera and Frank) model.

In this model, defects in epitaxial graphene serve as sinks for Si desorption loss, taking the place of reactive sites such as step edges for nucleation and growth of crystals produced with external precursors. This analysis shows that the surface diffusion of Si atoms to the grain boundaries of EG limits the growth on c-plane C-face and non-polar faces, rather than the purely vertical diffusion of Si through the grain boundaries described in the Deal-Grove model. However, for Si-face c-plane growth, diffusion of Si to the defects, as well as desorption of Si at the grain boundaries are both relevant, leading to a different temperature trend compared to the other faces. This distinct qualitative difference is ascribed to point-defects in Si-face growth, as contrasted with line defects/grain boundaries on the other faces. The size of the EG grains correlates with the surface diffusion length extracted from this model. The longer a Si adatom diffuses, the higher the quality of the grown EG film, an insight that provides valuable information on Si adatom kinetics for optimizing EG growth. We also discuss the applicability of this model to growth of multilayer EG in an argon ambient at atmospheric pressure.

3.1. THE GROWTH OF MULTILAYER EG FILMS: ROLE OF DEFECTS

Once a perfect single crystal of graphene is nucleated on SiC substrate, no further growth is possible, as the graphene lattice is so tightly packed that no subsequent Si can diffuse through the grown graphene layer to enable subsequent multilayer EG growth (Figure 3.1). Since Si cannot diffuse out through a grown EG layer, [c3:4] the grain boundaries/defects, nucleated during the initial stages of growth, provide alternate pathways for Si out-diffusion from the SiC crystal underneath.

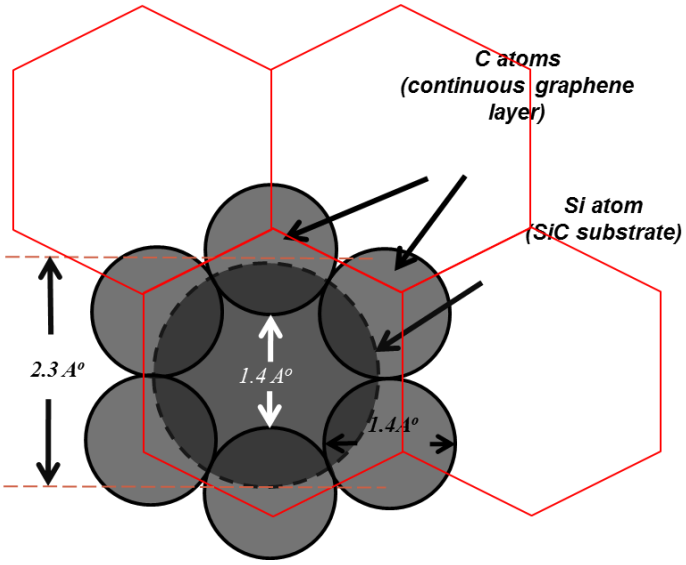

Figure 3.1: A schematic representation Si (g) & C(s) atoms during EG growth. Since Si atoms are bigger in size they cannot diffuse through graphite lattice.

Thus, the growth of multilayer EG films must be mediated by Si-diffusion through defects and grain boundaries of the already grown EG layers. These may be 1-dimensional point defects, as on the Si-face [c3:5] and 2-dimensional defects such as stacking boundaries, and/or cracks [c3:6], as on the C-face, or grain boundaries, as on the non-polar faces [c3:4].

Hence, we study the mechanism of Si out-diffusion through the defects in the grown EG layers in relation to the experimental growth rates. We consider Si diffusion along both vertical and lateral directions and conclude that the lateral surface diffusion kinetics determines the growth rates of multilayer EG. We propose a lateral diffusion model based on the BCF theory of crystal growth and use it to quantitatively describe the influence of defects on the growth rate of multilayer EG. We also show that the growth on the Si-face of 6H-SiC is distinctly different than the other (both polar and non-polar) faces due to the different dimensionality of the defects on the Si-face.

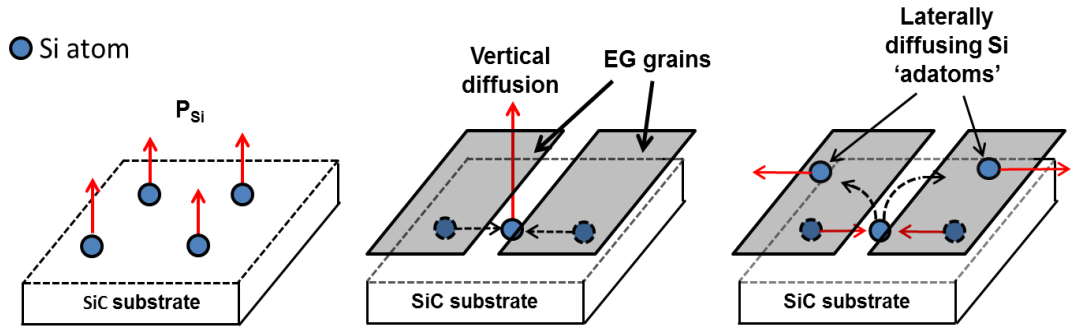

(1) (2) (3)

Figure 3.2: The three different potential modes for Si sublimation from SiC substrate towards multilayer EG growth.(1) Si sublimation from an open and free surface. (2)Vertical diffusion limits the multilayer EG growth (Deal-Grove regime). $D_{vertical} << D_{lateral}$
Vertical out-diffusion flux of Si atoms through the grain boundaries/defects is faster than lateral 'surface' diffusion flux. (3) Lateral diffusion of Si on the terrace to the grain boundaries/defects limits the multilayer EG growth (Surface diffusion regime). $D_{lateral} << D_{vertical}$.

3.2. EPITAXIAL GRAPHENE GROWTH ON POLAR (C PLANE) AND NON-POLAR SIC SUBSTRATES:

In this study, EG on a-plane (EG-a) and m-plane (EG-m) was grown on commercially available a and m plane 6H-SiC substrates from Aymont Technology chemical mechanical polished (CMP) and nitrogen doped ~$10^{17}/cm^3$. Polar faces (c-plane Si face and C-face) of 6H-SiC from Cree were also chosen to grow epitaxial graphene in the same run at different temperatures under similar growth condition. The samples were diced to 1cm×1cm pieces and then degreased using trichloroethylene (TCE), acetone, and methanol, respectively, followed by a rinse in DI water. The samples were finally dipped in dilute HF for two minutes to remove native oxide and

rinsed with DI water before being blown dry. They were then set in the crucible in an inductively heated furnace and baked out at 1000^{o}C for 13 to 15 hours in a high vacuum environment (<10^{-6} Torr). This temperature was slowly raised to the growth temperature (1300°C -1450°C), optimized condition for c-plane growth. In every growth, in addition to a and m plane sample, one Si face c-plane and one C-face c-plane sample was placed for comparison. All growths were performed for 60 minutes before cooling to 1000^{o}C at a ramp rate of 7~8^{o}C/min and eventually to room temperature. We used this slow temperature ramps to minimize thermal stress on the samples as optimized for c-plane growth [c3:6]. We observed that under the same growth conditions, both EG-m and EG-a layers were thicker than their corresponding polar c-plane samples while EG-m showed thicker growth than EG-a.

The measured growth rates (ML/hr.) of epitaxial graphene grown on polar and non-polar 6H-SiC faces is plotted in figure 3.3 as a function of temperature. The experimental growth rates are much lower than the expected growth rate of EG layers due to Si loss from an open and free surface due to the presence of the grown EG layers (discussed later in section 3.3.1). While Si-face growth is less dependent on the growth temperature, C-face and non-polar faces show a significant increase in growth rate with temperature. This indicates a different growth mechanism in Si face, arising primarily from point defects [c3:5], rather than grain boundaries, limiting the growth in Si face as will be discussed later.

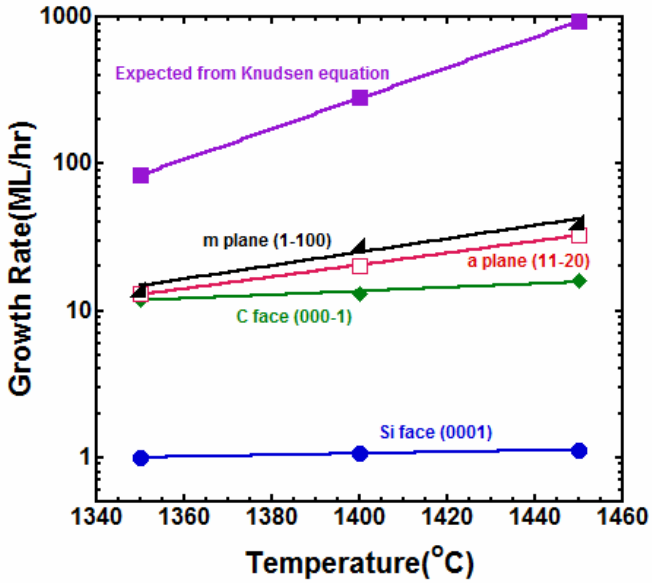

Figure 3.3: Arrhenius plot of growth rate (ML/hr.) vs. temperature (^{o}C). The expected growth rate from Si sublimation off an open and free surface is much higher than the experimental growth rates indicative of selective, defect-mediated diffusion limited multilayer EG growth.

The difference in surface morphology of EG-a, EG-m and EG-c layers grown at temperatures 1350^{o}C, 1400^{o}C and 1450^{o}C is shown in Figure 3.4. At all growth temperatures, EG on Si-face shows step like features [c3:7, 8], with no obvious grain boundaries and the steps becoming more prominent with increasing growth temperature. Hence, L_G (nm) for EG layers grown on this face is estimated by taking a statistical measurement of the steps from the phase image of tapping mode AFM, in addition to the Raman measurements discussed below. C-face EG layers show clear grain boundaries, some of which are wrinkles (rising up above the surface), while others are depressions (dipping below the surface). EG grown on non-polar faces exhibit nano-crystalline graphite like features. Both non-polar faces show surface roughness ~3nm, indicating poorer surface morphology as compared to Si-face EG with rms roughness<0.5nm and C-face EG with rms roughness~1nm.

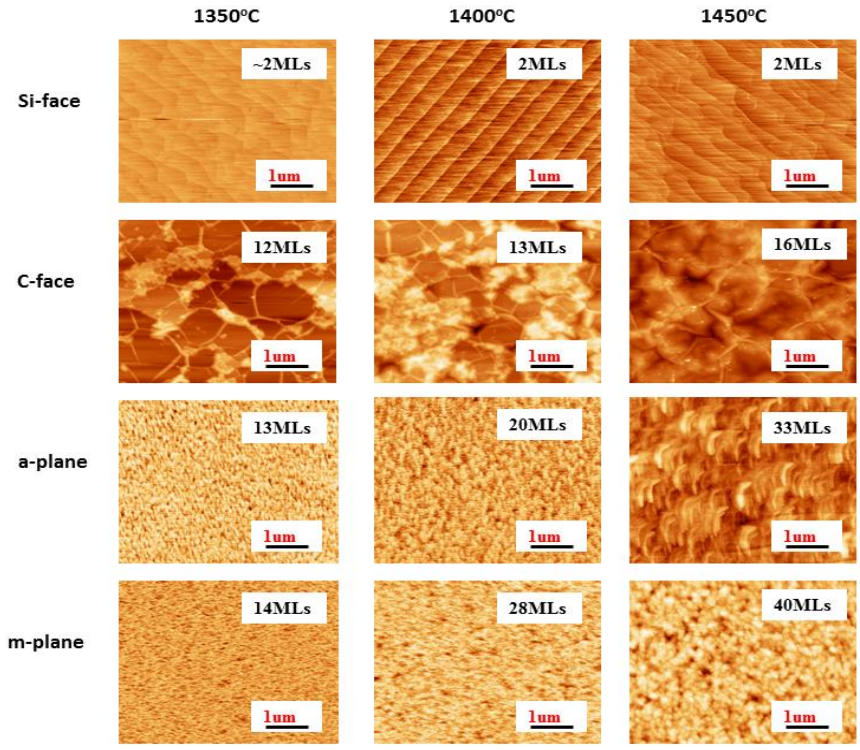

Figure 3.4: AFM image of epitaxial graphene grown on a, m and c plane 6H-SiC substrates at three different growth temperatures 1350°C, 1400°C and 1450°C respectively. EG on a-plane and m-plane samples show nano-crystalline graphite like features whereas EG on Si face show step like features and clear grain boundaries are observed for EG on C-face.

The crystal coherence length or grain size, L_G of the EG layers grown on polar and non-polar faces of 6H-SiC are estimated by Atomic Force Microscopy (AFM) and Raman Spectroscopy. AFM tapping mode was used to scan 2.5umX2.5um window size on several positions on a sample. Then, the crystal coherence length(L_G) or grain size for the EG layers grown on polar and non-polar faces of 6H-SiC was determined by taking a statistical measurement of 10 individual grains from each sample from the phase image of the tapping mode AFM image as described elsewhere [c3:9].

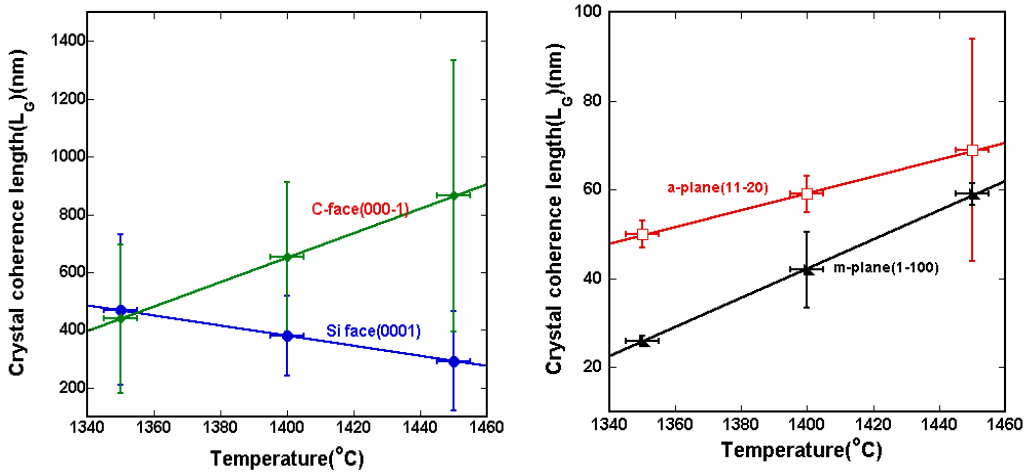

(a) (b)

Figure 3.5: Crystal coherence length (L_G) (nm) of EG on (a) polar (Si-face and C-face) and (b) non-polar faces (a and m plane) of 6H-SiC.

Finally, the disorder ratio (I_D/I_G) [c3:6] from Raman spectroscopy is used to calculate the in-plane coherence length, L_G(nm) [c3:10], by the following equation:

$$L_G = (2.4 \times 10^{-10})\lambda_l^4 (\frac{I_D}{I_G})^{-1} \quad (3.1)$$

Where λ_l is the Raman incident laser wavelength (632.817 nm) and I_D and I_G are the integral areas of the D and G Raman peaks, respectively.

There is generally a discrepancy between the crystal coherence lengths obtained by Raman, and by AFM (Figure 3.5 (a), (b)), due to differences in the nature of the defects between the various films. C and Si faces show significant differences between the 2 techniques, whereas a and m planes show better agreement. For Si-face EG with point defects [c3:5], L_G decreases with temperature, as Si-face EG layers are epitaxially registered [c3:11] to the thermally mismatched SiC substrate [c3:12]. This leads to build in compressive strain in the EG, as seen clearly in the blue-shifted Raman G-peak at ~1590cm^{-1}. Thus, when cooling from a higher temperature after growth, the epitaxially registered EG layer undergoes greater thermal stress, leading to generation

of a higher density of point defects. However, for c-plane C-face and non-polar faces, L_G increases with temperature (Figure 3.5), since these layers are not epitaxially registered to the substrate, and are therefore unstrained, leading to minimal thermal stress when cooling from different temperatures. This increase is attributed to greater energy available to form C-C bonds, enabling formation of larger networks of aromatic rings, an assertion borne out by the fact that high temperature annealing has been used to form high quality graphitic material with lower densities of defects [c3:13]. In all these experiments, the thicker the film, the smaller L_G is, as the grain boundaries/defects facilitate the desorption of Si-adatoms, speeding up the growth, the key observation that led to the proposal of the growth model discussed later.

Hence, to obtain a standard quantitative grain size/crystal coherence length for each temperature in this study, the AFM and Raman measurements were interpolated from a linear fit of these measurements over the entire temperature range .The measured values and the linear fit taken into account for the estimation of crystal coherence length, L_G is shown and C-face samples (Figure 3.6). All L_G values in this chapter are estimated in a similar manner. The error bars were estimated from the difference between the L_G values from AFM and Raman spectroscopy.

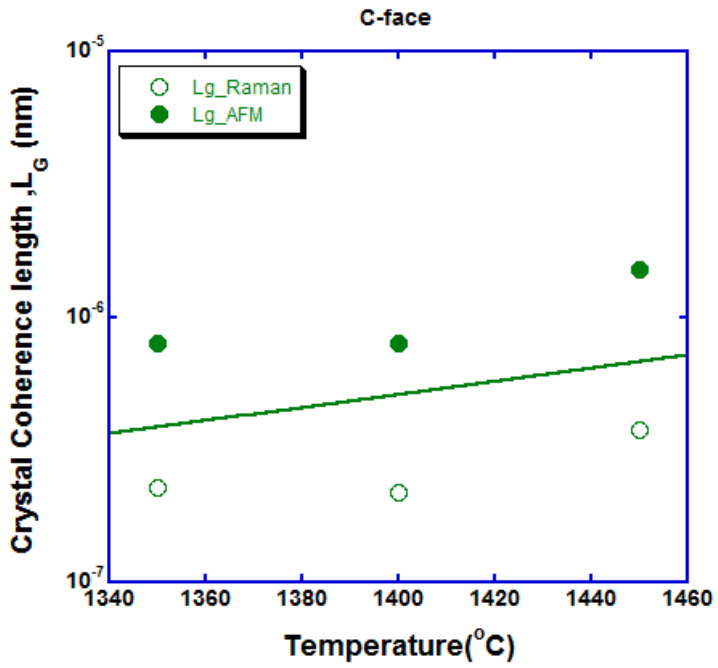

Figure 3.6: Crystal coherence length (L_G) (nm) interpolation from a linear fit between AFM and Raman values for C-face. A similar manner was utilized to extract the L_G for Si-face, a-plane and m-plane samples.

3.3. EPITAXIAL GRAPHENE GROWTH FROM AN OPEN AND FREE SiC SURFACE: DEFECTS LIMIT THE GROWTH

As discussed above, multilayer EG growth precedes by defect-mediated out-diffusion of Si atoms through the grown graphene layers. However, it is useful to consider the growth of EG from a free and open SiC surface, assuming that the grown graphene does not limit desorption of Si from the SiC surface (Figure 3.2 (1)). The Si flux from an open 6H-SiC surface for EG layer formation in vacuum [c3:4] can be obtained from Knudsen's equation from the kinetic theory of gases [c3:14]

$$\text{Flux}=\frac{P_{Si}}{(2\pi m_{Si}k_BT)^{1/2}} \qquad (3.2)$$

Where, m_{si}, k_B, T are the mass of one Si molecule ($4.658\text{x}10^{-23}$g), Boltzmann constant and absolute growth temperature respectively. This Si flux leaves C atoms behind, which serve as the carbon source for EG growth. We calculated the partial pressure of

Si over SiC, P_{Si} for our experimental temperatures 1350°-1450°C from the Clausius-Clapeyron relation [c3:15].

$$P_{Si} = e^{-\frac{\Delta H_{Si}}{RT}} \qquad (3.3)$$

Where ΔH_{Si} is specific latent heat of sublimation of Si adatoms for the reaction $SiC_{(s)}=Si_{(g)}+C_{(s)}$ at 298K (125±3 Kcal/mole) [c3:16], R is ideal gas constant and T is the growth temperature in K.

Thus, the expected growth rates of EG layers due to Si loss from an open and free surface in ML/hr. are plotted in Figure 3.3 by considering the Si flux during the growth interval (1hr) and atomic density of graphene (~$3.7x10^{15}cm^{-2}$). All the experimentally measured growth rates (also plotted in Figure 3.3) are much lower than expected from equation (2), which describes EG growth by Si sublimation off an open and free surface. The slowing down of the growth can be explained by the fact that multilayer EG growth proceeds only through selective, defect-mediated out-diffusion of Si atoms. The defects, therefore, play a critical role in mediating the growth of multilayer films.

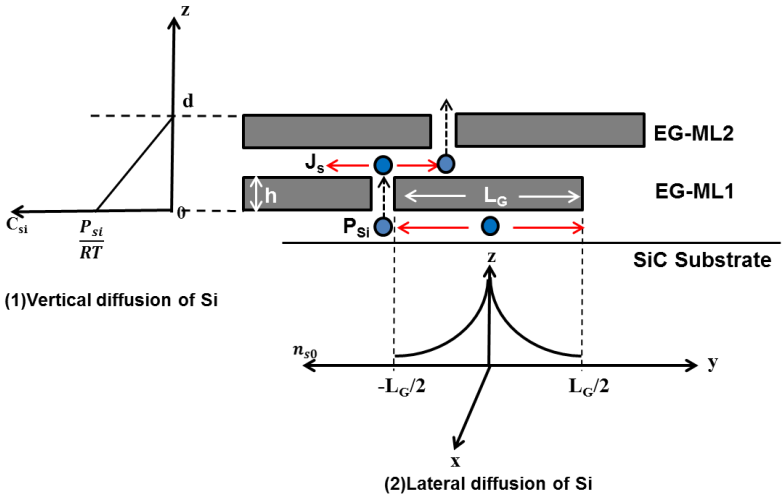

Figure 3.7: Diffusion limited growth model for multilayer epitaxial graphene. (1)The growth is limited by vertical diffusion of Si through the grain boundaries. (2) Lateral diffusion of Si to the grain boundaries limits the multilayer EG growth.

3.4. DEAL-GROVE MODEL: VERTICAL DIFFUSION OF Si THROUGH DEFECTS AS LIMITING FACTOR

The simplest way to account for the influence of defects towards Si out-diffusion mechanism is to use a Deal-Grove (Figure3.7 (1)) vertical diffusion limited growth model based on the crystal coherence length, L_G (Figure 3.6) where we assume the crystal coherence length represents the grain size of the EG layers .Since Si cannot diffuse out through a grown EG layer, the grain boundaries/defects in that layer, nucleated during the initial stages of growth, provide pathways for Si out-diffusion from the SiC crystal underneath (Figure 3.7 (1)). We require for this model that the lateral diffusion to the defects is very fast compared to the vertical diffusion through the defects (Figure 3.2 (2)), as has been measured in diffusion study in graphite, where in-plane diffusion is much faster than out-of-plane diffusion [c3:17].

The EG layer grown on a-plane shows slightly larger grains as compared to the m-plane, while the polar face (Si face & C-face) EG layers have even larger L_Gs. Therefore, after the formation of the first EG layer, the Si out-diffusion is expected to be the fastest for m-plane EG films, producing thicker layers compared to a-plane, Si face and C-face. Also, increasing the temperature increases the rate of Si sublimation and hence the out-diffusion of Si atoms which, in turns, increases the grown EG film thickness .The effective Si diffusion flux is considered to travel from the grown SiC/EG layers to the top EG/ambient interface through the grain boundaries in the newly formed EG layers.

According to this model (Figure 3.7 (1)); Si-flux through the grain boundaries is,

$$J_1 = k\frac{\partial d}{\partial t} \qquad (3.4)$$

Where d is the thickness of EG layers in cm(i.e. d=no. of Monolayers×.335× $10^{-7}cm$), $\frac{\partial d}{\partial t}$ is the growth rate in cm/sec which can be obtained from experimental growth rate in ML/hr by setting t=3600s, corresponding to 1 hour of growth time and considering the thickness of single graphene layer (0.335× 10^{-7}cm). This equation expresses the conservation of mass in the EG growth process. Each Si-atom lost contributes one C-atom to the EG/SiC surface for growth of EG. Therefore, k (~1.13x10^{23} cm^{-3}) is the atomic density of a single EG layer. The Si-flux coming out from the SiC substrate can also be expressed with Fick's first law of diffusion. The diffusion flux coming from the substrate,

$$J_2 = D_{Si}\frac{C(0)-C(d)}{d} \qquad (3.5)$$

Where D_{Si} is the diffusion coefficient of Si in (cm^2/sec), C (0) is the initial concentration of Si atoms at the surface of SiC substrate, C (d) is the concentration of Si atoms at the top of the graphene layers. The boundary conditions are;

$$C(0) = C_{Si} \quad \text{and} \quad C(d) = 0 \qquad (3.6)$$

The initial concentration of Si atoms, C_{Si} is estimated from the ideal gas law;

$$C_{Si} = \frac{P_{si}}{RT} \qquad (3.7)$$

Where P_{Si} is the vapor pressure of Si over SiC, R is the ideal gas constant and T is the absolute temperature in K.

The growth of EG must satisfy continuity of the Si-flux. In other words the diffusion flux coming out from the substrate should be equal to the diffusion flux coming out through the grain boundaries (Figure 3.7(1)). Thus continuity forces;

$$J_1 = J_2 ,$$

This gives: $k\frac{\partial d}{\partial t} = D_{si}\frac{C_{Si}}{d}$

And hence Diffusion constant D_{Si} in (cm^2/sec),

$$D_{Si} = k \times \frac{\partial d}{\partial t} \times \frac{C_{Si}}{d} = k \times \frac{\partial d}{\partial t} \times \frac{P_{Si}}{dRT} \qquad (3.8)$$

We can extract the diffusion coefficient, D_{Si} from the above equation. Consequently the growth activation energy can be obtained from the Arrhenius plot of D_{Si}, expressed as

$$D_{Si} = D_0 e^{-E_A/RT} \qquad (3.9)$$

Where D_0 is the maximum diffusion coefficient, E_A is the activation energy for diffusion in eV.Figure 3.8 shows the Arrhenius plot of diffusion constant D_{Si} as a function of temperature for all the faces extracted from the Deal-Grove like growth model. The plot exhibits negative activation energy, which is unphysical in the Deal-Grove model. Therefore the assumption of vertical diffusion of Si through the grain boundaries as the limiting factor for multilayer EG growth becomes invalid. In the following section, we incorporate the effect of lateral Si-adatom diffusion, which was ignored in this section (as described above), enabling a physically meaningful description of the Si-diffusion kinetics as related to the measured growth rates.

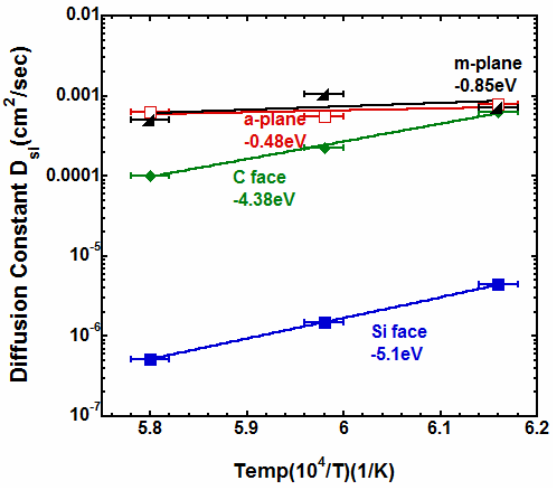

Figure 3.8: Arrhenius plot of the diffusion constant (D_{Si}) estimated from Deal-Grove like growth model as a function of temperature. The activation energies extracted from

the plot are negative; makes vertical diffusion limited multilayer EG growth unphysical.

3.5. BCF MODEL: INCORPORATING LATERAL DIFFUSION OF Si TO THE GRAIN BOUNDARIES/DEFECTS

Since Burton, Cabrera and Frank (BCF) laid the theoretical foundation for the dynamics of atomic steps [c3:18]; several modifications of BCF theory have been studied to discuss growth mechanisms [c3:19-23]. Here, we analyzed the epitaxial growth of EG based on the BCF theory with some modifications described below, where we add the lateral diffusion of Si to the grain boundaries, ignored in the Deal-Grove like model discussed in the previous section. We develop a simplified 1-D surface diffusion model, where EG layers have a height, h of 3.35×10^{-7}cm, corresponding to the thickness of a single EG layer, and an average straight-line distance between defects/grain boundaries of L_G (Fig. 3.7 (2)).

The assumptions here are:

1. The surface is 1D. We will discuss the implications of this in the results.
2. The distance between the defects is uniform (experiment shows this to be a reasonable approximation)
3. The grain boundaries/defects present in the grown graphene layer act as perfect sinks for the Si adatoms once they reach those paths.
4. Lateral diffusion of Si can be in SiC/EG interface or EG/EG interface, and can be slow (Figure 3.2(3)).

In this system, the SiC crystal surface is thermally decomposed and Si adatoms diffuse along the surface. Some of the adatoms reach the grain boundaries of the graphene layer above and diffuse through them, leaving a C-rich surface behind. The formation of multilayer EG must also satisfy the continuity of the Si-flux i.e. the Si-flux toward the grain boundaries must be equal to the Si-flux through the grain boundaries. This continuity is expressed by

$$-D_s \frac{d^2 n_s(y)}{dy^2} = \frac{-n_s(y)}{\tau_s} \qquad (3.10)$$

Where $n_s(y)$ is number of Si adatoms per unit area on the surface, τ_s is mean surface residence time of adatoms, and D_s is the surface Si-diffusion coefficient. Using the boundary condition $n_s = n_{s0}$ at $y = \pm \frac{L_G}{2}$, the adatom concentration on the terraces, $n_s(y)$ can be given as a solution of (10):

$$n_s(y) = n_{s0} \frac{\cosh(y/\lambda_s)}{\cosh(L_G/2\lambda_s)} \qquad (3.11)$$

Where n_{s0} is the adatom concentration at equilibrium and λ_s is the surface diffusion length of adatoms; an average length for adatoms to migrate on a "step-free" surface before desorption given by the following equation:

$$\lambda_s = (D_s \tau_s)^{1/2} = a \exp\left(\frac{E_{des} - E_{diff}}{2k_B T}\right) \qquad (3.12)$$

Where a, k_B and T are the proportionality constant, Boltzmann constant and absolute temperature respectively, E_{des} and E_{diff} are the activation energies for desorption and lateral surface diffusion in eV.

Hence, the Si-adatom flux at y=0,

$$J(0) = \frac{n_s(0)}{\tau_s} = \frac{n_{s0}}{\tau_s \cosh(\frac{L_G}{2\lambda_s})} \qquad (3.13)$$

Although it is difficult to estimate $\frac{n_{s0}}{\tau_s}$ independently, this ratio can be expressed by the equilibrium vapor pressure of Si over SiC, P_{Si} using Knudsen's equation from the kinetic theory of gases, $\frac{n_{s0}}{\tau_s} = \frac{P_{Si}}{(2\pi m_{Si} k_B T)^{1/2}}$ (3.14)

Where m_{Si} is the mass of the Si adatom .Since the desorption probability of migrating adatoms at grain boundaries is assumed to be unity, the horizontal velocity is given by the following equation:

$$\nu_{horizontal} = \frac{J(0)}{n_0} = \frac{n_{s0}}{n_0 \tau_s Cosh(\frac{L_G}{2\lambda_s})} \quad (3.15)$$

Where n_0 is the atomic density of graphene (3.8×10^{-15} cm^{-2}). To convert from a horizontal growth velocity to a vertical growth rate , R_G ; the conversion factor $\frac{h}{L_G}$ is used as the Si-adatom diffuses through the crystal coherence length ,L_G and desorb through the thickness of EG layer (h) for subsequent EG layer formation .Therefore, the no of graphene layers,

$$d(t) = R_G t = \nu_{horizontal} \times \frac{h}{L_G} \times t = \frac{n_{s0}}{n_0 \tau_s Cosh(\frac{L_G}{2\lambda_s})} \times \frac{h}{L_G} \times t \quad (3.16)$$

We extracted the values of λ_S from the above equation and estimated the activation energy difference on different planes by using Eqn. (12).A power law fit to the extracted λ_S and L_G , L_G shows a similar behavior for all the planes as λ_S of the Si adatoms are much smaller than L_G (Figure 3.9). However, the estimated relative activation energy (E_{des}-E_{diff}) (Figure 3.10) reveals the dissimilarity in the growth mechanism in Si face than C-face and non-polar faces arising from the different defect profile (point defects in Si face and defects/grain boundaries in C-face and non-polar faces).

In this modified BCF model, lateral surface diffusion of Si adatoms to the grain boundaries/defects is considered the limiting factor to realize multilayer EG growth. The lateral surface diffusion length of the Si adatoms, λ_s extracted by fitting growth rates to equation (16), is plotted in Figure 3.9 against crystal coherence length, L_G. For all the faces λ_s increases with L_G; although they are much smaller than L_G. Therefore, the longer a Si-adatom diffuses, the higher the quality of the grown EG film, an insight into EG growth on SiC that may enable further optimization of this process.

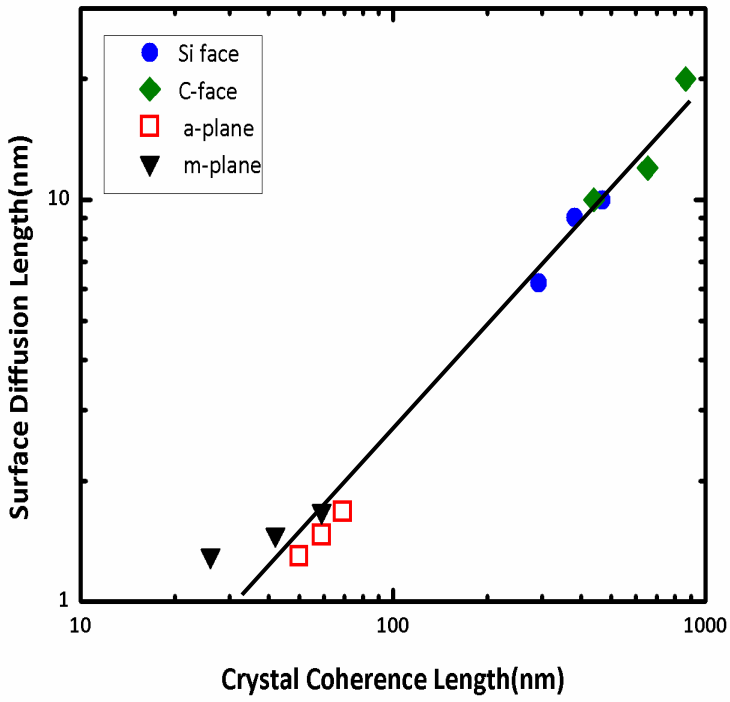

Figure 3.9: Surface diffusion length (nm) extracted from the lateral diffusion limited growth model is plotted against crystal coherence length (nm).

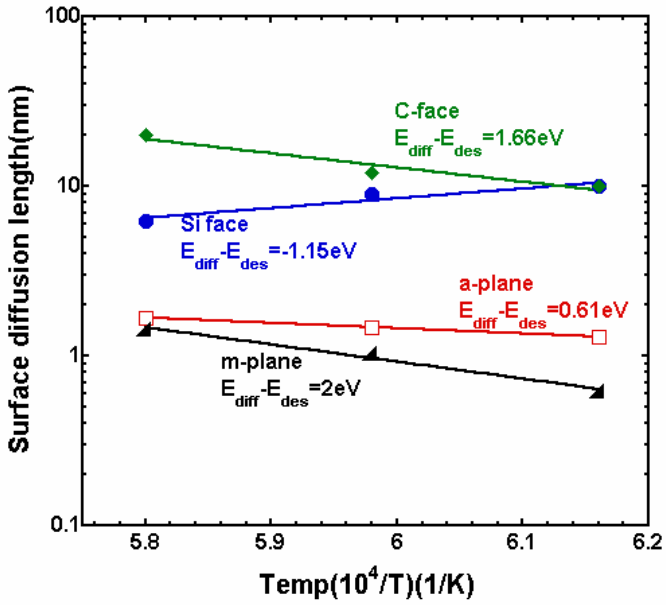

Figure 3.10: Arrhenius plot of surface diffusion length (λ_s) for EG grown on polar (c plane) and non-polar (a & m plane) vs. temperature.

Figure 3.10 shows the effective activation energy for lateral surface diffusion of Si adatoms, E_{diff}-E_{des} extracted from the Arrhenius plot of λ_s vs. T. For C-face and non-polar faces, $E_{des} < E_{diff}$, as assumed in the model with clearly observable large extended 1D line defects. Thus, in this case, the lateral surface diffusion of Si adatoms to these defects/grain boundaries plays the primary role in limiting the growth of EG.

For EG on the C-face, the SiC defect sites on the C-face participate in EG growth [c3:3] leading to multiple orientations [c3:24] unlike EG on the Si-face. This, along with non-uniform stacking sequence (AA, AB) in the C-face EG film [c3:25] gives rise to large area grain boundaries which act as effective sinks for Si adatoms i.e. growth mode (3) dominates (Figure3.2).To facilitate multilayer EG growth, Si adatoms from the SiC crystal beneath the first EG layer must travel far enough to reach the defects/grain boundaries to escape i.e. $E_{diff} > E_{des}$.

The non-polar faces also exhibit $E_{diff}>E_{des}$. Due to the lack of a hexagonal SiC template [c3:4] a continuous EG film cannot be grown on a/m planes. Rather, scattered island/grains form as a result of the faster growth rates, with 1D line defects bounding each grain, as on the C-face. As shown in Figure 3.9, L_G is smaller in these faces compared to the polar faces resulting in a greater density of grain boundaries /desorption sites. This reduces E_{des}, as the grain boundaries act as sinks for Si-adatoms. However, due to the greater roughness of these films, they also possess a higher E_{diff} that must be overcome, as this roughness presents an impediment to lateral Si-adatom diffusion. Despite this greater roughness, the growth rates for non-polar faces the multilayer EG growth rate is higher than the polar faces due to the large density of defects present. Therefore, again, growth mode (3) (Figure 3.2) dominates.

However, for Si face grown EG, $E_{des} > E_{diff}$ showing that there is a barrier to Si desorption, which breaks down the assumption that defects are perfect sinks for Si diffusion. We ascribe this anomalous behavior to 0D point defects [c3:25] in the grown Si-face EG, which are very small, making the diffusion of Si through them difficult. Therefore, for Si-face EG growth, both vertical (Figure 3.2 growth mode (2)) and lateral diffusion of Si-adatoms (Figure 3.2 growth mode 3) play a role in slowing down the growth.

We believe this model is applicable to growth of EG in argon at atmospheric pressure,[c3:26]with the modification that the flow of Si-loss after leaving the EG/SiC surface, transitions from molecular (Knudsen) flow at high vacuum, to fluid (diffusive) flow at atmospheric pressure, which is much slower. Therefore, the growth rate is limited not just by defects within the EG layer, but also by Si-desorption from the

EG/ambient surface. This will slow down growth further, enabling longer diffusion lengths on the surface, improving the material quality (Figure 3.10). Therefore, we expect that there will be a modification to $E_{des,}$ which will change due to an additional contribution from slower desorption of Si-adatoms from the EG surface. If this desorption from the EG/ambient surface in an argon ambient becomes the bottleneck for growth, it is conceivable that the growth mode shifts from modes 2,3 in Figure 3.2 to mode 1, with the modification that the Si-loss from the surface takes place through diffusive transport rather than Knudsen transport. This behavior may be responsible for the high quality, low defect densities obtained by researchers in an argon ambient [c3:26], enabling self-limiting growth to 1ML when optimized. However, a detailed investigation of argon ambient grown EG is required to clarify whether this growth mode transition has indeed occurred.

3.6. SUMMARY:

In summary, we presented a quantitative study on multilayer EG growth and discussed the growth mechanism of multilayer EG films comparing the growth on polar and non-polar faces of 6H-SiC. The growth on all the faces is slower than expected from a free and open SiC surface. The non-polar faces with higher growth rate have smaller L_G compared to the polar faces. Thus the multilayer EG growth was first attributed to be limited by Si desorption through grain boundaries/defects in the grown EG layers that allow the escape of Si from the SiC substrate as Si cannot diffuse through a perfect graphene lattice. We showed that lateral diffusion of Si to the grain boundaries contributes to limit the growth rate of EG. This process is quantitatively

analyzed with a model based on BCF theory. This analysis showed a clear correlation between surface diffusion length λ_s and $L_{G,}$ the crystal coherence length and EG film quality, an important result for the optimization of EG growth. This shows that increasing the surface migration length on Si adatoms increases the crystal coherence length, and slows down the growth rate. Multilayer EG growth for Si face ($E_{des}>E_{diff}$) is found to be different than growth on the other faces ($E_{des}<E_{diff}$), attributed to the different dimensionality of the defects on these faces. We discuss the applicability of this model to growth of multilayer EG in an argon ambient at atmospheric pressure.

CHAPTER 4

INFLUENCE OF SUBSTRATE PREPERATION ON EG GROWTH KINETICS

Graphene, a two dimensional (2D) array of carbon atoms arranged in honeycomb lattice structure with unique electronic, optical and mechanical properties may overcome the physical limits silicon faces as transistors shrink to ever-smaller sizes - providing solutions for future electronics[c4:1,2].A promising way towards wafer-scale graphene production is to grow epitaxial graphene (EG) by the thermal decomposition of polar (c plane) and non-polar (a and m plane) SiC substrates in ultra-high vacuum or Ar environment at high temperatures[c4:3, 4].In order to have a better control on EG growth towards large scale graphene production for graphene based electronics it is very important to understand the growth kinetics of EG on SiC substrates. This chapter presents the role of initial surface preparation by hydrogen etching prior EG growth on EG growth kinetics and electronics properties of EG layers. Hydrogen etching prior to EG growth increased EG grain size up to 5x while the thickness decreased by >2x, with layers as thin as ~5ML. Analysis of the Si-adatom kinetics shows that increased diffusion lengths due to defect minimization on the SiC surface are responsible for increasing the grain size, leading to a weaker temperature dependence of the growth rate. The best films have an estimated carrier mobility as high as ~1500 cm^2/Vs, which we attribute to the turbostratic stacking and consequent massless linear dispersion, demonstrating the promise of graphene based electronics on non-polar SiC substrates.

4.1. DEFECT INFLUENCED MULTILAYER EPITAXIAL GRAPHENE GROWTH:

We have shown previously in chapter 3 that defects in the grown EG are the key controlling factors that determine the growth of multilayer epitaxial graphene [c4:5, 6]. EG on non-polar faces exhibit higher growth rate with smaller grain sizes and higher defect density as compared to polar faces [c4:6].A modified BCF model adopted for multilayer growth realization on these faces shows that the surface diffusion of the Si adatoms towards defects limits the EG growth rate as compared to vertical diffusion through the defects. According to this model, the surface diffusion length of the Si adatoms, λ_s represents an average length Si adatoms diffuse laterally on the surface before desorption. The smoother the nucleation surface for graphene growth, it will enhance lateral diffusion of Si adatoms and increase λs. We observed that, as the surface diffusion length of the Si adatoms increases, EG grain size also increases contributing towards better quality EG [c4:6].

In this work, we investigate the role of initial surface preparation towards EG growth kinetics by hydrogen etching the polar (c plane Si face and C face) and non-polar (a and m plane) 6H- SiC substrates prior to EG growth. SiC being a refractory solid, the physical properties of the surface depends a lot on how it is treated due to the low mobility of the surface atoms [c4:7]. Hydrogen etching, as a well-known method to remove defects introduced on the surface during wafer preparation can provide a different primary surface for EG growth on SiC [c4:8]. Typically, for polar faces (Si face and C face) the optimized EG growth have obtained without hydrogen etching. However, for EG growth on non-polar 6H-SiC substrates we observed that hydrogen etching initiates EG growth at lower temperatures and EG grain size increases with slower growth rate as

compared to films grown without hydrogen etching.

Hence, in this chapter we present a detailed study on the influence of hydrogen etching on Epitaxial graphene (EG) grown on non-polar 6H-SiC substrates. Non-polar (a and m plane) 6H-SiC substrates does not carry spontaneous and piezoelectric polarization charges as opposed to polar (c plane Si face and C face) SiC [c4:9], which might lead to a higher carrier mobility in EG due to the minimization of polarization scattering. Moreover, EG on non-polar SiC lacks the interfacial buffer layer [c4:10,11], present in EG on Si face, responsible for the system's high electron-doping and contributes to the degradation of the electrical properties of the overlying graphene [c4:10].Thus EG on non-polar faces show a great potential for graphene based electronic applications.

4.2. EXPERIMENTAL DETAILS:

EG samples were synthesized on commercially available chemical mechanical polished (CMP) nitrogen doped ~$10^{17}/cm^3$ a-plane and m-plane 6H-SiC substrates from Aymont Technology. At the same time polar (Si-face and C-face) Semi-insulating 6H-SiC substrates from II-IV materials were also used as reference samples to confirm the optimized growth for our system. The samples were diced to 1cm x1cm pieces and then degreased using trichloroethylene (TCE), acetone and methanol respectively, followed by a rinse in DI water. The samples were finally dipped in dilute HF for two minutes to remove native oxide and rinsed with DI water before being blown dry. The substrates were then underwent an ex-situ H_2 etching at 1550^oC for 20-60 minutes in a hot-wall Chemical Vapor Deposition (CVD) reactor [c4:12]. Atomic force microscopy (AFM) tapping mode is utilized to scan 2.5umX2.5um window size on several positions on a

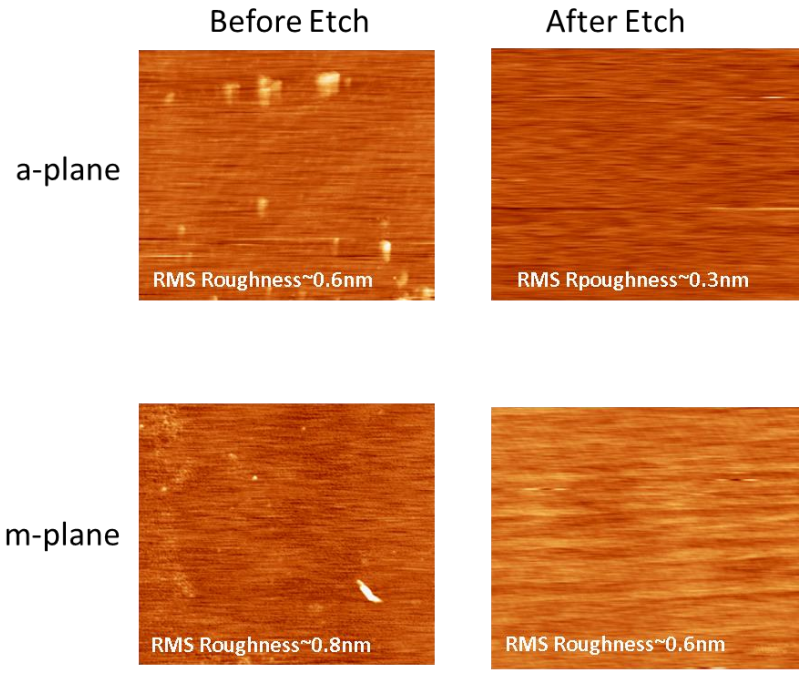

Figure 4.1: The surface morphology of a-plane and m-plane substrates before and after hydrogen etching. The Z-scale range is ~ 10nm for all these images depicted above. After etching a smooth etched surface is achieved indicated by a reduction in RMS surface roughness.

sample to investigate the surface morphology of the substrates before and after hydrogen etching.

Figure 4.1 corresponds to the surface morphology of a-plane and m-plane before and after hydrogen etching. Unlike Si face, no steps are visible on non-polar SiC substrates. After etching the particulates and other surface contamination disappear from the substrate, clearly evident in the images. A reduction in RMS surface roughness is also observed in etched samples than as received clean sample, indicating a smoother nucleation surface for EG growth.

The EG growth was then carried out in our inductively heated furnace at CEL at the growth temperatures (1300^{o}C-1450^{o}C) .After each growth AFM measurements were utilized to characterize EG surface morphology. The EG film thickness was extracted using X-ray photoelectron spectroscopy (XPS). The Raman spectrum of graphene with

its characteristic peaks (D, G and 2D) confirms the presence of graphene for the samples under consideration and graphitization quality. Furthermore, The crystal coherence length (L_G) or grain size for the EG layers grown on non-polar faces of 6H-SiC were also calculated from the ratio of the integrated peak intensities of the D-peak to the G-peak (I_D/I_G) .Since, the Raman 2D peak width is strongly correlated with graphene carrier mobility, we estimated the EG carrier mobility for each samples by utilizing 2D FWHM, established previously [c4:4].

4.3. INFLUENCE OF HYDROGEN ETCHING ON EG GROWTH:

AFM images of EG on both etched and non-etched substrates at the growth temperatures of 1300, 1350, 1400 and 1450^{o}C is depicted in Figure 4.2. Without etching the surface morphology exhibits nano-crystalline graphite like features whereas EG growth on etched substrates appears to occur in patches that coalesce with depressions on the surface. The surface roughness for these EG films is of ~7nm as compared to EG on un-etched substrates with surface roughness values of ~3nm, indicating a rougher surface morphology after substrate etching. This can be due to the thermal stress occurred in the substrates by performing ex-situ H_2 etching at elevated temperature (1550^{o}C) in a hot-wall CVD furnace with subsequent cooling at room temperatures followed by raising the substrates to the growth temperatures at the RF reactor furnace for EG growth . A more detailed study is required on this which is beyond the scope of this dissertation.

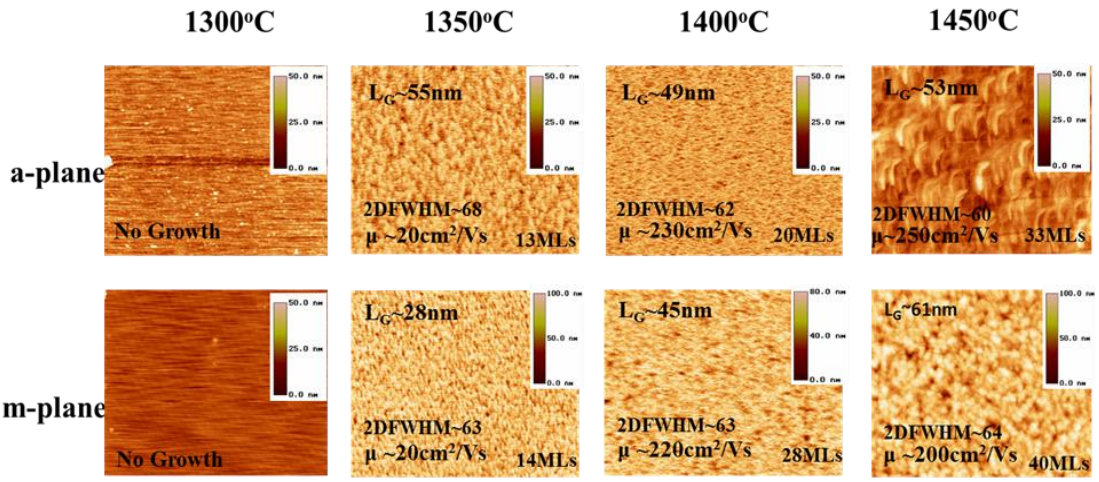

(a)EG surface morphology grown on un-etched non-polar (a and m plane) 6H-SiC substrates.

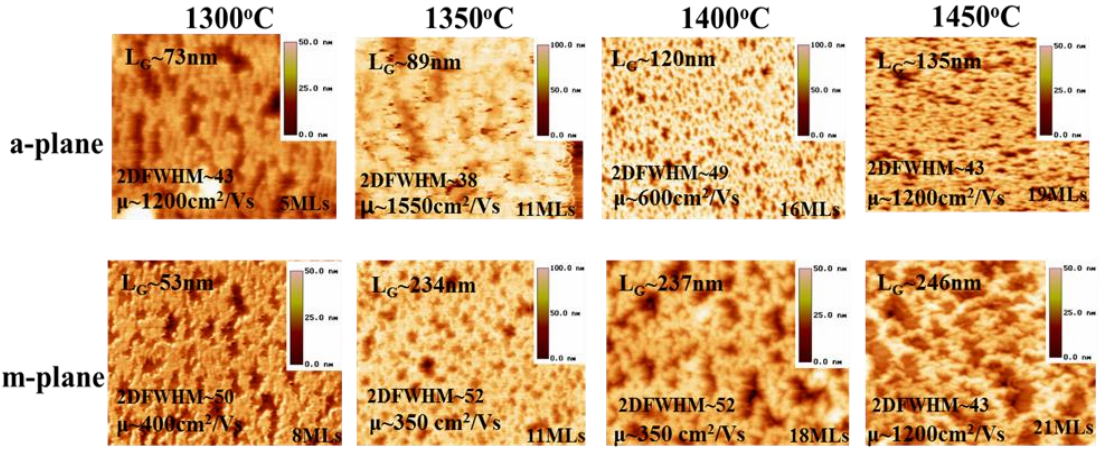

(b)EG surface morphology grown on hydrogen etched (a and m plane) 6H-SiC substrates.

Figure 4.2: AFM image of epitaxial graphene on a and m plane substrates before(a) and after(b) etching at four different growth temperatures: 1300, 1350, 1400 and 1450^{o}C, respectively. AFM image results the surface morphology of graphene on these substrates. The EG grain size, L_G is estimated from Raman spectroscopy. The Raman 2D FWHM is also presented which is utilized to extract the mobility for these growths as depicted in the images.

Hydrogen etching initiates EG growth at lower temperature i.e.1300^{o}C rather than 1350^{o}C and contributes lowering the EG growth rate on these faces as shown in Figure 4.2. Due to hydrogen etching prior EG growth, the nucleation surface undergoes a

surface reformation with ordered 1x1 surface reconstructions as has been observed on non-basal plane SiC surfaces[c4:13] leading to a change in the initial surface energetics. Since EG nucleation and growth is highly dependent on SiC surface energetics [c4:14], the change in surface energy on the substrates due to hydrogen etching prior to EG growth might lead to EG formation at a lower temperature. As growth temperature increases, the EG grain size increases on etched substrates, showing a similar trend as observed in EG without substrate etching. However, on m-plane EG grain size increases by ~ 5x and on a-plane the grain size increases by ~2x as compared to EG on un-etched substrates. After hydrogen etching, the 2D peak FWHM reduces to ~ (35-50) cm^{-1} than EG grown on un-etched substrates with a 2D FWHM of ~ (60-70) cm^{-1} (Figure 4.3). The estimated carrier mobility from Raman 2D FWHM is also presented in Figure 4.3.EG grown on hydrogen etched substrates exhibit higher carrier mobility as compared to EG on un-etched substrates and for best EG layers the mobility is ~ 1500 cm^2/Vs, a potential advantage for future graphene based devices.

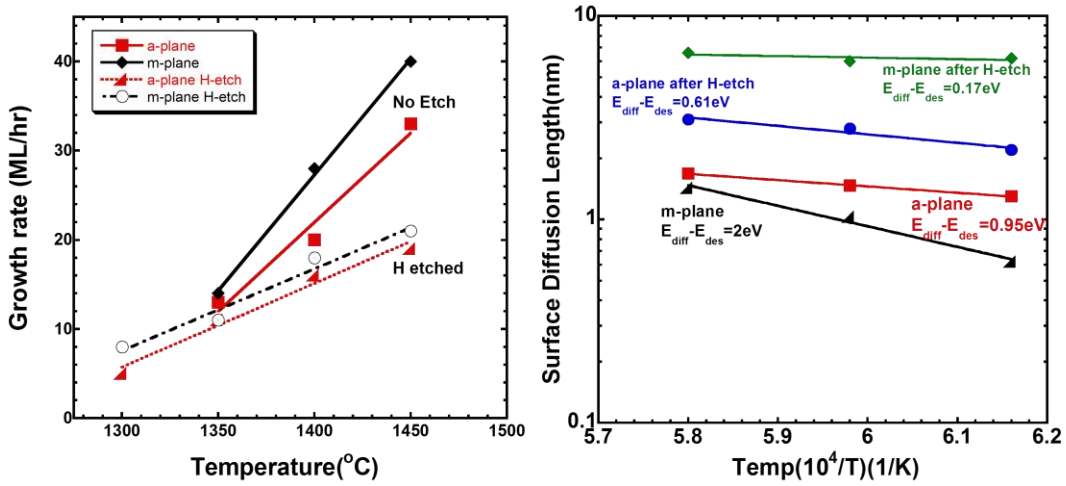

Figure 4.3: The EG growth rate variation with temperature on un-etched and hydrogen etched a and m plane substrates (left). Hydrogen etching prior to EG growth slows down the growth rate and initiates the EG growth at lower temperature. Arrhenius plot of the surface diffusion length as a function of temperature (right).

4.4. EG GROWTH KINECTICS DUE TO INITIAL SUBSTRATE PREPERATION:

Figure 4.3 (a) plots the EG growth rates before and after etching the substrates. Hydrogen etching provides with a slower growth rate and a plane EG samples. We adopted the modified BCF model for a detailed analysis on the Si adatom growth kinetics as established earlier in chapter 3 to analyze multilayer EG growth [c4:5].

According to this model, the grain boundaries/defects present in the grown graphene layer provide paths for the Si sublimation once they reach the defect sites facilitating multilayer EG growth after the formation of first layer. The activation energy required for the desorption of the Si adatom through these defects/grain boundaries is defined as E_{des} whereas the lateral diffusion of Si after the thermal decomposition of SiC substrates occurs in SiC/EG interface or EG/EG interface, and the activation energy required for lateral diffusion of the adatoms is defined as E_{diff} .

We observed that after hydrogen etching, the activation energies required for lateral surface diffusion of Si adatoms, E_{diff} and desorption through defect sites, E_{des} become more comparable as shown in figure 4.3 (b).Hydrogen etching reduces the surface roughness in the nucleation surface and thus enhances the lateral surface diffusion of the Si adatoms and reduces E_{diff}. The longer the Si adatom diffuses; it contributes to a high quality EG film with larger grains. Larger EG grains with better EG quality provide less defect sites for Si desorption, increasing the E_{des}. Therefore, the two contributing process for multilayer EG growth becomes more analogous reducing E_{diff}-E_{des} towards a weaker temperature dependence and a lower growth rate.

4.5. INFLUENCE OF DEFECT MINIMIZATION TOWARDS ELECTRONIC PROPERTIES:

To investigate the influence of initial surface preparation on EG electronic properties the Raman 2D FWHM is plotted as a function of the D/G ratio, the ratio of the integrated peak intensities of the D-peak to the G-peak (I_D/I_G), an indicator of the disorder/defects present in EG layers(Figure 4.4).EG samples with hydrogen etching prior EG growth exhibit a lower defect density comprising with narrower 2D FWHM, contributing towards higher carrier mobility as compared with EG on un-etched substrates.

The crystalline quality along with the defect density of the EG films were extracted from Raman spectroscopy. All EG samples on non-polar substrates exhibit a symmetric 2D peak fitted by a single Lorentzian. The 2D peak in EG Raman spectrum is an indicator of the stacking of the material[c4:6]. Ideal Bernal stacked graphite has a split asymmetric 2D peak, with each sub-peak corresponding to the AB stacking responsible for graphene's linear electron dispersion whereas a symmetric 2D peak indicates turbostratic stacking i.e. the stacking which is well oriented but rotationally disordered in nature[c4: 15]. Hence, the best films have grain sizes comparable to EG films formed on Si-face SiC and higher mobility, although the stacking of these films appears to be turbostratic rather than Bernal, promising for high mobility devices .We attribute this to proper hydrogen termination and formation of ordered SiC surfaces, although the lack of a clear template on the non-polar faces randomizes the stacking.

The disorder/defects present in EG layers are estimated by the D/G ratio, the ratio of the integrated peak intensities of the D-peak to the G-peak (I_D/I_G) in the EG Raman

spectrum. As shown in Figure 4.4, EG samples with hydrogen etching prior EG growth exhibit a lower D/G ratio, indicative of fewer defects than EG on un-etched substrates.

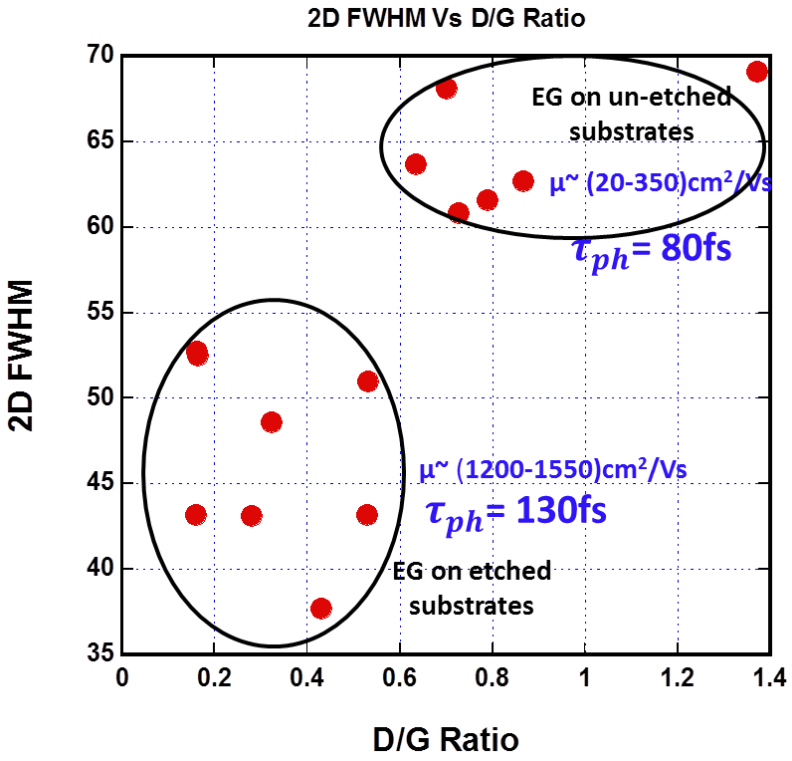

Figure 4.4: The 2D FWHM as a function of disorder (I_D/I_G) or (D/G) ratio obtained from Raman spectroscopy. After etching the Raman 2D FWHM along with the disorder ratio decreases providing a longer phonon lifetime.

After hydrogen etching, the 2D peak FWHM reduces to ~ (35-50) cm^{-1} than EG grown on un-etched substrates with a 2D FWHM of ~ (60-70) cm^{-1}. The estimated carrier mobility from Raman 2D FWHM is also presented in Figure 4.4.EG grown on hydrogen etched substrates exhibit higher carrier mobility as compared to EG on un-etched substrates.

The broadening of Raman 2D FWHM on etched substrates can be explained from the theory of spectral line shape, where Raman line width is expected to be inversely proportional to the lifetime of the signal .In case of crystal/semiconductors with

impurities and defects, Raman broadening can occur due to phonon lifetime shortening mechanisms[17] as a consequence of phonon scattering at impurity or defect centers. For our EG samples, we have calculated the phonon lifetime via Raman 2D line width. To eliminate the Raman 2D FWHM instrumental band pass broadening and acquire the actual phonon line width, the Raman spectra is acquired at successive slit widths ranging from 350um down to 100um described elsewhere [c4:16]. We plotted the measured Raman line width values Wm as a function of slit width, Ws and the zero-slit value line-width, Wp is extrapolated by the equation below:

$$W_m = \sqrt{W_p^2 + (W_s \times 9.2 \times 10^{-3})^2} \qquad (4.1)$$

Where instrumental band pass is $9.2\text{x}10^{-3}$ $cm^{-1}/\mu m$, obtained for our Raman system, as obtained previously [c4:16]. The zero slit value line width is then utilized to estimate the Raman phonon lifetime τ, from the energy-time uncertainty equation:

$$\frac{\Delta E}{\hbar} = \frac{1}{\tau} \qquad (4.2)$$

Where, ΔE is the Raman line width in cm^{-1} and $\hbar$ is $5.3\text{x}10^{-12}$ $cm^{-1}s$. Without etching, the phonon lifetime is 80 fs, whereas EG on etched substrates exhibit a longer phonon lifetime (~ 130 fs) as plotted in figure 4.45. As defects are reduced on the substrate by hydrogen etching, it leads to EG with less defect density (figure 4.4).Hence, in the presence of less scattering centers/defects, EG on etched substrates is expected to have less phonon scattering towards a longer phonon lifetime, contributing to a narrower 2D FWHM.

The EG carrier mobility on etched substrates increases by ~10x as compared to EG on un-etched substrates whereas the phonon lifetime increases by ~2x. The carrier

mobility is related to several scattering mechanisms including phonon scattering and impurity scattering; and the carrier lifetime can be expressed as:

$$\frac{1}{\tau} = \frac{1}{\tau_{ph}} + \frac{1}{\tau_I} + \cdots \quad (4.3)$$

Where τ_I is the impurity scattering lifetime. EG on etched substrates exhibit longer phonon lifetime as well as less impurity scattering due to lower defect density, which can be attributed to an increase of ~10x in the EG carrier mobility due to reduced scattering.

4.6. SUMMARY:

In summary, we investigated the role of substrate preparation on the EG growth kinetics on non-polar SiC substrates by hydrogen etching. Hydrogen etching prior to EG growth contributes larger EG grains with higher carrier mobility as compared to EG on unetched non-polar SiC substrates. After hydrogen etching, Si adatoms tend to show diffuse more on the EG surface with a higher surface diffusion length before desorption takes place. Since hydrogen etching provides a smoother starting surface with less defects, longer surface diffusion along with a lower defect density slow down the Si sublimation rate .Hence, the C atoms left on the surface get sufficient enough time to rearrange themselves towards larger EG grains with better EG quality. These EG layers also exhibit higher carrier mobility promising for electronic applications. Therefore, this study will open a path to better understanding the role of substrate preparation towards EG growth kinetics to achieve larger films with high mobility for future graphene based electronics.

CHAPTER 5

SELECTIVE MULTIMODAL GAS SENSING IN EPITAXIAL GRAPHENE

This chapter demonstrates the sensing behavior of epitaxial graphene (EG) grown on C-face SiC substrates by infrared reflectance spectroscopy through molecular adsorption of NO_2, NH_3 and N_2 gases. Fourier Transform Infrared Reflection (FTIR) measurements were performed on EG under gas exposure and it clearly exhibits an EG thickness dependence. By comparing the change in E_f under gas adsorption with the adsorbed impurity concentration as a function of EG thickness, the 3 gases were clearly distinguished, enabling a new paradigm for multi-modal gas sensing using optical interrogation of EG surfaces towards EG electronic or optical noses.

5.1. EPITAXIAL GRAPHENE AS A SENSING MEDIUM:

Graphene being a truly 2D material has an exceptionally high surface area, with the entire monolayer of sp^2 bonded carbon atoms .When introduced to chemical species; the whole volume can be exposed to surface adsorbents and hence graphene is highly sensitive to adsorbed molecules. The molecules form a weak Van der Waals force to the graphene surface and can act as donors/acceptors to the graphene sheet [Figure 5.1]. Furthermore, graphene is highly conductive as each carbon atom in the monolayer has three electrons which form σ-bonds with neighboring carbon atoms and the fourth bond is a π-bond, where electrons can freely travel. Thus any change in the carrier

concentration caused by the molecules adsorbed on the graphene surface will be readily sensed made graphene a promising candidate as highly sensitive sensors, even with the possibility of detecting individual molecules[c5:1]. The sensitivity of exfoliated graphene [c5:2] to NH_3 and NO_2 and that of epitaxial graphene (EG) have been established by molecular adsorption doping where the adsorbent NH_3 and NO_2 act as electron donating and withdrawing impurities, respectively[c5:3]. Epitaxial graphene on SiC substrate (EG) offers the added advantage of integrating sensors and readout circuits on the same chip[c5:4], that are also suitable for harsh environment operation, taking advantage of the wide band gap of SiC. This chapter focuses on the sensing behavior of epitaxial graphene on C-face with more defects as defects offer more dangling bonds, like those found on the edge plane of graphene, which can provide more sites for charge transfer to occur [c5:5], extending the remarkable surface sensitivity of graphene to bulk multilayer films.

We investigate the carrier transport by FTIR reflection spectroscopy and extract various transport parameters (i.e. thickness in monolayers (ML), E_F and adsorbed surface impurity concentrations (n_i)) within a theoretical framework and thus distinguish three different gases (N_2, NH_3 and NO_2). This study is significantly important for EG sensing behavior towards these gases.

5.2. EXPERIMENTAL SETUP FOR GAS SENSING:

For this study, EG was grown in an inductively heated home-built furnace on commercial n^+ 8^0 off axis 4H-SiC substrates on C-face, nitrogen doped ~$10^{19}/cm^3$.After each growth AFM (atomic force microscopy) and Raman Spectroscopy were performed

to investigate the EG surface morphology and crystalline quality. The ratio of intensities of the D-peak to G-peak, $I_D/I_G \leq 0.2$ demonstrates the high quality of our graphene [c5:6]. X-ray photoelectron spectroscopy (XPS) measurements were done to obtain the thickness [c5:7] in monolayer's (ML) on EG. The thickness extracted by XPS was consistent with our FTIR measurements [c5:8].

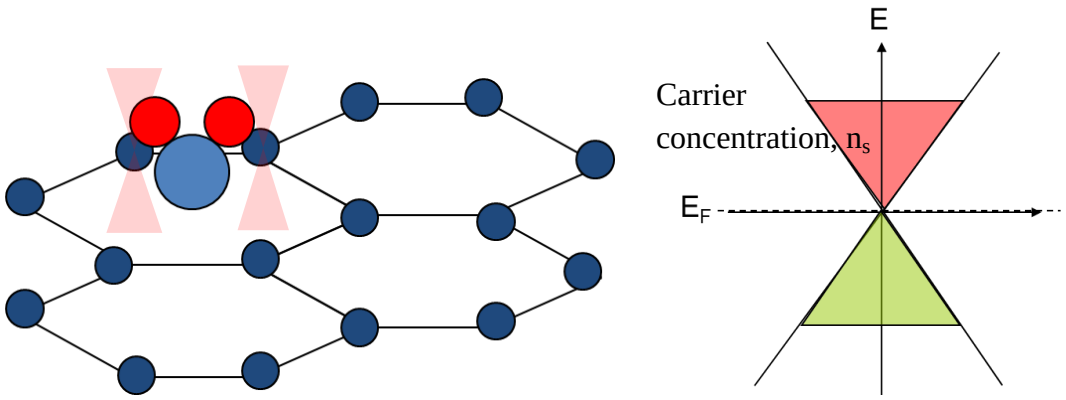

Figure 5.1: In graphene, entire volume is exposed to surface. As adsorbed molecules (left) act as donors/acceptors, carrier density changes as a result of charge transfer between incoming molecule and graphene layer (right).

FTIR measurements (2.5 µm to 25µm wavelength) were carried out with a blank SiC substrate, cut from the same wafer as the grown samples, as the reference and thus we obtained differential reflectance of EG with respect to SiC substrate. For gas exposure, the FTIR chamber was filled with the required adsorbent gas. Reference was taken with N_2 environment (known as inert gas) and corresponding IR reflection was taken in $N_2/NO_2/NH_3$ environment consequently. All reflectance measurement presented here are the differential reflectance with respect to the SiC substrate as described earlier [c5:9]. Figure 5.2 depicts the illustration of the experimental setup using FTIR.

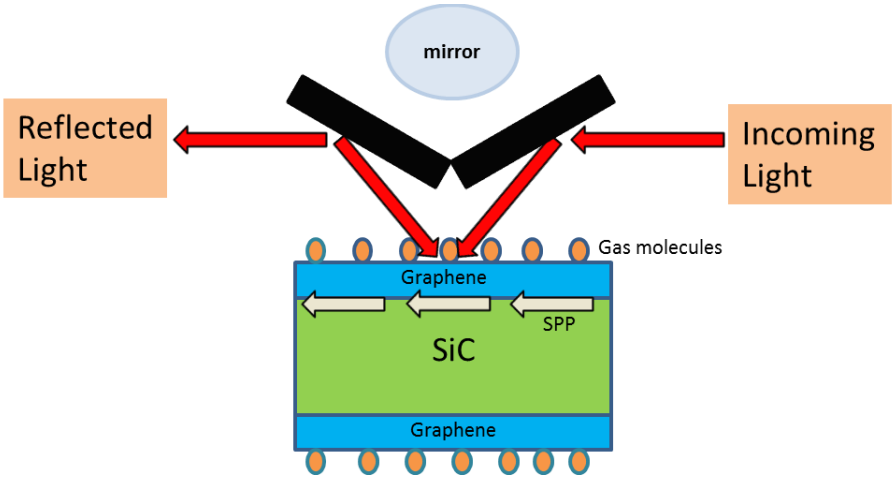

Figure 5.2: Experimental setup for gas sensing in EG by FTIR Spectroscopy.

5.3: EXPERIMENTAL RESULTS:

The experimental IR reflection spectra for 9, 22 and 34ML EG in N_2, NH_3 and NO_2 environment in Figure 5.2.We observed that reflectance (indicative of conductivity, with higher conductivity leading to higher reflectance) changes for different gases due to adsorption of surface impurities. From the experimental results, it is evident that for both in NO_2 and NH_3 environments reflectivity decreases compared to N_2 with NO_2 showing greater decrease than NH_3. This can be explained with the thought that NH_3 has lower adsorption energy leading to both charge interacting and non-interacting configuration [c5:10], whereas NO_2 has higher adsorption energy (0.3~0.4eV) [c5:11], which forces it to accept electrons in any adsorption configuration [c5:10]. Moreover, polar molecules [c5:3] change EG conductivity by a) inducing carriers in the EG and b) increasing scattering i.e. decreasing mobility. Scattering (τ) includes both intra and interband scattering, responsible for inter and intra band conductivity respectively [c5:3]. Thus, Increase or decrease of conductivity and hence reflectivity upon gas exposure is a tradeoff between carrier concentration and scattering.

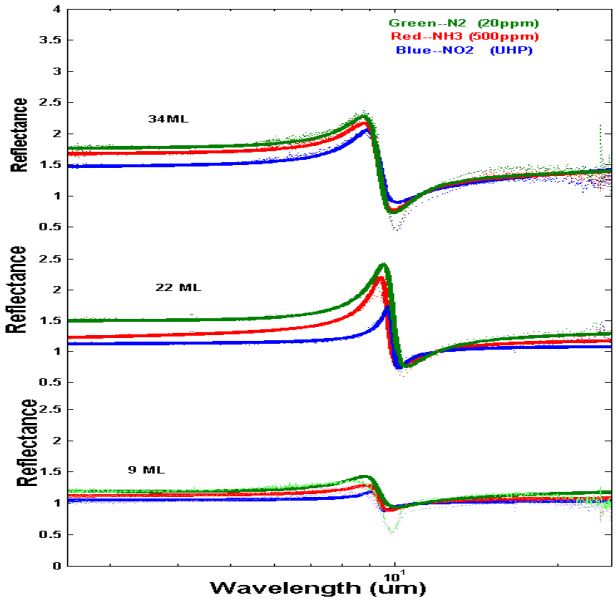

Figure 5.3: Shows the IR reflection measurement while experimental data fits with the mathematical model.

5.4. ANALYSIS APPROACH:

To investigate the experimental results, we adopted previously developed mathematical model [c5:12] to extract optical conductivity. The total reflection, R in case of FTIR spectra can be expressed as [c5:13]:

$$R = \frac{\left| \left(\sqrt{\varepsilon_1 \varepsilon_2(\omega) \varepsilon_0} / \alpha \right) + \frac{\sqrt{\varepsilon_1} N \sigma(\omega) \times \cos(\Phi 1)}{c} - \varepsilon_1 \varepsilon_0 \right|^2}{\left| \left(\sqrt{\varepsilon_1 \varepsilon_2(\omega) \varepsilon_0} / \alpha \right) + \frac{\sqrt{\varepsilon_1} N \sigma(\omega) \times \cos(\Phi 1)}{c} + \varepsilon_1 \varepsilon_0 \right|^2} \qquad (5.1)$$

Where $\boldsymbol{\varepsilon}_1$ and $\boldsymbol{\varepsilon}_2$ represents the dielectric function of air and SiC considering graphene at the interface between two dielectrics (as shown in figure 5.2),

$$\alpha = \frac{\sqrt{1-[(\frac{n_1}{n_2}\sin\Phi 1)]^2}}{\cos\Phi 1} \qquad (5.2)$$

With n_1 and n_2 are the refractive index of air and SiC respectively, σ(ω) is the total conductivity and ε_0 is the free space permittivity (~8.854×10^{-12} F/m). For EG on SiC substrates, ε_1 is the permittivity of air (~1) and ε_2 is the permittivity of SiC, which is a function of wavelength, given by [c5:14]

$$\varepsilon_2(\omega) = \varepsilon_\infty \frac{\omega^2 - \omega_{LO}^2 + i\Gamma_1\omega}{\omega^2 + \omega_{TO}^2 + i\Gamma_2\omega} \qquad (5.3)$$

Here ε_∞=6.5 is the positive ion core background dielectric constant, ω_{LO} is the longitudinal optical phonon frequency (ω_{LO}=972cm$^{-1)}$, ω_{TO} is the transverse optical phonon frequency

(ω_{TO}=796 cm^{-1}). $\Gamma_{1,2}$ describes the broadening of the phonon resonances, typically 5-60

cm^{-1}, where the higher values are due to free-carrier absorption. As we match the experimental values with this theoretical framework we extract conductivity.

The conductivity in any material can be divided into two components, intraband and interband conductivities. Intraband conductivity refers to the traditional Drude-Sommerfield type conductivity involving free electrons (holes) in the conduction (valence) band. Scattering events here only move carriers within the same band named intraband scattering. Interband conductivity accounts for processes where carriers can

move between bands, such as direct optical absorption and carrier recombination. Scattering events here lead to carriers changing bands known as interband scattering.

Introducing separate scattering times τ_{intra} and τ_{inter} for intraband and interband conduction modes respectively, these equations for the optical conductivity can be written as [c5:15];

$$\sigma_{intra} = \frac{e^2}{\pi\hbar}\frac{i}{\omega + i/\tau_{intra}}\int_{-\infty}^{+\infty} d\varepsilon\left(-\frac{\delta f(\varepsilon-\varepsilon_f)}{\delta\varepsilon}\right)\varepsilon^2\frac{\theta(\varepsilon^2)}{|\varepsilon|} \qquad (5.4)$$

$$\sigma_{inter} = i\frac{e^2(\omega + i/\tau_{inter})}{\pi}\int_{0}^{+\infty}\frac{d\varepsilon[f(\varepsilon-\varepsilon_f) - f(-\varepsilon-\varepsilon_f)]}{(2\varepsilon)^2 - \hbar^2(\omega + i/\tau_{inter})^2} \qquad (5.5)$$

where e is the electronic charge, ε is the energy variable over which integration takes place, ε_f is the Fermi level, ω is the frequency of the incident electromagnetic radiation, $f(\varepsilon) = [\exp(\varepsilon/kT)+1]^{-1}$ is the Fermi-Dirac distribution function, k is the boltzman constant $1.3806503 \times 10^{-23}$ m^2 kg $s^{-2}K^{-1}$ and θ is the Heaviside step function. We note that throughout this chapter, SI units are used, unless otherwise indicated. Hence, while matching the experimental results with the theory to estimate conductivity, we also extracted the fitting parameters i.e. Fermi level position, E_F , intraband scattering time τ_{intra} and interband scattering time τ_{inter}.

Finally, to extract to extract surface impurity concentration, n_i we match optical conductivity [c5:16] with conductivity in the Random Phase approximation (RPA):

$$\sigma_{T=0}^{RPA} = \frac{e^2}{\pi\hbar}\left[\frac{n_s}{n_i G[4r_s/(2-\pi r_s)]} + \frac{n_i F[4r_s/(2-\pi r_s)]}{4n_s}\right] \qquad (5.6)$$

where h is Planck's constant, n_s is the surface carrier concentration, r_s, G and F function is defined as below.

$$r_s = \frac{e^2}{4\pi\varepsilon_0\varepsilon_{SiC}v_F\hbar} \quad (5.7)$$

where e is the electron charge 1.6x10^{-19}C , v_F is the Fermi velocity 1.1x10^6 m/s, ε_{SiC} is the dielectric constant of SiC which has different values for high frequency (~6.5) and low frequency (~9.52) regime and G and F function defined [c5:16] as,

$$G(x) = \frac{x^2}{8}\int_0^{2\pi} \frac{\sin^2\theta}{(\sin\frac{\theta}{2}+x)^2}d\theta \text{ and } F(x) = \frac{x^2}{8}\int_0^{2\pi} \frac{(1-\cos\theta)^2}{(\sin\frac{\theta}{2}+x)^2}d\theta \quad (5.8)$$

Considering two limiting values of SiC dielectric constant (high frequency~6.5 and low frequency~9.52), two different values of r_s (high frequency~0.31 and low frequency~0.21) were calculated [c5:14]. For the high frequency r_s =0.31 was used for the conductivity

$$\sigma^{RPA}_{T=0}[highfrequency] = \frac{e^2}{\pi h}[\frac{n_s}{n_i G[4r_s/(2-\pi r_s)]}] \quad (5.9)$$

matching with the optical conductivity to extract impurity concentration, n_i. A similar procedure was used for the low frequency side where r_s ~0.21 arises from ε_{SiC} ~9.52 while considering

$$\sigma^{RPA}_{T=0}[lowfrequency] = \frac{e^2}{\pi h}[\frac{n_i F[4r_s/(2-\pi r_s)]}{4n_s}] \quad (5.10)$$

n_i extracted at both these frequency regimes was consistent. For further confirmation, we calculate intra and inter band scattering from n_i using equations

presented elsewhere [c5:16] and was found to be consistent with our extracted data within the experimental error limit.

5.5 VALIDATION OF EPITAXIAL GRAPHENE AS A GAS SENSOR:

The extracted scattering time, E_F and adsorbed surface impurity concentrations (n_i), are listed in Table 5.1 .For NH_3 and NO_2, the surface impurity concentration is higher than N_2 because of the nature of the gas interaction (electron donating and withdrawing ability) with the carriers on the EG surface. For further confirmation, we calculate intra and inter band scattering from n_i using equations presented elsewhere [c5:16] and was found to be consistent with our extracted data within the experimental error limit. Table 5.1 shows the extracted carrier transport parameters for 34, 22 and 9ML samples in gaseous medium while experiment matches with theory.

Table 5.1: Shows extracted parameter while experiment matches with theory.

No of Layer	**Gas**	**Fermi level (meV)**	**Impurity (cm^{-2})**	**Intra band scattering time (s)**	**Inter band scattering time(s)**
34	N_2	25 ± 2	$(2 \pm 0.5) \times 10^{11}$	$(2.8 \pm 0.9) \times 10^{-13}$	$(4.3 \pm 2.7) \times 10^{-14}$
	NH_3	30 ± 2	$(6 \pm 1) \times 10^{12}$	$(7.5 \pm 2) \times 10^{-15}$	$(2 \pm 1) \times 10^{-15}$
	NO_2	35 ± 2	$(2 \pm 0.6) \times 10^{13}$	$(1.4 \pm 1) \times 10^{-15}$	$(3.5 \pm 2) \times 10^{-16}$
22	N_2	45 ± 2	$(3 \pm 0.5) \times 10^{11}$	$(1.5 \pm 0.3) \times 10^{-14}$	$(2.3 \pm 0.1) \times 10^{-14}$
	NH_3	65 ± 2.5	$(7.5 \pm 1) \times 10^{12}$	$(6 \pm 3) \times 10^{-15}$	$(1 \pm 0.01) \times 10^{-15}$
	NO_2	95 ± 3	$(6 \pm 1) \times 10^{13}$	$(9 \pm 0.3) \times 10^{-16}$	$(2 \pm 0.7) \times 10^{-16}$
9	N_2	70 ± 4	$(5.1 \pm 0.5) \times 10^{11}$	$(1.5 \pm 0.1) \times 10^{-13}$	$(2.2 \pm 0.4) \times 10^{-14}$
	NH_3	90 ± 4	$(5.5 \pm 1) \times 10^{13}$	$(9 \pm 1) \times 10^{-16}$	$(3.6 \pm 1) \times 10^{-16}$
	NO_2	120 ± 4	$(1.5 \pm 0.8) \times 10^{14}$	$(4 \pm 1) \times 10^{-16}$	$(2 \pm 1) \times 10^{-16}$

With N_2 gas, 34ML samples shows Fermi level of ~25meV, close to neutral because our EG is thick. Similarly 22 and 9ML samples shows increase in Fermi level to 45meV and 70meV respectively because of thinner layer compared to 34ML, comparable to EG screening length ~1ML. As N_2 is an inert gas and should not contribute any impurity on the EG surface. Our extracted parameters indicate a surface impurity concentration due to N_2 gas is of $2\sim5x10^{11}cm^{-2}$, fairly consistent with an ex-situ sample that has not had any degassing or other processing performed on it.For NH_3 and NO_2, the surface impurity concentration is higher than N_2 because of the nature of the gas interaction (electron donating and withdrawing ability) with the carriers on the EG surface. Increase in Fermi level position compared to N2 in both the cases indicates more surface impurity concentration due to gas adsorption. For 34ML sample, change is Fermi level is very small (~5meV in NH_3 and 10meV in NO_2) indicates that thicker EG layer behaves more like neutral layer because of EG screening length is only ~1ML. For 22 and 9ML sample E_f changes are noticeably greater indicates the sensitivity of EG as presented by other researchers [c5:16]. This thickness dependent trend clearly supports the single molecule sensitivity of single layer graphene described elsewhere [c5:17]. E_f changes are greater in NO_2 compared to NH_3 attributes more charge transfer by NO_2 compared to NH_3. The impurity concentration is plotted against the extracted Fermi level position in figure 5.4. The change in Fermi level for a specific thickness also differs when exposed to two different gases which can be used to distinguish these gases with EG as a sensing medium by FTIR spectroscopy.

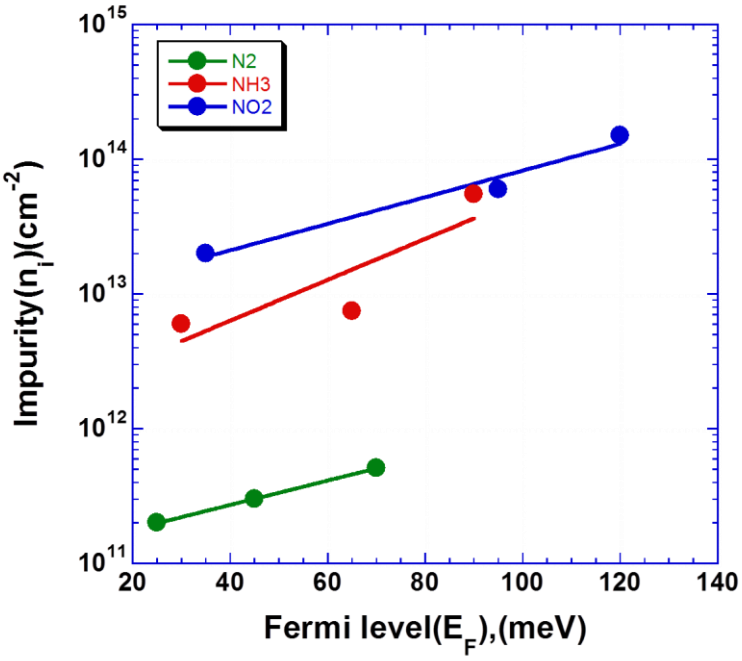

Figure 5.4: shows the impurity concentration variation with the Fermi level position for three different gases.

In summary, we explore the sensing properties of EG by FTIR spectroscopy. The Fermi level position changes differ based on the exposure of a specific gas (NO_2 and NH_3) suggests the application of EG sensors to distinguish these gases.

5.6 DEFECT INFLUENCED DIFFUSION MODEL:

The sensing behavior of EG on C-face SiC substrates can be explained in terms of molecular diffusion through defects present in the EG layers. From the geometric structure of epitaxial graphene on SiC substrate it is clearly evident that graphene lattice is too tight (as shown in chapter 3) to molecular diffusion beyond the EG surface. Hence, the defects/ grain boundaries provide pathways for molecular diffusion through the EG layers enabling a thickness dependent sensing in these layers. Therefore, we

have developed a defect influenced diffusion model assuming that the defects are evenly distributed and the molecular diffusion of the gases follows Fick's law of diffusion (Figure 5.5).

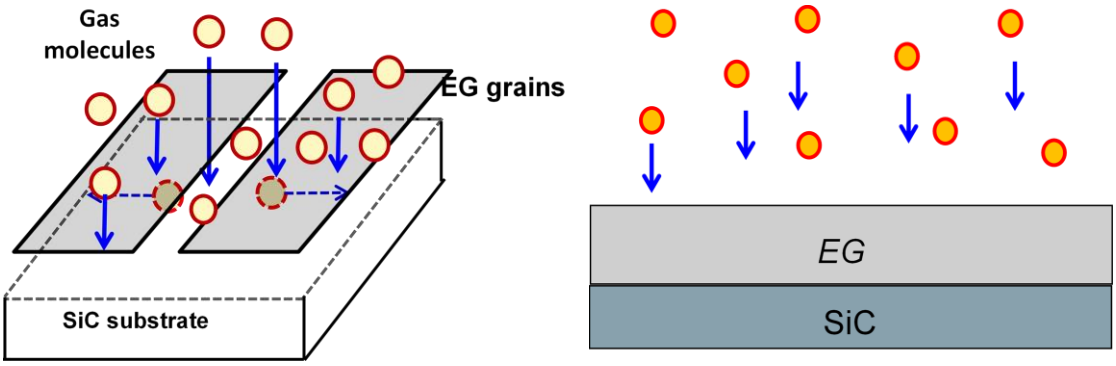

Figure 5.5: Molecular diffusion through the defects/grain boundaries in EG layers.

Upon gas exposure, the diffusion flux through the EG layers can be expressed as:

$$J = D\frac{\partial n}{\partial d} \qquad (5.11)$$

Where J is diffusion flux, D is the diffusion coefficient or diffusivity n is the impurity concentration and d is the thickness of the EG layers. According to Fick's second law of diffusion, the change in the impurity concentration with time (t) can be expressed as:

$$\frac{\partial n}{\partial t} = \frac{\partial J}{\partial d} = D\frac{\partial^2 n}{\partial d^2} \qquad (5.12)$$

Now, the boundary conditions are:

The impurity concentration, n (d, 0) =n_s and n (0, t) =0; Thus, by solving the equation with the boundary condition, the impurity concentration upon gas exposure through the EG layers:

$$n(d,t) = n_s\left(1 - 2\left(\frac{d}{2\sqrt{Dt\pi}}\right)\right) \qquad (5.13)$$

Where, n_s is the initial surface impurity concentration. Hence from this relationship, it is evident that as the no. of EG layer increases, the impurity concentration decreases, correlating our experimental observation to the theoretical defect influenced model.

Assuming, the initial surface impurity concentration is much smaller than the impurity concentration throughout the EG layers after gas exposure; the above equation can be written as:

$$n(d,t) \cong \frac{n_s d}{\sqrt{Dt\pi}} \quad (5.14)$$

The diffusion coefficient or diffusivity can also be extracted using this equation. Hence we plot the differential impurity concentration and extract the diffusion constant of NO_2 as shown in the figure below:

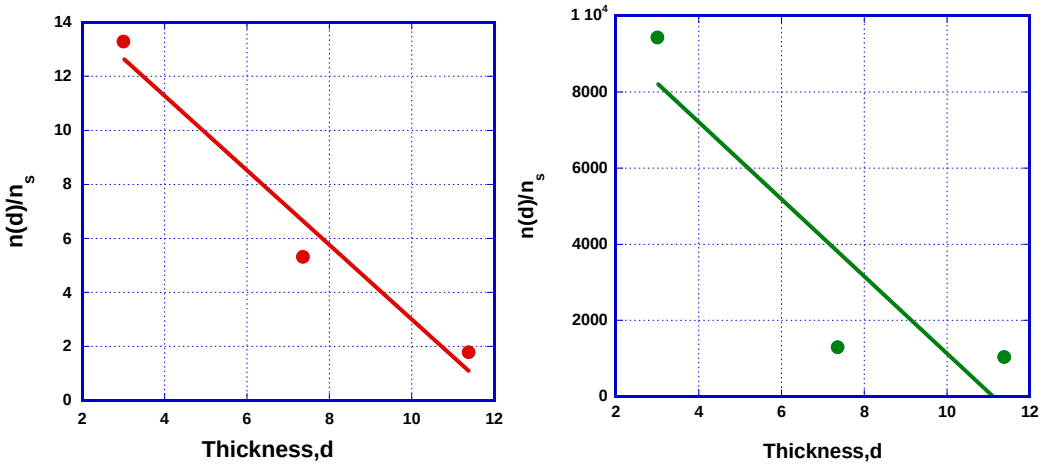

(a) (b)

Figure 5.6: n (d)/n_s as a function of EG thickness. (a)The diffusion coefficient of NO_2 in EG can be extracted from the slope of the curve. (b) The diffusion coefficient of NH_3 in EG is extracted from the slope of the curve.

As shown in the above figure, in case of NH_3 a higher impurity concentration (n (d)) is observed which can be due to concentration difference under gas exposure (500ppm NH_3 and 20 ppm NO_2).The diffusion constant for NO_2 calculated from the slope of this

curve is $3.36x10^{-5}$ cm^2/s; whereas the diffusion constant for NH_3 is $1.03x10^{-9}$ cm^2/s. The values are comparable to lithium diffusion through graphene planes in HOPG [c5:18]; diffusion coefficient ranges from $4.4x10^{-6}$ cm^2/s-$8.7x10^{-12}cm^2/s$. However, the diffusion of these gases in C-face EG is much faster than the vertical diffusion of lithium ions through the graphene planes ($8.7x10^{-12}cm^2/s$). This is due to the fact that EG on C face has grain boundaries; which provide larger area paths for diffusion under gas exposure as opposed to lithium diffusion in graphene planes in HOPG through point defects; as observed earlier for diffusion through porous graphene [c5:19,20]. Thus, EG on C face with grain boundaries can act as a gas filter to distinguish these gases based on the diffusion coefficient and serve as a promising candidate towards graphene based gas separation.

CHAPTER 6

DEFECT ENGINEERED THICK EPITAXIAL GRAPHENE

In this chapter, we present a method to produce much thicker layers >200 monolayers (ML) of multilayer graphene on Si-face 4H SiC substrates (0, 4 and 8 deg off cuts) than possible with solid-state decomposition at atmospheric pressure in Argon alone (~2ML). The process uses small concentrations (~0.1%) of SiF_4 diluted in Ar at 300 Torr and temperatures 1300-1600°C. This method exploits the thermodynamic advantages of SiF_4 to increase the Si-removal from the SiC surface, thereby increasing the graphene growth rate and reducing the minimum growth temperature to ~1400°C from ~1650°C in Ar alone. A method to estimate large thicknesses is described that relies on combined Raman/infrared spectroscopies. The films are turbostratically stacked, in stark contrast to the Bernal stacking observed for Si-face growth in Ar alone. The Raman D/G ratio, a measure of the defect density in the material, decreases from ~1 at 1400°C to <0.2 at 1600°C, enabling temperature controlled engineering of the defect profile of the material. This is critical for enabling defect-controlled applications in electrochemistry such as batteries and biosensors that require thick layers of activated graphitic carbon.

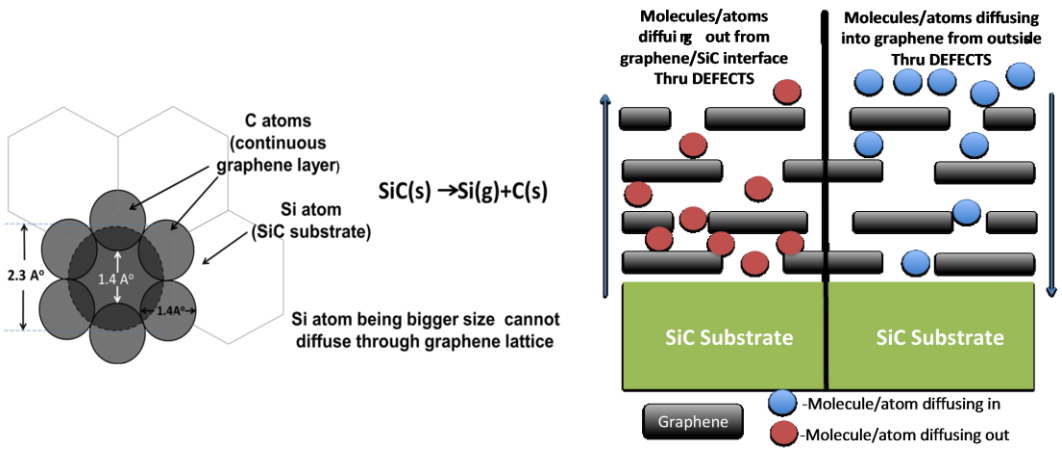

Figure 6.1: (Left) The silicon atom has a much larger diameter than the atomic gap in a graphene layer. Continuous, perfect epitaxial graphene (EG) layer formation prevents Si loss from the substrate. Si-loss can only occur through defects [c6:10].
(Right) Schematic of defects in graphene, and how they mediate molecular in-diffusion for doping and Si-adatom out-diffusion for growth of EG, as well as molecular doping/sensing using graphene [c6:8,11].

6.1. MOTIVATION:

Bulk graphite and graphitic/aromatic materials are ubiquitous in energy sciences and technology. Applications range from battery electrodes in alkali-metal intercalated graphite[c6:1], carbon supported precious metal catalyst systems[c6:2], polycyclic aromatic hydrocarbonsynthesis[c6:3], fuel cell electrodes[c6:4], water filtration[c6:5], ultra-capacitors[c6:6], gas filters/sensors[c6:7, 8] etc. These applications rely on the graphitic materials' high surface area, allowing large quantities of energy storage/conversion and other chemistry to be performed in a compact footprint. The high surface area arises from defects and non-idealities within the graphite (Figure 6.1) such as 0-dimensional (0D) point defects [c6:9], 1-dimensional (1D) grain boundaries and stacking mismatch boundaries [c6:10, 11], mixed graphitic allotropes (e.g., carbon nanotubes, fullerenes) [c6:12] .These defects enable the bulk of the graphite to be accessed from the surface. Without the defects, only the surface would be accessible, as

graphene, a monolayer of graphite has a very tight lattice that does not allow any diffusion through it (Figure 6.1) [c6:10, 11]. The influence of graphitic allotropes such as carbon nanotubes (CNT's) and fullerenes have been investigated in detail [c6:12]. The physical basis for understanding these defects is the graphene lattice [c6:13, 14], with appropriate boundary conditions or modifications to the lattice. Therefore, while traditional graphene growth has focused on producing 1-2 atomic monolayers (ML) for radio frequency (RF) applications, it is now desirable to produce defect-engineered graphene thick films >100ML to systematically engineer graphitic materials for energy applications.

The earliest ways to synthesize graphene, an emerging nanomaterial, were crude (e.g. exfoliation of bulk graphite), and could only produce single layers of small area <100um in size, although this led to the 2010 award of the Nobel Prize [c6:15] .Subsequently, several other techniques have been perfected. Graphene synthesis can be also be performed by reduction of graphite oxide, chemical vapor deposition on transition metal/metal carbide substrates [c6:16-18], and Si sublimation of SiC [c6:10, 19].The best quality material for nano-electronics has been obtained systematically through the solid-state decomposition of the surface of commercial SiC substrates [c6:20]. In this technique, the substrate is heated to high temperatures ~1300-1650°C, either in a vacuum [c6:21, 22], or in an inert environment such as Argon [c6:19, 23]. The Si vapor pressure at the surface, being higher than that of carbon, leads to the loss of Si from the surface, and the formation of a C-rich layer on the SiC surface according to reaction 1 (Table 6.1). The C-rich layer produced according to reaction (1) can then rearrange itself into a perfect graphene crystal, if enough time is available for the bonds to form. The thickness

is controlled by changing the temperature and time, as well as the choice of SiC substrate orientation [c6:1]. It was then shown that the best quality material could be obtained by slowing down the growth rate, [c6:24] allowing the C-rich layer to form complete C-C bonds leading to a good quality graphene crystal. If the formation rate of the C-rich layer is too fast, a good quality crystal cannot be formed due to random and uncorrelated nucleation of graphene layers [c6:25].

Table 6.1**.**Free formation energy (kcal/mol) for various reactions calculated using thermochemical data [c6:29].

	Reaction	**1800K**	**1900K**	**2000K**
	Dissociation and evaporation reactions			
1	$SiC(s) \rightarrow Si(g) + C(s)$	58.19	54.60	51.183
1a	$SiC(s) \rightarrow Si(l) + C(s)$	12.90	12.00	11.116
1b	$Si(l) \rightarrow Si\ (g)$	45.29	42.59	39.904
	SiF_4 reaction			
2	$Si\ (l) + SiF_4 \rightarrow 2SiF_2\ (g)$	19.69	15.93	12.22

We have further shown that the growth of multilayer films MUST be mediated by the defects in the growing epitaxial graphene film (Figure 6.1), [c6:10] as a perfect graphene crystal cannot allow further Si-atoms to diffuse through it and out of the growth region, a necessary step for the formation of a subsequent C-rich layer. In other words, to grow thick layers, defects must be present, and therefore, thicker layers contain a greater density of defects [c6:10]. Thus, we identified a fundamental trade-off in the production

of high-quality graphene growth i.e., that of crystal quality and crystal thickness. We demonstrate in this paper that by changing the Si loss mechanism from reaction (1) to reaction (2) (Table 6.1) that this trade-off may be broken. This technique relies on fluoride-enhanced Si-removal from the SiC surface, which also changes the stacking/defect profile of graphene grown on Si-face SiC.

6.2. EXPERIMENTAL DETAILS:

Nitrogen doped (~$10^{19}cm^{-3}$), chemo-mechanical polished (CMP), commercial 4H-SiC substrates with various off cuts (~0°, 4° and 8°) were used. Samples were cleaned by the standard RCA cleaning method. Graphene epitaxial growths were performed in a vertical hot-wall CVD reactor [c6:40]. New graphite parts are used and properly baked at 1600°C before loading the sample to remove any residual contamination in the reactor parts. Ultra high purity (99.9999%) Ar gas was used as the carrier gas. The substrate was first baked at 750°C in vacuum. Then, 10slm Ar carrier gas flow was initiated to attain the growth pressure (300 torr). The growth temperature (1300-1600°C) was reached in ~20 minutes, at which point 0.1% SiF_4 flow (Tetrafluorosilane or TFS) was initiated for the graphene growth. Finally, the temperature was ramped down from the growth temperature to 750°C in ~20 minutes. We show later that without the addition of SiF_4, no graphene growth is observed, consistent with the ~1650°C required for the onset of graphene growth in Ar [c6:23]. No pre-growth hydrogen etch was performed. The surface morphology of these films was characterized by atomic force microscopy (AFM) after each growth. Tapping mode was used to scan a 5um×5um window at several positions on a sample.

A micro-Raman setup with laser excitation wavelength at 632nm and a spot size of ~2μm was used to obtain the Raman spectra of the graphene samples. The Raman system was calibrated using the known Si peak at 520.7cm^{-1}. Reference blank substrate spectra were scaled appropriately and subtracted from the graphene spectra to show only the graphene peaks[c6:29].All the spectra shown in this paper are difference Raman spectra obtained in this manner, unless otherwise noted. The Raman spectrum of graphene has three peaks, called the G-peak, intrinsic to graphene/graphite at ~1580cm-1, the disorder induced D-peak at ~1350cm-1 and the second order 2D peak, which is present in ideal graphene[c6:29]. At 1300°C, no 2D peak was observed, showing no graphene growth [c6:41]. For all other conditions, we observed the presence of the aforementioned peaks, an indication of the presence of graphene. The width of the 2D-peak allows estimation of the carrier mobility of these films [c6:20], which is implemented for estimating film thicknesses >35ML.

After each growth, X-ray photoelectron spectroscopy (XPS) measurements were conducted using a Kratos AXIS Ultra DLD XPS system equipped with a monochromatic Al Kα source. The energy scale of the system was calibrated using an Au foil with Au4f scanned for the Al radiation and a Cu foil with Cu2p scanned for Mg radiation resulting in a difference of 1081.70 ± 0.025eV between these two peaks. The binding energy is calibrated using an Ag foil with Ag3d5/2 set at 368.21 ± 0.025eV for the monochromatic Al X-ray source. The monochromatic Al Kα source was operated at 15 keV and 150 W. The pass energy was fixed at 40 eV for the detailed scans. A charge neutralizer was used to compensate the surface charge. The graphene film thickness was extracted from the XPS spectrum as described in details elsewhere [c6:10].In short, for films <~10ML thick,

the C1s orbital peak for graphene was referenced to the C1s peak for the SiC substrate, whereas for films >10ML, the C1s peak was referenced to the Si2p peak for the SiC substrate.

FTIR reflectivity measurements were performed using a Galaxy Series FTIR-5000 spectrometer in an incidence angle of 40^{o} over the wavelength 2.5μm to 25μm using a blank SiC substrate as the reference.

6.3.RESULTS AND DISCUSSION:

The thichkess of graphene layers grown on sample substrates are listed in Table 6.2.

Table 6.2: Measured graphene thickness with the variation of temperature and substrate offcut.

Temperature(^{o}C)	On axis(MLs)	4 degree(MLs)	8 degree(MLs)
1300	No growth	No growth	No growth
1400	19/18(XPS)	25/28(XPS)	28/27(XPS)
1500	128	128	128
1600	39	220	139

For films <~35ML thick, the thickness was extracted using X-ray photoelectron spectroscopy (XPS) as described in the experimental section. However, for films >~35ML thick, which is much greater than the inelastic mean free path for the C1s and Si2p X-ray photoelectrons through graphene ~3nm, it is not possible to extract the thickness by XPS due to the disappearance of the reference substrate peaks.

Therefore, we adopt another approach to extract the thickness of the EG layers by Fourier Transform Infrared Spectroscopy (FTIR) [c6:26]. This relies on the fact that more conductive graphene layers are more reflective in the infrared [c6:21]. Thus, from a reflectance spectrum, the conductivity can be determined [c6:21]. For thick films, which are electrically neutral (far from the substrate>>1ML screening length in graphene [c6:27]), the carrier concentration, n, is known. Thus, if the carrier mobility, μ, can be estimated using Raman [c6:20], the total thickness in ML, N, can be estimated from the relationship below:

σ (FTIR)=Nnqμ (6.1)

At room temperature, n=2x8x$10^{10}$$cm^{-2}$/ML, assuming a neutral layer, where the factor of 2 comes from equal concentration of electrons and holes. The carrier mobility is estimated from the phenomenological μ-2D Raman width correlation [c6:20].Therefore, the lone fitting parameter is N, enabling reasonable confidence in the measurements. Furthermore, for layers <30ML, XPS can be used to correlate the results obtained from FTIR (Table 6.2), with excellent agreement.

We considered the FTIR reflectance at a low value of 500cm^{-1} to minimize apparent decrease in reflectance for non-specular reflections, damping from carrier scattering, and increase in conductivity from interband transitions at higher frequencies [c6:21]. Thus, we estimated the differential reflectance of graphene as we vary the number of layers with this approach as shown in Figure 6.2 for a μ=500cm^2/Vs.

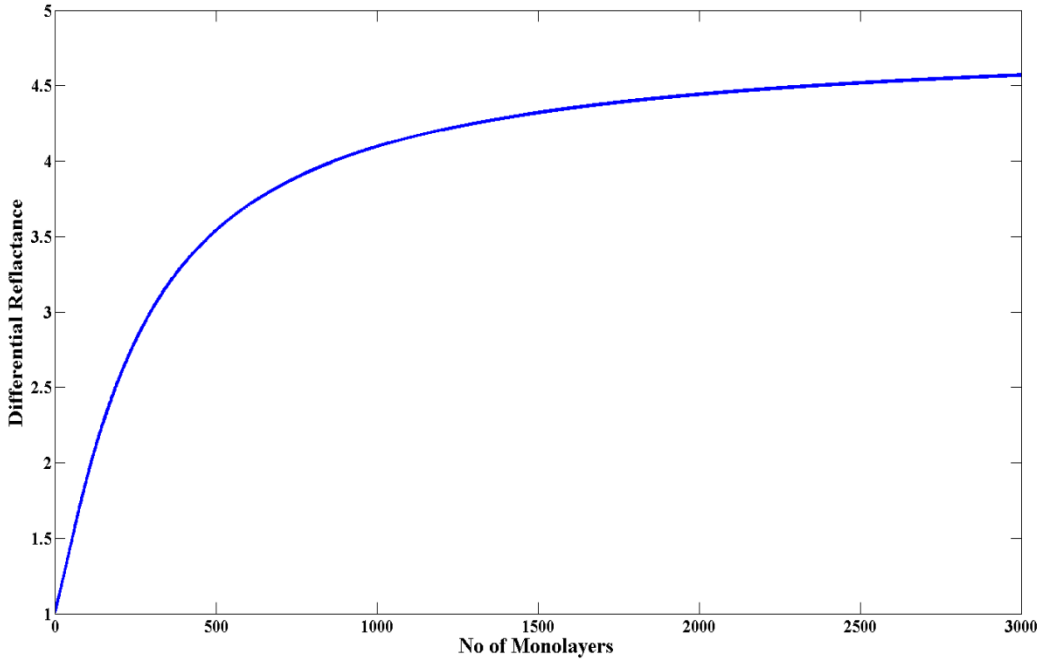

Figure 6.2. Variation of total differential infrared reflectance spectra with graphene thickness (i.e. number of graphene monolayers).

Finally the graphene film thickness was extracted while matching the experimental differential reflectance values with theory for 1400^{o}C, 1500^{o}C and 1600^{o}C (Table 6.2). We found good agreement for the EG thickness values grown at 1400^{o}C estimated from XPS and FTIR which also validates the model to extract EG thickness for values >30 MLs. The unusual temperature dependence of the thickness for on-axis substrates bears further investigation, and is beyond the scope of this dissertation. We speculate that this may be due to the lack of pre-growth hydrogen etching of the SiC surface, as per our standard process [c6:11].

The process of graphene/graphite epitaxial growth on SiC is described as follows. The partial pressure of Si is > 10 times higher than that of C in SiC at typical growth temperatures as described in experimental section[c6:24].As the partial pressure of Si in SiC is much higher than the other components of silicon carbide, when SiC is heated

above 1410°C in any inert gas environment (e.g. Ar. or He), SiC dissociates (reaction 1, Table-6.1), forms liquid (reaction 1a, Table-6.1) and eventually evaporates (reaction 1b, Table-6.1) leaving carbon layer(s) on the surface[c6:28]. The growth of epitaxial graphene on SiC in the SiF_4 -free process is dependent on the removal of Si from the surface by thermal evaporation. This is slowed further by diffusion through the growing graphene film, which allows diffusion only through defect sites [c6:10].

To accelerate graphene growth in a predictable manner with greater controllability of defect profile, a controllable Si removal process by some precursor gas is needed. SiF_4 has the strongest Si-F bond and thermal decomposition is difficult below 2000°C [c6:29, 30]. However, SiF_4 is known to forming SiF_2 (g) by reacting with solid Si at above 1150°C (Table 6.1, reaction 2)

[c6:31].

Since enhanced SiC etching with increased etch rate can be achieved by adding SiF_4 to H_2 where Si is removed by SiF_4 and C is removed by hydrogen [c6:29], this work is based on the fact that when instead of H_2, a noble gas Ar is used, SiF_4 selectively removes Si from the SiC surface without etching the carbon as H_2 does [c6:28], enabling faster growth of graphene. Si removal from the surface is more favorable (ΔG = 15.9 kcal/mol, reaction 2) by using SiF_4 compared to the thermal evaporation reaction (ΔG = 42.6 kcal/mol, reaction 1b). On the other hand, C removal by SiF_4 gas is considerably more difficult due to much higher free energy for the carbon removal reactions (ΔG > 100 kcal/mol)[c6:29]. Inert Ar itself does not remove Si from the surface since it does not react with Si or SiC. Hence, treatment of SiC at higher temperatures with SiF_4 in an inert environment is a silicon selective etching process using a precursor gas which can

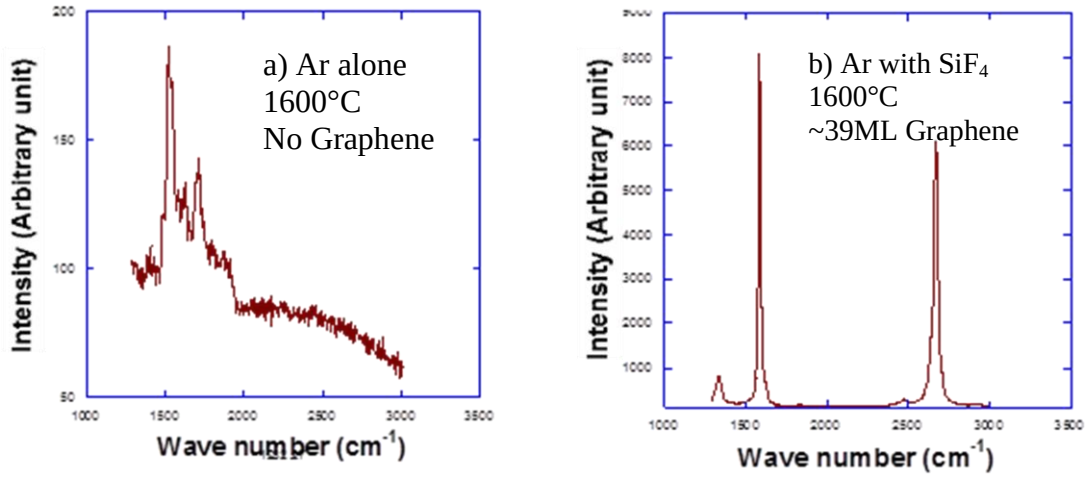

Figure 6.3. Comparison of as-taken Raman spectra (without substrate subtraction) of on-axis 4H-SiC substrates treated at 1600°C. (a) For 1 hour at 10 slm of Ar flow rates without SiF_4 and (b) for 1 hour at 10slm of Ar with a 10 sccm of SiF_4.

be exploited to grow thick graphene films.

The consequence of this reaction is demonstrated experimentally below in the Raman spectra of SiC samples treated (a) in Ar alone and (b) in Ar with SiF_4 (Figure 6.3).

Epitaxial graphene has three Raman peaks [c6:32]. These peaks are G-peak or graphene peak (~1580cm^{-1}), disorder or D-peak (1350cm^{-1}) and 2nd order of D peak or 2D-peak (~2660cm^{-1}). Surface pretreatment using Ar (1600°C, 1 hr) did not show any graphene G or 2D peak and no measurable difference was found from the original substrate, consistent with the 1650°C onset of epitaxial graphene growth on Si-face SiC [c6:23]. On the other hand, for the samples where 10 sccm of SiF_4 is added in the Ar gas stream during the growth process, a sharp G peak was found after the treatment(Figure 6.3b),and the SiC substrate signature is completely suppressed, demonstrating very thick growth compared to the standard Si-face epitaxial graphene on SiC [c6:33]. Using the FTIR-based thickness measurement technique described in the experimental section, the temperature and offcut dependence of the thickness were extracted for 1 hour growths, showing thickness increasing with temperature, even as the Raman-measured defect

density decreases (Figure 6.4), in contrast with the behavior seen with inert-ambient grown epitaxial graphene. This demonstrates the potential to break the thickness/material quality tradeoff observed with inert-ambient graphene [c6:34], enabling thick graphene structures for applications in energy, as well as for interconnects and electrodes in other electronic devices.

Another noteworthy observation is that while the growths in this study were kept to 1 hour (>> temperature ramps ~10mins up and ~10mins down) to minimize the influence of temperature ramp transients, calibration growths at 30mins and at 1600°C showed thickness less than that measured for the 1 hour growth (about half the thickness) under identical conditions. However, a detailed time-dependent study is required to determine whether SiF_4 mediated growth is thermodynamic/kinetic limited (~time) or limited by diffusion through the thick graphene (~√time) [c6:11]. Nevertheless, the results here indicate that the thickness on Si-face SiC could be increased (decreased) by increasing (decreasing) both temperature and time.

The 2D peak in EG Raman spectrum is an indicator of the stacking of the material. All graphene samples exhibit a symmetric 2D peak that could fit well with a single Lorentzian instead of the split-peak seen for Bernal stacked graphene/graphite [c6:35]. Ideal Bernal stacked graphite has a split asymmetric 2D peak, with each sub-peak corresponding to the AB stacking responsible for graphene's linear electron dispersion. This shows that these films are not AB Bernal-stacked as is the case usually with Si-face epitaxial graphene, but instead have turbostratic, or mixed stacking. Furthermore, the 2D/G ratio is ~0.5-1 (Figure 6.4a) for all these films (seen for 1-2ML graphene), indicating that on average, there are stacking clusters 1-2ML spread over the entire

thickness of the graphene.

The full width at half maximum (FWHM) for the 2D peak in these films is inversely correlated with the carrier mobility i.e., narrower FWHM correlates with higher mobility [c6:20]. In the films here, the FWHM decreases from ~60cm^{-1} at 1400°C to ~40cm^{-1} at 1600°C (Figure 6.4b). There appears to be a very weak offcut dependence, although on-

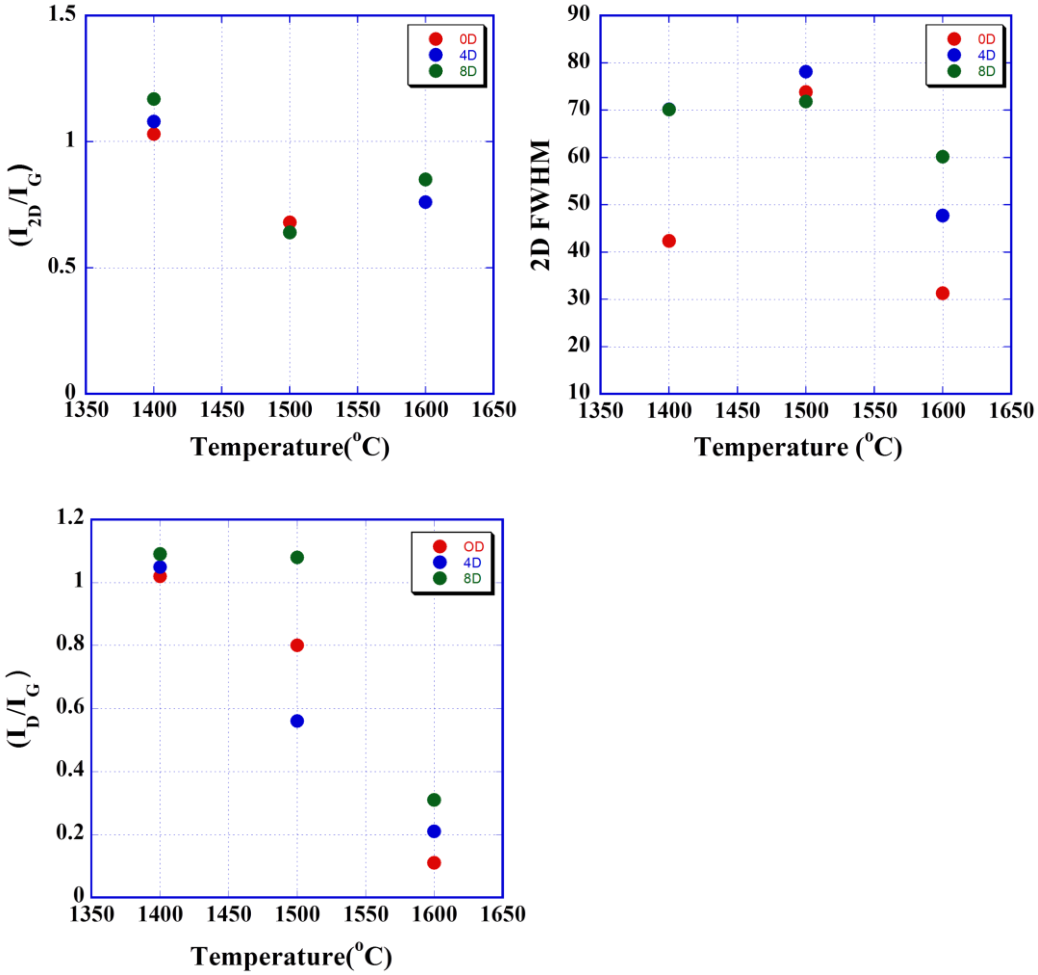

Figure 6.4. (a) Raman ratio of integrated peak intensities of the 2D peak to the G peak (I_{2D}/I_G) as a function of growth temperature attributed to graphene cluster of 1-2 ML spreading over the entire sample.(b) As temperature increases, the Raman 2D FWHM reduces towards higher carrier mobility for these samples. (c)Temperature dependence of Raman ratio of integrated peak intensities of the D peak to the G peak (I_D/I_G) indicative of defect density reduction in higher temperature growth.

axis substrates give the narrowest FWHM at 1600°C, as narrow as 30cm^{-1}, indicating a carrier mobility >1000cm^2/Vs, suitable for electronic applications in transistors [c6:22,36]. The lack of systematic offcut dependence may be due to the fact that there was no intentional hydrogen etching of the SiC surface performed prior to growth, as well as unintentional mis-orientations towards other directions (<1100>, rather than <1120>)[c6:37].

The improvement of electronic quality with increasing temperature correlates with a sharp decrease in defect density measured by Raman spectroscopy. The ratio of the areal intensity of the disorder D peak to that of the G-peak, proportional to the defect density [c6:38], decreases with temperature, from ~1 at 1400°C to <0.2 at 1600°C (Figure 6.4c), as higher temperatures facilitate the formation of graphitic sp^2 C=C bonds [c6:1]. There is again no clear offcut dependence, as for the 2D FWHM discussed above, showing that the temperature is the primary factor controlling defect density using SiF_4. The strong temperature dependence of this defect density demonstrates the possibility of temperature programmed defect engineering in graphene for energy applications, where defects are the dominant factor as discussed above.

The morphology of the sample surface is depicted in Figure 6.5 as measured by AFM. At 1300°C, samples with no graphene growth show wavy steps on the SiC substrate instead of straight steps, a fact we attribute to the high doping (~10^{19}cm^{-3}) of the substrate[c6:39]. There is step bunching observed, with step heights as large as 10nm (10 unit cells for 4H-SiC). As growth starts at 1400°C, steps can be observed on the surface, a morphology that appears to be inherited from the steps seen at 1300°C, as the domain size/defect density extracted from Raman above have no correlation with the step

dimensions.

The lack of a clear offcut dependence of the thickness suggests that step flow does not mediate this growth, although this point bears further investigation. At 1400^{o}C, graphene samples show an RMS surface roughness~15nm which reduces as the growth temperature increases (~5-8nm). These films are smooth enough for lithographic patterning using standard nanofabrication techniques to make devices.

6.4.SUMMARY:

In summary, temperature programmed defect engineering is demonstrated in epitaxial graphene grown on Si-face SiC using a novel SiF_4 accelerant for Si-removal, enabling

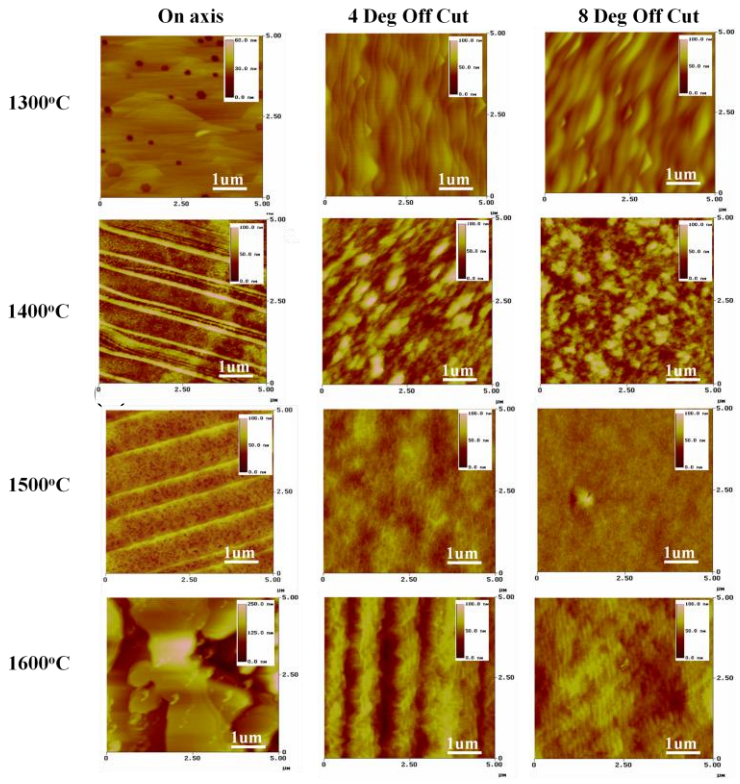

Figure 6.5.AFM images of the graphene grown on Si face 4H-SiC substrates (0, 4 and 8 degree offcuts) with SiF_4 accelerant at four different growth temperatures: 1300, 1400, 1500, and 1600^{o}C respectively. AFM image shows the surface morphology variation due to growth temperature and off cut.

films >100ML to be grown (RMS roughness <10nm), as opposed to <5ML without the accelerant. This graphene showed turbostratic stacking, as opposed to AB Bernal stacking normally observed, with a decrease in growth onset temperature from ~1650°C to ~1400°C. While there was not a systematic offcut dependence, the best quality films were obtained on on-axis SiC, with Raman D/G ratio <0.2, and estimated carrier mobility >1000cm^2/Vs, demonstrating the potential of this material for nanostructured defect engineered electrodes in energy applications.

CHAPTER 7

CONCLUSION

7.1. CONCLUSION:

This thesis focuses on the influence of defects present in the epitaxial graphene towards graphene growth and simple device performances. In general, defects present in any material are considered as detrimental for the quality and performances. However, in this thesis we established the role of defects in case of multilayer epitaxial graphene growth. Though, defects present in the first layer facilitates multilayer EG growth, the growth is limited by surface diffusion of Si adatoms to the defects/grain boundaries in case of EG on C-face and non-polar faces whereas for EG on Si face the growth is limited to (2-3 MLs) by desorption of Si adatoms through point defects. The impact of defects in the substrate is also discussed in the light of the growth kinetics model developed. Hydrogen etching is performed on the substrates prior to EG growth to reduce the defects in as cleaned samples. For Si face and C face, the optimized EG growth is observed in our case, although the crystalline quality and electronic properties improved in case of EG on non-polar faces. To investigate the sensing behavior in defective epitaxial graphene, EG on C-face is utilized and three different gases are clearly distinguished. Finally, the very well-known concept of defect engineering is introduced in epitaxial graphene layers by using SiF_4 gas, a novel method to achieve thick graphene layers on Si face SiC substrates, promising for energy storage applications.

7.2. FUTURE WORK:

In this work, we emphasize on the epitaxial graphene growth on SiC substrates in a home-built RF reactor furnace with an optimized process flow described in details in chapter 2.All growths were performed in the furnace where high vacuum was maintained ($<10^{-6}$ Torr) and the growth temperature varies from 1350^{o}C-1450^{o}C; although the best EG layers on Si face SiC substrates is observed for our optimized growth temperature at 1365^{o}C. The growth duration is typically 1 hr and then the system is cooled to 1000^{o}C and eventually to room temperature at a ramp rate of 7-8^{o}C/min to reduce thermal stress on the samples.

Epitaxial graphene grown on SiC substrates experience a compressive strain due to (i) lattice mismatch between graphene and SiC substrates underneath and (ii) the difference in thermal expansion coefficient between SiC (which contracts upon cooling) and graphene (which expands upon cooling). The compressive strain originated from the large difference in thermal expansion coefficients (TEC) can be expressed as [c7:1]:

$$\varepsilon = 1 - \frac{1}{exp\int_{RT}^{Tg} \Delta T \Delta\alpha(T)} \quad (7.1)$$

Where, ε is the compressive strain at room temperature (RT), T_g is the growth temperature,

Δα (T) is the difference between the SiC and graphene TECs and ΔT represents the cooling rate after the growth is done. The slower the cooling rate, ΔT would be smaller towards less compressive strain on the EG layers during the cool down

process. Thus, an even slower (i.e. 2-3^{o}C/min) cooling rate can be utilized in the growth process flow to minimize the compressive strain on the samples.

REFERENCES

CHAPTER 1

[c1-1]Geim, A. K. and Novoselov, K. S. Nature Materials 6 (3): 183–191 (2007)

[c1-2] T. Seyller, A. Bostwick, K. V. Emtsev, K. Horn, L. Ley, J. L. McChesney, T. Ohta, J. D. Riley, E. Rotenberg, F. Speck,Phys. Stat. Sol. B, Basic Solid State Phys. 2008, 245, 1436.

[c1-3]C. N. R. Rao, A. K. Sood, K. S. Subrahmanyam, Angew. Chem. Int. Ed. 2009, 48, 7752.

[c1-4]A. K. Geim, Science 2009, 324, 1530.

[c1-5]S. Park, R. S. Ruoff, Nat. Nanotechnol. 2009, 4, 217.

[c1-6]M. Pumera, Chem. Rec. 2009, 9, 211.

[c1-7]A. A. Balandin, S. Ghosh, W. Z. Bao, I. Calizo, D. Teweldebrhan, F. Miao, C. N. Lau, Nano Lett. 2008, 8, 902.

[c1-8] R. F. Service, Science 2009, 324, 875.

[c1-9]C. Lee, X. D. Wei, J. W. Kysar, J. Hone, Science 2008, 321,385.

[c1-10]J. Hass, W. A. de Heer, E. H. Conrad, J. Phys. Cond. Matter2008, 20, 27.

[c1-11]Jablan, Marinko, Hrvoje Buljan, and Marin Soljačić. "Plasmonics in graphene at infrared frequencies." Physical review B 80.24 (2009): 245435.

[c1-12]S. Blankenburg, M. Bieri, R. Fasel, K. Müllen, C.A. Pignedoli, D. Passerone, Small, 2010,6,2266.

[c1-13]F. Schedin, A. K. Geim, S. V. Morozov, E. W. Hill, P. Blake, M. I. Katsnelson, K. S. Novoselov, Nat Mater, 2007, 6, 652.

[c1-14]M. D. Stoller, S. J. Park, Y. W. Zhu, J. H. An, R. S. Ruoff, Nano Lett. 2008, 8, 3498.

[c1-15]E. Yoo, J. Kim, E. Hosono, H. Zhou, T. Kudo, I. Honma, Nano Lett. 2008, 8, 2277.

[c1-16]D. H. Wang, D. W. Choi, J. Li, Z. G. Yang, Z. M. Nie, R. Kou, D. H. Hu, C. M. Wang, L. V. Saraf, J. G. Zhang, I. A. Aksay, J. Liu, ACS Nano 2009, 3, 907.

[c1-17]B. Seger, P. V. Kamat, J. Phys. Chem. C 2009, 113, 7990.

[c1-18]R. Kou, Y. Y. Shao, D. H. Wang, M. H. Engelhard, J. H. Kwak, J. Wang, V. V. Viswanathan, C. M. Wang, Y. H. Lin,Y. Wang, I. A. Aksay, J. Liu, Electrochem. Commun. 2009,11, 954.

[c1-19]E. Yoo, T. Okata, T. Akita, M. Kohyama, J. Nakamura, I. Honma, Nano Lett. 2009, 9, 2255.

[c1-20]Y. C. Si, E. T. Samulski, Chem. Mater. 2008, 20, 6792.

[c1-21]Y. M. Li, L. H. Tang, J. H. Li, Electrochem. Commun. 2009,11, 846.

[c1-22]X. Wang, L. J. Zhi, N. Tsao, Z. Tomovic, J. L. Li, K. Mullen, Angew. Chem.-Int. Ed. 2008, 47, 2990.
[c1-23]J. B. Wu, H. A. Becerril, Z. N. Bao, Z. F. Liu, Y. S. Chen, P. Peumans, Appl. Phys. Lett. 2008, 92, 263302.
[c1-24]Z. Liu, J. T. Robinson, X. M. Sun, H. J. Dai, J. Am. Chem. Soc. 2008, 130, 10876.
[c1-25]H. Chen, M. B. Muller, K. J. Gilmore, G. G. Wallace, D. Li,Adv. Mater. 2008, 20, 3557.
[c1-26]C. S. Shan, H. F. Yang, J. F. Song, D. X. Han, A. Ivaska, L. Niu, Anal. Chem. 2009, 81, 2378.
[c1-27]Z. J. Wang, X. Z. Zhou, J. Zhang, F. Boey, H. Zhang, J.Phys. Chem. C 2009, 113, 14071.
[c1-28]C. H. Lu, H. H. Yang, C. L. Zhu, X. Chen, G. N. Chen, Angew. Chem. Int. Ed.t. 2009, 48, 4785.
[c1-29]Y. Wang, J. Lu, L. H. Tang, H. X. Chang, J. H. Li, Anal.Chem. 2009, 81, 9710.
[c1-30]Humberto Terrones et al. , "The role of defects and doping in 2D graphene sheets and 1D nanoribbons", Rep. Prog. Phys. 2012 75 062501
[c1-31]Wallace, P. R. (1947). "The Band Theory of Graphite". Physical Review 71: 622 (1947)
[c1-32]Charlier, J.-C.; Eklund, P.C.; Zhu, J. and Ferrari, A.C. "Electron and Phonon Properties of Graphene: Their Relationship with Carbon Nanotubes". from Carbon Nanotubes: Advanced Topics in the Synthesis, Structure, Properties and Applications, Ed. A. Jorio, G. Dresselhaus, and M.S. Dresselhaus.
[c1-33]Semenoff, G. W. (1984). "Condensed-Matter Simulation of a Three-Dimensional Anomaly". Physical Review Letters 53: 5449. (1984)
[c1-34]Avouris, P., Chen, Z., and Perebeinos, V. (2007). "Carbon-based electronics". Nature Nanotechnology 2 (10): 605. (2007)
[c1-35]Dresselhaus M S and Dresselhaus G 1981 Adv. Phys. 30 139.
[c1-36]Shamaita S Shetu, S. Omar, K. Daniels, B. Daas, J Andrewes , S. Ma, T. S. Sudarshan, MVS Chandrashekhar, "Si-adatom kinetics in defect mediated growth of multilayer epitaxial graphene films on 6H-SiC" , Journal of Applied Physics,2013,Vol.114,Issue 16.
[c1-37]B. Daas, O. Sabih, S. Shetu, K. Daniels, S. Ma, T. Sudarshan, MVS Chandrashekhar , "Comparison of epitaxial graphene growth on polar and non-polar 6H-SiC faces: On the growth of multilayer films", (Journal of Crystal Growth and Design,20 12, Vol. 7, 3379-3387.
[c1-38]G. M. Rutter, J. N. Crain, N. P. Guisinger, T. Li, P. N. First, J. A. Stroscio, Science, 2007, 317, 219.
[c1-39]Rafiee, Mohammed A., Javad Rafiee, Iti Srivastava, Zhou Wang, Huaihe Song, Zhong-Zhen Yu, and Nikhil Koratkar. "Fracture and fatigue in graphene nanocomposites." small 6, no. 2 (2010): 179-183.

CHAPTER 2

[c2-1]M. Y. Han, B. Özyilmaz, Y. Zhang and P. Kim, Phys. Rev. Lett. **98** (20), 206805 (2007).
[c2-2]C. Berger, Z. Song, T. Li, X. Li, A. Y. Ogbazghi, R. Feng, Z. Dai, A. N. Marchenkov, E. H. Conrad, P. N. First and W. A. de Heer, J Phys. Chem. B **108** (52), 19912-19916 (2004).
[c2-3]Y. Zhang, Tan, J. W., Stormer, H. L. & Kim, P, Nature **438** (7065), 201-204 (2005).
[c2-4]K. I. Bolotin, K. J. Sikes, Z. Jiang, M. Klima, G. Fudenberg, J. Hone, P. Kim and H. L. Stormer, Solid State Comm. **146** (9–10), 351-355 (2008).
[c2-5]C. Lee, X. Wei, J. W. Kysar and J. Hone, Science **321** (5887), 385-388 (2008).
[c2-6]J. S. Bunch, A. M. Van Der Zande, S. S. Verbridge, I. W. Frank, D. M. Tanenbaum, J. M. Parpia, H. G. Craighead and P. L. McEuen, Science **315** (5811), 490-493 (2007).
[c2-7]http://www.electronicspecifier.com/Tech-News/IDTechEx-forecasts-100-million-graphene-market-2018.asp.
[c2-8] Geim, A. K. and Novoselov, K. S. "The rise of graphene". Nature Materials 6 (3): 183–191 (2007).
[c2-9]A. J. Pollard, R. R. Nair, S. N. Sabki, C. R. Staddon, L. M. A. Perdigao, C. H. Hsu, J. M. Garfitt, S. Gangopadhyay, H. F. Gleeson, A. K. Geim and P. H. Beton "Formation of Monolayer Graphene by Annealing Sacrificial Nickel Thin Films" *J. Phys. Chem. C*, 2009, *113* (38), pp 16565–16567.
[c2-10]Yu, Q. et al., Graphene segregated on Ni surfaces and transferred to insulators. Appl. Phys. Lett. 93, 113103 (2008).
[c2-11]Reina, A. et al., Large area, few-layer graphene films on arbitrary substrates by chemical vapor deposition. Nano Letters 9, 30-35 (2009).
[c2-12]Xuesong Li. et al., Evolution of Graphene Growth on Ni and Cu by Carbon Isotope Labeling, *Nano Lett.*, **2009**, *9* (12), pp 4268–4272.
[c2-13]Yu Q, Lian J, Siriponglert S, Li H, Chen Y P and Pei S-S 2008Appl. Phys. Lett. 93 113103.
[c2-14]Kondo D, Sato S, Yagi K, Harada N, Sato M, Nihei M andYokoyama N 2010 Appl. Phys. Express 3 025102.
[c2-15]Jahan M. Dawlaty, Shiriram Shivaraman, Jared Strait, Paul George, Mvs Chandrashekhar, Farhan Rana, Michael G. Spencer, Dmity veksler and Yunqing Chen, Appl. Phys. Lett. 93,131905 (2008)
[c2-16]M. Hupalo,E. Conrad,and M. C. Tringides "Growth mechanism for epitaxial graphene on vicinal 6H-SiC(0001) surfaces: A scanning tunneling microscopy study" Phys. Rev. B 80, 041401(R) (2009).
[c2-17]B.K.Daas, Sabih U Omar, S.Shetu, Kevin M.Daniels, S.Ma, T.S.Sudarshan, MVS Chandrashekhar " Comparison of epitaxial graphene growth on polar and non-polar 6H-SiC faces:On the growth of multilayer films". Cryst. Growth Des., **2012**, 12 (7), pp 3379–3387.
[c2-18]J. L. Tedesco, G. G. Jernigan, J. C. Culbertson, J. K. Hite, Y. Yang, K. M. Daniels, R. L. Myers-Ward, C. R. Eddy, J. A. Robinson, K. A. Trumbull, M. T. Wetherington, P. M. Campbell, and D. K. Gaskill "Morphology and

Characterization of argon mediated epitaxial graphene on C face SiC", Appl. Phys. Lett. 96, 222103 (2010).
[c2-19]J. L. Tedesco, G. G. Jernigan, J. C. Culbertson, J. K. Hite, Y. Yang, K. M. Daniels, R. L. Myers-Ward, C. R. Eddy, J. A. Robinson, K. A. Trumbull, M. T. Wetherington, P. M. Campbell, and D. K. Gaskill, Appl. Phys. Lett. (2010) 96, 222103.
[c2-20]J Hass, W A de Heer and E H Conrad, J. Phys.: Condens. Matter 20 (2008) 323202
[c2-21]Konstantin V. Emtsev, Aaron Bostwick, Karsten Horn, Johannes Jobst, Gary L. Kellogg, Lothar Ley, Jessica L. McChesney, Taisuke Ohta, Sergey A. Reshanov, Jonas Röhrl, Eli Rotenberg, Andreas K. Schmidt, Daniel Waldmann, Heiko B. Weber & Thomas Seyller, Nature Mat. (2009) 8, 203.
[c2-22]Walt A. de Heer, Claire Berger,, Ming Ruan, Mike Sprinkle, Xuebin Li, Yike Hu, Baiqian Zhang**,** John Hankinson, and Edward Conrad., PNAS (2011) 108, 16900.
[c2-23]C. Berger, Z. Song, X. Li, X. Wu, N. Brown, C. Naud, D. Mayou, T. Li, J. Hass, A. N. Marchenkov, E. H. Conrad, P. N. First, and W. A. de Heer;" Ultrathin Epitaxial Graphite: 2D Electron Gas Properties and a Route toward Graphene-based Nanoelectronics" J. Phys. Chem. B 108, 19912 (2004).
[c2-24]J. Drowart, G. De Maria, and M. G. Inghram, J. Chem. Phys. (1958) 29, 1015
[c2-25]B.K. Daas, K. M. Daniels, T.S. Sudarshan, M.V.S. Chandrashekhar. Journal of Appl. Phys. (2011) Vol 110, issue 11, 113114.
[c2-26]Li Jin, Qiang Fu, Hui Zhang, Rentao Mu, Yanhong Zhang, Dali Tan, and Xinhe Bao, J. Phys. Chem. C (2012), 116 (4), pp 2988–2993
[c2-27]E.N. Mokhov, M.G. Ramm, A.D. Roenkov, Yu.A. Vodakov, Mat. Sci. and Eng. B 46 (1997) 317-323.
[c2-28]Yu. M. Tairov, Mat. Sci. and Eng. B 29 (1995) 83-89.
[c2-29]K. V. Emtsev, F. Speck, T. Seyller, L. Ley and J. D. Riley, Physical Review B **77** (15), 155303 (2008).
[c2-30]E. Rollings, G. H. Gweon, S. Y. Zhou, B. S. Mun, J. L. McChesney, B. S. Hussain, A. V. Fedorov, P. N. First, W. A. de Heer and A. Lanzara, Journal of Physics and Chemistry of Solids **67** (9–10), 2172-2177 (2006).
[c2-31]S. Shivaraman, M. Chandrashekhar, J. J. Boeckl and M. G. Spencer, J. Elec. Mat. **38** (6), 725-730 (2009).
[c2-32]P. J. Cumpson, Surf. Inter. Anal. **29** (6), 403-406 (2000).
[c2-33]M. Hupalo,E. Conrad,and M. C. Tringides "Growth mechanism for epitaxial graphene on vicinal 6*H*-SiC(0001) surfaces: A scanning tunneling microscopy study" Phys. Rev. B 80, 041401(R) (2009).
[c2-34]Virgil B. Shields, MVS Chandrashekhar, Shriram Shivaraman, Michael G. Spencer, journal of electron matter2009
[c2-35]A. Luce, 2007.
[c2-36]A.C Ferrari and J. Robertson "Interpretation of Raman spectra of disordered and amorphous carbon" Phys. Rev B 61 vol 61 num 20 (2000).
[c2-37]Shriram Shivaraman, M.V.S. Chandrashekhar, Jhon J. Boeckl and Michael Spencer;" Thickness Estimation of Epitaxial Graphene on SiC Using

Attenuation of Substrate Raman Intensity" J. of Elec. Matt., 38,6 (2009).
[c2-38]L. G. Cançado, K. Takai, T. Enoki, M. Endo, Y. A. Kim, H. Mizusaki, A. Jorio, L. N. Coelho, R. Magalhães-Paniago, and M. A. Pimenta, Appl. Phys. Lett. (2006) 88, 163106
[c2-39]L. G. Cancado, A. Jorio, E. H. Martins Ferreira, F. Stavale, C. A. Achete, R. B. Capaz, M. V. O. Moutinho, A. Lombardo, T. S. Kulmala, and A. C. Ferrari Nano Lett. (2011) *11* (8), pp 3190–3196.
[c2-40]Mauricio Terrones Andrés R. Botello-Méndez, Jessica Campos-Delgado, Florentino López-Urías, Yadira I. Vega-Cantú, Fernando J. Rodríguez-Macías, Ana Laura Elías, Emilio Muñoz-Sandoval, Abraham G. Cano-Márquez, Jean-Christophe Charlier, Humberto Terrones; Nanotoday (2010) Vol. 5, Issue 4, pp. 351–372
[c2-41]Joshua A. Robinson, Kathleen A. Trumbull, Michael LaBella, , Randall Cavalero,Matthew J. Hollander, Michael Zhu, Maxwell T. Wetherington, Mark Fanton, and David W. Snyder, Appl. Phys. Lett. (2011) 98, 222109.
[c2-42]Daniels, K.M., et al., Evidences of electrochemical graphene functionalization and substrate
[c2-43]dependence by Raman and scanning tunneling spectroscopies. Journal of Applied Physics, 2012. 111(11).
[c2-44] Daas, B.K., et al., Polariton enhanced infrared reflection of epitaxial graphene. Journal of Applied Physics, 2011. 110(11)
[c2-45]Sun, D., et al., Spectroscopic Measurement of Interlayer Screening in Multilayer Epitaxial Graphene. Physical Review Letters, 2010. 104(13): p. 136802.
[c2-46]Robinson, J.A., et al., Correlating Raman Spectral Signatures with Carrier Mobility in Epitaxial Graphene: A Guide to Achieving High Mobility on the Wafer Scale. Nano Letters, 2009. 9(8): p. 2873-2876.

CHAPTER 3

[c3-1]Luxmi, N. Srivastava, Guowei He, and R. M. Feenstra "Comparison of graphene formation on C-face and Si-face SiC {0001} surfaces" Phys. Rev. B 82, 235406 (2010).
[c3-2]Jennifer K. Hite, Mark E. Twigg, Joseph L. Tedesco, Adam L. Friedman, Rachael L. Myers-Ward, Charles R. Eddy, Jr., and D. Kurt Gaskill "Epitaxial Graphene Nucleation on C-Face Silicon Carbide".. Nano Lett.11 (3), pp 1190–1194 (2011)
[c3-3]J. L. Tedesco, G. G. Jernigan, J. C. Culbertson, J. K. Hite, Y. Yang, K. M. Daniels, R. L. Myers-Ward, J. C. R. Eddy, J. A. Robinson, K. A. Trumbull, M. T. Wetherington, P. M. Campbell and D. K. Gaskill, Applied Physics Letters **96** (22), 222103-222103 (2010).

[c3-4]B.K.Daas, Sabih U Omar, S.Shetu,Kevin M.Daniels, S.Ma, T.S.Sudarshan, MVS Chandrashekhar " Comparison of epitaxial graphene growth on polar and non-polar 6H-SiC faces:On the growth of multilayer films". Cryst. Growth Des., 2012, 12 (7), pp 3379–3387

[c3-5]G. M. Rutter, J. N. Crain, N. P. Guisinger, T. Li, P. N. First and J. A. Stroscio, Science **317** (5835), 219-222 (2007).
[c3-6]N. Srivastava, G. He, R. M. Feenstra and P. Fisher, Phys. Rev. B 82 (23), 235406 (2010).
[c3-7]G. Prakash, M. A. Capano, M. L. Bolen, D. Zemlyanov and R. G. Reifenberger, Carbon **48** (9), 2383-2393 (2010).
[c3-8]J. A. Kellar, J. M. P. Alaboson, Q. H. Wang and M. C. Hersam, Appl. Phys. Lett. **96** (14), 143103-143103 (2010).
[c3-9]S. G. Davis, D. F. Anthrop and A. W. Searcy, J Chem. Phys. 34 (2), 659-664 (1961).
[c3-10]B. Jungblut and E. Hoinkis, Phys. Rev. B 40 (16), 10810-10815 (1989).
[c3-11]C. Berger, Z. Song, T. Li, X. Li, A. Y. Ogbazghi, R. Feng, Z. Dai, A. N. Marchenkov, E. H. Conrad, P. N. First and W. A. de Heer, J Phys. Chem. B 108 (52), 19912-19916 (2004).
[c3-12]N. Ferralis, R. Maboudian and C. Carraro, Phys. Rev. Lett. 101 (15), 156801 (2008).
[c3-13]G. D. Ado Jorio, M. S. Dresselhaus, Carbon Nanotubes: Advanced Topics in the Synthesis, Structure, Properties and Applications (Springer, 2007).
[c3-14]F. C. J.O.Hirschfelder, and R.B. Bird, Molecular Theory of Gases and Liquids. (John Wiley and Sons, Inc, New york, 1954).
[c3-15]J. Drowart, G. De Maria and M. G. Inghram, J Chem. Phys. 29 (5), 1015-1021 (1958).
[c3-16]A. Luce, 2007.
[c3-17]L. G. Cancado, K. Takai, T. Enoki, M. Endo, Y. A. Kim, H. Mizusaki, A. Jorio, L. N. Coelho, R. Magalhaes-Paniago and M. A. Pimenta, Appl. Phys. Lett. **88** (16), 163106-163103 (2006).

[c3-18]W. K. Burton, N. Cabrera and F. C. Frank, Philos. Trans. R.l Soc. A 243 (866), 299-358 (1951).
[c3-19]R. L. Schwoebel and E. J. Shipsey, J. App. Phys. 37 (10), 3682-3686 (1966).
[c3-20]K. Voigtlaender, H. Risken and E. Kasper, Appl. Phys. A 39 (1), 31-36 (1986).
[c3-21]H. C. Abbink, R. M. Broudy and G. P. McCarthy, J. App. Phys. 39 (10), 4673-4681 (1968).
[c3-22]E. Kasper, Appl. Phys. A 28 (2), 129-135 (1982).
[c3-23]T. S. a. T. Nishinaga, Jpn. J Appl. Phys. 28 (Part 1, No. 7), 1212-1216 (1989).
[c3-24]J. Hass, W. A. d. Heer and E. H. Conrad, J Phys. Cond. Matt **20** (32), 323202 (2008).
[c3-25]J. L. Tedesco, B. L. VanMil, R. L. Myers-Ward, J. M. McCrate, S. A. Kitt, P. M. Campbell, G. G. Jernigan, J. C. Culbertson, J. C. R. Eddy and D. K. Gaskill, Appl. Phys. Lett. 95 (12), 122102-122103 (2009).
[c3-26]K. V. A. B. Emtsev, K. Horn, J. Jobst, Gary L. Kellogg, L. Ley, J. L. McChesney, T. Ohta, S. A. Reshanov, J. Röhrl, E. Rotenberg, A. K. Schmid, D. Waldmann, H. B. Weber & T. Seyller, Nat Mater **8** (3), 203-207 (2009).

CHAPTER 4

[c4-1]C. Berger, Z. Song, T. Li, X. Li, A. Y. Ogbazghi, R. Feng, Z. Dai, A. N. Marchenkov, E. H. Conrad, P. N. First and W. A. de Heer, The Journal of Physical Chemistry B 108 (52), 19912-19916 (2004).
[c4-2]A. K. Geim, Novoselov, K. S., Nat Mater 6 (3), 183-191 (2007).
[c4-3]K. V. A. B. Emtsev, K. Horn, J. Jobst, Gary L. Kellogg, L. Ley, J. L. McChesney, T. Ohta, S. A. Reshanov, J. Röhrl, E. Rotenberg, A. K. Schmid, D. Waldmann, H. B. Weber & T. Seyller, Nat Mater 8 (3), 203-207 (2009).
[c4-4]J. A. Robinson, M. Wetherington, J. L. Tedesco, P. M. Campbell, X. Weng, J. Stitt, M. A. Fanton, E. Frantz, D. Snyder, B. L. VanMil, G. G. Jernigan, R. L. Myers-Ward, C. R. Eddy and D. K. Gaskill, Nano Letters 9 (8), 2873-2876 (2009).
[c4-5]S. S. Shetu, S. U. Omar, K. M. Daniels, B. Daas, J. Andrews, S. Ma, T. S. Sudarshan and M. V. S. Chandrashekhar, Journal of Applied Physics 114 (16), - (2013).
[c4-6]B. K. Daas, S. U. Omar, S. Shetu, K. M. Daniels, S. Ma, T. S. Sudarshan and M. V. S. Chandrashekhar, Crystal Growth & Design 12 (7), 3379-3387 (2012).
[c4-7]C. Hallin, F. Owman, P. Mårtensson, A. Ellison, A. Konstantinov, O. Kordina and E. Janzén, Journal of Crystal Growth 181 (3), 241-253 (1997).
[c4-8]F. Owman, C. Hallin, P. Mårtensson and E. Janzén, Journal of Crystal Growth 167 (1–2), 391-395 (1996).
[c4-9]P. Waltereit, Brandt, O., Trampert, A., Grahn, H. T., Menniger, J., Ramsteiner, M., Reiche, M., Ploog, K. H., Nature 406 (6798), 865-868 (2000).
[c4-10]M. Ostler, I. Deretzis, S. Mammadov, F. Giannazzo, G. Nicotra, C. Spinella, T. Seyller and A. La Magna, Physical Review B 88 (8), 085408 (2013).
[c4-11]S. Kim, J. Ihm, H. J. Choi and Y.-W. Son, Physical Review Letters 100 (17), 176802 (2008).
[c4-12]F. Owman, C. Hallin, P. Mårtensson and E. Janzén, Journal of Crystal Growth 167 (1–2), 391-395 (1996).
[c4-13]U. Starke, physica status solidi (b) 246 (7), 1569-1579 (2009).
[c4-14]M. Kusunoki, T. Suzuki, T. Hirayama, N. Shibata and K. Kaneko, Applied Physics Letters 77 (4), 531-533 (2000).
[c4-15]M. Terrones, A. R. Botello-Méndez, J. Campos-Delgado, F. López-Urías, Y. I. Vega-Cantú, F. J. Rodríguez-Macías, A. L. Elías, E. Muñoz-Sandoval, A. G. Cano-Márquez, J.-C. Charlier and H. Terrones, Nano Today 5 (4), 351-372 (2010).
[c4-16]L. Bergman, D. Alexson, P. L. Murphy, R. J. Nemanich, M. Dutta, M. A. Stroscio, C. Balkas, H. Shin and R. F. Davis, Physical Review B 59 (20), 12977 (1999).

CHAPTER 5

[c5-1]A.K. Geim and K.S. Novoselov: Nat. Matter. 6 183 (2007)
[c5-2]Y.dan, Y. Lu, N.J. Kybert, Z. Luo and A.T.C. Johnson: Nano Lett. 9 1472 (2009)
[c5-3]Qazi et al., Express 3 075101 (2010)
[c5-4]Nomani et al., Sens. Actuators B 150, 301 (2010)

[c 5 - 5] R. Sharma, J. H. Baik, C. J. Perera, M. S. Strano., Nano Letters 10, 398-405
(2010)
[c5-6]Ferrari, A.C,et.al.;Phys. Rev. Lett. 7, 238 (2006)
[c5-7]P.J.Cumpson; Surf. Interface. Anal, 29, 403 (2000)
[c5-8]B.K Daas,K.M. Daniels, T.S.Sudarshan and MVS Chandrashekhar.; J. Appl. Phys. 110, 113114 (2011)
[c5-9]B. K. Daas, W. K. Nomani, K. M. Daniels, T. S. Sudarshan, G. Koley and MVS Chandrashekhar., Mater. Sci. Vol. 717-720 665-668 (2012).
[c5-10]O. Leenaerts, B. Partoens, and F.M. Peeters, Phys. Rev. B 77, 125416 (2008)
[c5-11]T.O. Wehling, K.S. Novoselov, S.V. Morozov, E.E. Vodvin, M.I. Katsnelson, A.K. Geim and A.I. Lichtenstein, Nano. Lett 8, 173 (2008)
[c5-12]Md. W.K. Nomani, R. Shishir, M. Qazi, D. Diwan, V.B. Shields, M.G. Spencer, G.S. Thompa, N.M. Sbrockey and G. Koley, Sens. Actuators B 150, 301 (2010)
[c5-13]T. Stauber, N.M.R Peres, A.K. Geim; Phy.Rev. B 78 085432 (2008)
[c5-14]Dmitriy Korobkin, Yaroslav Urzhumov, and Gennady Shvets**;** J. Opt. Soc. Am. B, 23,3,468 (2006)
[c5-15]V. P. Gusynin, S. G. Sharapov, and J. P. Carbotte; Phy. Rev. Lett. 96, 256802 (2006)
[c5-16]S.Y. Liu, X.L. Lei, Norman J.M. Horing: J. Appl. Phys. 104, 043705 (2008)
[c5-17]F. Schedin, A. K. Geim, S. V. Morozov, E. W. Hill, P. Blake, M. I. Katsnelson & K. S. Novoselov ,Nat. Mat. **6**, 652 - 655 (2007).
[c5-18]K. Persson, V. A. Sethuraman, L. J. Hardwick, Y. Hinuma, Y. S. Meng, A. van der Ven, V. Srinivasan, R. Kostecki, & G. Ceder, J. Phys. Chem. Lett. 2010 1 (8), 1176-1180
[c5-19]H. Du, J. Li, J. Zhang, G. Su, X. Li, & Y. Zhao, J. Phys. Chem. C 2011 115 (47), 23261-23266
[c5-20]S. P. Koenig,L. Wang,J. Pellegrino & J. S. Bunch, Nat nano 7, 728-732 (2012).

CHAPTER 6

[c6-1]M. S. Dresselhaus,G. Dresselhaus, *Adv. in Phys*., **1981**, 30,139.
[c6-2]F. Rodríguez-Reinoso, *Carbon*, **1998**,36,159.
[c6-3]P. R.Wentrcek, B. J. Wood, H. Wise, *J. Catalysis*, **1976**,43,363.
[c6-4]C. A. Bessel, K. Laubernds, N. M. Rodriguez, R.T. K. Baker,*J. Phys. Chem. B*, **2001**,105,1115.
[c6-5]T. Otowa, Y. Nojima,T. Miyazaki, *Carbon*,**1997**,35,1315.
[c6-6]M. D. Stoller, S. Park, Y. Zhu, J. An,R.S. Ruoff, *Nano Lett*., **2008**,8,3498.
[c6-7]S. Blankenburg, M. Bieri, R. Fasel, K. Müllen, C.A. Pignedoli, D. Passerone, *Small*, **2010**,6,2266.
[c6-8]F. Schedin, A. K. Geim, S. V. Morozov, E. W. Hill, P. Blake, M. I. Katsnelson, K. S. Novoselov, *Nat Mater*, **2007**, 6, 652.

[c6-9]G. M. Rutter, J. N. Crain, N. P. Guisinger, T. Li, P. N. First, J. A. Stroscio, *Science*, **2007**, 317, 219.
[c6-10]B. K. Daas, S. U. Omar, S. Shetu, K. M. Daniels, S. Ma, T. S. Sudarshan, M. V. S. Chandrashekhar, *Crys. Growth & Des*., **2012**, 12, 3379.
[c6-11]S. S. Shetu, S. U. Omar, K. M. Daniels, B. Daas, J. Andrews, S. Ma, T. S. Sudarshan, M. V. S. Chandrashekhar, *J. Appl. Phys*. , **2013**, 114, 16.
[c6-12]R Saito. 1998: World Scientific .
[c6-13]F. Banhart, J. Kotakoski, A. V. Krasheninnikov, *ACS Nano*, **2010**, 5, 26.
[c6-14]J. C. Meyer, C. Kisielowski, R. Erni, M. D. Rossell, M. F. Crommie, A. Zettl, *Nano Lett*., **2008**, 8, 3582.
[c6-15]A. K. Geim, K. S. Novoselov, *Nat Mater*, **2007**,6,183.
[c6-16]A. Reina, X. Jia, J. Ho, D. Nezich, H. Son, V. Bulovic, M. S. Dresselhaus, J. Kong, *Nano Lett.*, **2008**,9,30.
[c6-17]C. Virojanadara, M. Syväjarvi, R. Yakimova, L. I. Johansson, A. A. Zakharov,T. Balasubramanian, *Phys. Rev. B*, **2008**, 78, 245403.
[c6-18]P. W. Sutter, J.I. Flege, E. A. Sutter, *Nat Mater*, **2008**,7, 406.
[c6-19]W. A. De Heer, C. Berger, M. Ruan, M. Sprinkle, X. Li, Y. Hu, B. Zhang, J. Hankinson, E. Conrad, *Proceed. of the Nat. Acad. of Sci.*, **2011**, 108, 16900.
[c6-20]J. A. Robinson, M. Wetherington, J. L. Tedesco, P. M. Campbell, X. Weng, J. Stitt, M. A. Fanton, E. Frantz, D. Snyder, B. L. Vanmil, G. G. Jernigan, R. L. Myers-Ward, C. R. Eddy, D. K. Gaskill, *Nano Lett.*, **2009**, 9, 2873.
[c6-21]B. K. Daas, K. M. Daniels, T. S. Sudarshan, M. V. S. Chandrashekhar, *J. Appl. Phys.*, **2011**, 110, 11.
[c6-22]C. Berger, Z. Song, T. Li, X. Li, A.Y. Ogbazghi, R. Feng, Z. Dai, A. N. Marchenkov, E. H. Conrad, P.N. First, W.A. De Heer, *J.Phys. Chem. B*, **2004**, 108, 19912.
[c6-23]K.V. Emtsev, A. Bostwick, K. Horn, J. Jobst, G. L. Kellogg, L. Ley, J. L. Mcchesney, T. Ohta, S. A. Reshanov, J. Rohrl, E. Rotenberg, A. K. Schmid, D. Waldmann, H. B. Weber, T.Seyller, *Nat Mater*, **2009**, 8, 203.
[c6-24]J. Drowart, G. De Maria, M. G. Inghram, *J. Chem. Phys.*, **1958**, 29, 1015.
[c6-25]M. Hupalo, E. H. Conrad, M. C. Tringides, *Phys. Rev. B*, **2009**. 80, 041401.
[c6-26]K. M. Daniels, B. K. Daas, N. Srivastava, C. Williams, R. M. Feenstra, T. S. Sudarshan, M. V. S. Chandrashekhar, *J. Appl. Phys*.**, 2012**. 111,11.
[c6-27]D. Sun, C. Divin, C. Berger, W. A. De Heer, P. N. First, T. B. Norris, *Phys. Rev. Lett.*, **2010**, 104, 136802.
[c6-28]M. Kumagawa, H. Kuwabara, S. Yamada, *J. J. Appl. Phys*., **1969**, 8, 421.
[c6-29]T. Rana, M. V. S. Chandrashekhar, T. S. Sudarshan, *J. Cryst. Growth*, **2013**, 380, 61.
[c6-30]W. Collins, in *Kirk-Othmer Encyclopedia of Chemical Technology*, **2000**, John Wiley & Sons, Inc.
[c6-31]P. L. Timms, R. A. Kent, T. C. Ehlert, J. L. Margrave, *J. Amer. Chem. Soc.* , **1965**, 87, 2824.
[c6-32]S. Shivaraman, M. V. S. Chandrashekhar, J. J. Boeckl, M. G. Spencer, *J. Elec. Mater*., **2009**, 38, 725.
[c6-33]W. A. De Heer, C. Berger, X. Wu, P. N. First, E. H. Conrad, X. Li, T. Li, M. Sprinkle, J. Hass, M. L. Sadowski, M. Potemski, Gérard Martinez, *Sol. Stat. Comm.*, **2007**,143,92.
[c6-34]K. S. Novoselov, D. Jiang, F. Schedin, T. J. Booth, V. V. Khotkevich, S. V. Morozov, A. K. Geim, *Proceed. of the Nat. Acad. of Sci. of the USA*, **2005**, 102, 10451.

[c6-35]M. Terrones, A. R. Botello-Méndez, J. Campos-Delgado, F. López-Urías, Y. I. Vega-Cantú, F. J. Rodríguez-Macías, A. L. Elías, E. Muñoz-Sandoval, A. G. Cano-Márquez, J. Charlier, H. Terrones, *Nano Today*, **2010**, 5, 351.

[c6-36]J. Kedzierski, H. Pei-Lan, P. Healey, P. W. Wyatt, C. L. Keast, Mike Sprinkle, C. Berger,W. A. De Heer, *Elect. Dev., IEEE Transac. on*, **2008**, 55, 2078.

[c6-37]B. L. Vanmil, R. L. Myers-Ward, J. L. Tedesco, C. R. Eddy, G. G. Jernigan, J. C. Culbertson, P. M. Campbell, J. M. Mccrate, S.A. Kitt, D. K. Gaskill. in *Materials Science Forum*. **2009**. Trans Tech Publ.

[c6-38]L. G. Cancado, K. Takai, T. Enoki, M. Endo, Y. A. Kim, H. Mizusaki, A. Jorio, L. N. Coelho, R. Magalhaes-Paniago, M. A. Pimenta, *Appl. Phys. Lett*., **2006**,88, 163106.

[c6-39]G. Wagner, D. Schulz,D. Siche, Progress in *Cryst. Growth and Character. of Mater*., **2003**, 47, 139.

[c6-40]T. Rana, M. V. S. Chandrashekhar, T. S. Sudarshan, *phys. stat. solidi (a*), **2012**,209, 2455.

[c6-41]A. C. Ferrari, J. C. Meyer, V. Scardaci, C. Casiraghi, M. Lazzeri, F. Mauri, S. Piscanec, D. Jiang, K. S. Novoselov, S. Roth, A. K. Geim, *Phys. Rev. Lett*., **2006**,97,187401.